5-2015

The Experimental and Theoretical Study of Plasticity Improvement of Zr-Based Bulk Metallic Glasses

Xie Xie
University of Tennessee - Knoxville, xxie3@vols.utk.edu

To the Graduate Council:

I am submitting herewith a dissertation written by Xie Xie entitled "The Experimental and Theoretical Study of Plasticity Improvement of Zr-Based Bulk Metallic Glasses." I have examined the final electronic copy of this dissertation for form and content and recommend that it be accepted in partial fulfillment of the requirements for the degree of Doctor of Philosophy, with a major in Materials Science and Engineering.

Peter K. Liaw, Major Professor

We have read this dissertation and recommend its acceptance:

Yanfei Gao, Hairong Qi, Mariya Zhuravleva

Accepted for the Council:
Dixie L. Thompson

Vice Provost and Dean of the Graduate School

(Original signatures are on file with official student records.)

The Experimental and Theoretical Study of Plasticity Improvement of Zr-Based Bulk Metallic Glasses

A Dissertation Presented for the
Doctor of Philosophy
Degree
The University of Tennessee, Knoxville

XIE XIE

May 2015

ACKNOWLEDGEMENTS

First and foremost, I would like to thank my academic advisor, Prof. Peter K. Liaw, for his instructions on my graduate study and guidance on my professional career. I would also like to thank the committee members: Prof. Yanfei Gao, Prof. Hairong Qi, and Prof. Mariya Zhuravleva, for their kind agreement to be on my Doctoral Committee, and thought-provoking discussions and suggestions on my dissertation work. I want to pay my sincere gratitudes to all those who helped me complete the Ph.D. degree in Materials Science and Engineering.

My sincere thanks also go to Prof. Karin A. Dahmen, at the University of Illinois at Urbana–Champaign, for the insightful comments to my study on the intrinsic feature of serration behavior. I would like to than Mr. James Antonaglia and Mr. Abid Khan from University of Illinois at Urbana–Champaign for the cooperated work. I would like to thank Prof. Yung C. Shin and Dr. Yunfeng Cao, at Purdue University, for conducting the laser shock peening on the BMG samples and the collaboration. I am grateful to Prof. Philip J. Withers and Dr. Bartlomiej Winiarski from The University of Manchester, U.K., for their help in mapping the residual stress of the laser-peened sample, and constructive comments on our joint work. I would like to thank Prof. Fuqian Yang, Dr. Guangfeng Zhao, and Ms. Peizhen Li, from University of Kentucky, for their help in performing nanoindentation and the collaboration. I would like to thank Prof. Yoshihiko Yokoyama from Tohoku University, for providing high-quality BMG samples. I appreciate Prof. Junwei Qiao from Taiyuan University of Technology, China, and Prof. Yong Zhang from University of Science and Technology Beijing, China, for the informative discussions on

my study and collaboration. I am also grateful to Prof. Takeshi Egami and Dr. Wojciech Dmowski, for the instructive discussion about the synchrotron X-ray diffraction and pair distribution function analysis. I would like to thank Dr. Yang Ren at the Argonne National Laboratory. Without Dr. Ren's offer of the beamtime and help for the synchrotron x-ray experiments, I could not complete this work. I would like to thank Mr. Douglas E. Fielden, and his team, Mr. Larry D. Smith and Mr. Dan Hackworth, in the mechanical workshop at The University of Tennessee, for the enlightening talks and the great help in machining the test samples. The work included in this thesis would not be possible without their support.

I am also indebted to Mr. Gregory Jones and Mr. John Budai for helping me on the operation of the scanning electron microscope, focused ion beam, and transmission electron microscopy. My thanks should go to Ms. Carla Lewrence, Ms. Martha Gale, Ms. Tonya Brewer, Ms. Tracy Lee, Mr. Frank Holiway, Mr. Randy Stooksbury, Mr. Stephen Stiner, and Ms. Carol Winn in our department for their great help.

I would like to thank all of my fellow doctoral students for their help and friendship. I am especially grateful to Dr. Gongyao Wang, Dr. Zhengke Teng, Dr. Liang Wu, Dr. E-wen Huang, Dr. Sooyeol Lee, Dr. Feng Jiang, Dr. Li Li, Dr. Shenyan Huang, Dr. Andrew Chuang, Dr. Wei Wu, Dr. Lu Huang, Mr. Zhinan An, Mr. Wei Guo, Mr. Qingming Feng, Mr. Zhiqian Sun, Mr. Bilin Chen, Dr. Zhi Tang, Mr. Tong Yang, Mr. Louis J. Santodonato, Mr. Gian Song, Ms. Haoyan Diao, Mr. Yuting Li, Ms. Shuying Chen, Mr. Haifei Li, Ms. Xue Bai, Mr. Rui Feng, and new group members, at The University of Tennessee. I also would

like thank the visiting professors, Prof. Gong Li, Prof. Qing Wang, Prof. Yan Wang, Prof. Weili Ren, and Prof. Jieshan Hou, for their help and inspiring discussions. I would like specially thank Mr. James Brechtl for the interesting discussion about the fractal study on BMGs.

This research is mainly supported by the U.S. National Science Foundation (NSF), under Grant No. CMMI-0900271, with Dr. C. V. Cooper as the program manager, and the U.S. Department of Energy (DOE), Office of Fossil Energy (DE-FE-0011194) with S. Markovich as contract monitor. This research used resources of the Advanced Photon Source, a U.S. Department of Energy (DOE) Office of Science User Facility operated for the DOE Office of Science by Argonne National Laboratory under Contract No. DE-AC02-06CH11357.

Last but not least, I would like to dedicate my thesis to my wife, Yi Zhao, my little angel, Iris Z. Xie, my parents, Fugong Xie and Jinrong Zhu, my farther- and mother-in-law, Xide Zhao and Wenfeng Sang, for their love, encouragement, and support in all my pursuits.

ABSTRACT

Bulk metallic glasses (BMGs) attract more and more attention for their great mechanical properties, such as high strength, good corrosion resistance, etc. However, even though extensive studies have been made, their deformation mechanisms are still not well understood. Their limited plasticity and catastrophic failure after yielding severely prevent their broad applications in industry and daily life. To improve their plasticity, some work has been done through miscellaneous processing methods, e.g., thin-film coating, surface treatment, and ion irradiation. The present work also focuses on the plastic deformation of BMGs, and is expected to deepen the fundamental understanding of the deformation mechanisms through the study of several methods, which could improve their plasticity, namely, geometrical constraint, pre-fatigue, and laser-induced constraint. To characterize the improvement, compression, four-point bending fatigue, and nanoindentation experiments were conducted. Moreover, recent work suggests that BMGs also show serrated flows in certain regimes of temperatures and strain rates, which is similar to the Portevin–Le Chatelier effect (PLC) in traditional alloys. Thus, the serrated flow can be used as a probe for studying the deformation process. Through the investigations of serration behavior, it's expected that the details of deformation dynamics can be extracted. The thermograph study and synchrotron X-ray diffraction were also utilized to investigate the shear-band dynamics and structural changes. Serration characteristics were analyzed statistically and a slip avalanche model was successfully applied on BMGs.

TABLE OF CONTENTS

LIST OF TABLES

LIST OF FIGURES

CHAPTER I INTRODUCTION

1.1 Background

Bulk metallic glasses (BMGs) possess many unique properties [1-3], such as high fracture strength [4, 5], high fracture toughness [6], excellent magnetic properties [7, 8], good fatigue resistance [9-13], and high corrosion resistance [14-17]. However, their applications as potential engineering and structural materials [18] are limited, because their deformation mechanisms, often resulting in poor ductility, are not well understood. The reason lies in the difficulties associated with defining their amorphous structures.

BMGs are fabricated by rapid cooling to freeze the "random position" of atoms in a liquid phase, which requires extremely fast cooling rates. Unlike the lattice structures in crystalline materials, there are free volumes (voids) left in these bulk specimens after solidification. More specifically, the free volumes promote the formation of weak spots or shear transformation zones (STZs) in BMGs [19-21]. Generally, the volume fraction of weak spots is regarded as 1%, such as in the free-volume theory [22]. If this is true, they will not contribute too much to the mechanical behavior of BMGs. Recent studies, however, revealed that the fraction of weak spots could be as large as 25% through the synchrotron diffraction study [20]. Therefore, these weak spots should be taken into account, and a comprehensive theory to interpret the deformation mechanism of BMGs is needed.

1.2 Objective and Motivation

The goal of this study is to understand the plastic deformation of BMGs under different loading conditions through the experimental study, statistical analysis, and

theoretical modeling. Investigating the universal behavior of BMGs during plastic deformation in combination with the microscopy, diffraction, and modeling techniques will provide an innovative and transformative approach to (1) quantify the shear-band dynamics and (2) detail the fundamental deformation mechanism of BMGs.

At room temperature, the plastic deformation is closely related to serration behavior in the stress-strain curve or load-displacement curve. The serration behavior of BMGs results from a complicated process involving heterogeneous deformation and microstructural evolution, which is not yet well understood. Based on our understanding and studies for BMGs [23-28], a hypothesis is proposed that the statistical characteristics (e.g., the magnitudes of stress drops) in the serrations of BMGs follow a tuned critical scaling behavior, for instance, the strain rate could act as the tuning parameters. If this hypothesis is confirmed, the seemingly stochastic serration behavior could be described using a universal model, regardless of the BMG composition.

More specifically, first, serration behavior will be studied under different conditions, including constrained and unconstrained environments, fatigue effects, laser-treatment effects, and different loading rates. The mean-filed theory (MFT) based models, which are developed for crystalline materials, will be adapted to describe the serration behavior in BMGs. After verifying models with experimental results, the accuracy of the models will be refined, and can then be used to predict the serration characteristics of BMGs. Thus, the present research will allow the investigation of the intrinsic mechanisms of plastic deformation of BMGs.

The proposed work will potentially transform the popular understanding of materials deformation behavior and present a novel perspective to probe the universal

serration characteristics in a wide range of advanced materials, including BMGs, high-entropy alloys (HEAs), and nanocrystalline and granular materials.

1.3 Framework

To study the serration behavior, a high-resolution data-acquisition rate (e.g., 100 Hz) is essential to ensure that every serration detail is captured successfully. Otherwise, the analyses and modeling results may not capture the whole information, possibly leading to incomplete or even fallacious conclusions. However, most published work did not focus on the serration investigation and use a relatively low-resolution data-acquisition rate, such as 3 or 10 Hz. Thus, systematically compression experiments should be performed in order to provide the detailed serration data to be gathered at a high-resolution data-acquisition rate of 100 Hz for the development and refinement of our slip-avalanche theory and models.

The present study mainly focuses on the following eight aspects about the experiments and modeling of plastic deformation, i.e., (1) constrained and unconstrained conditions, (2) fatigue effects on plastic behavior, (3) laser-treatment induced effects on plasticity, (4) characterization of shear-band and fracture morphologies, (5) synchrotron diffraction on laser-treated samples, (6) thermograph studies of shear-band evolution, and (7) development of theoretical models and analysis of serration behavior and modification of current models for plastic deformation.

1.4 Intellectual Merit and Broader Impacts

1.4.1 Intellectual merit

In this project, we will develop a new approach combining materials science, mechanical engineering, and statistics. The experiments and models will quantify the serration behavior of slowly deformed BMGs under different conditions, e.g., geometrical constraint effects, fatigue-strain effects, and laser-induced constraint effects. The experiments will characterize the morphologies and structures of the BMGs using SEM, thermograph, and synchrotron diffraction. To describe the serration statistics, we will apply a MFT model to BMGs. The study is expected to reveal the underlying mechanisms of plastic deformation in BMGs through the comparison of model parameters, interpretations, and predictions with experiments on serration statistics and morphology characterization during slow deformation of BMGs.

1.4.2 Broader impacts

The current research is expected to contribute to the fundamental understanding of BMGs. The experimental and theoretical results will be disseminated through articles in scientific journals and conference talks. Public lectures for middle- and high-school students, teachers, and the general public will be offered. Appropriate aspects of the research results will be incorporated into the graduate and undergraduate course materials in the University of Tennessee to introduce students to modern interdisciplinary materials research. Revealing the deformation mechanisms of BMGs will significantly promote the industrial, commercial, and engineering applications of these materials as substitutes for

traditional alloys. All the results will be presented in relevant symposia at domestic and international conferences, such as the Minerals, Metals, and Materials (TMS), Materials Science & Technology (MS&T), and Materials Research Society (MRS) meetings.

CHAPTER II LITERATURE REVIEW

2.1 Serrated Behavior for Crystalline Materials and BMGs

Under compression or tension, at certain regime of temperatures and slow strain rates, crystalline materials, including nanocrystals and high entropy alloys (HEAs), exhibit serrated-flow or stick-slip or jagging behavior in their stress-strain curves. Since serration occurs after yielding point, it provides a way to understand the mechanism for plastic deformation of materials. Over the past several decades, extensive researches have been conducted to investigate, characterize, quantify, and model this phenomenon [29-52]. Generally speaking, this trend means that under slowly increasing shear force, the material responds in a jerky way with sudden stress drops, indicating sudden slips occurring in the material, which is related to the collective motion of dislocations, or deformation twining, or boundary movement, such as in the Portevin-LeChatellier (PLC) effect, or dynamic strain aging [53-57].

For traditional alloys, serration behavior, also known as the PLC effect, can be observed in certain temperature regimes at a specific strain rate. For instance, a serrated flow appears at 423 - 523 K for a Mg-Gd-Zn alloy [58], 473 - 923 K for Hastelloy X (a Ni-based superalloy) [59], 523 - 1,023 K for alloy 625 (a Ni-based superalloy) [60], below 373 K for an Al alloy [61], and 573 - 873 K for an austenitic stainless steel [62]. Interestingly, beginning from the lower temperature for each alloy, as shown above, serrations seem to be amplified as temperature increases, but disappears beyond higher temperature [58-62].

Recent study [63] found the temperature dependence of the deformation properties of HEAs under slow shear, which may include dislocation motion and

deformation twinning. The results show a smaller slip size at a higher temperature for the investigated HEAs. One possible reason, for the cases of MoNbTaW and $Al_5Cr_{12}Fe_{35}Mn_{28}Ni_{20}$ HEAs, could be that a higher temperature increases the mobility of diffusing solute atoms and also the thermal vibration energy of pinning solute atoms. Since HEAs are regarded as solid solutions, each constituent element can be a solute atom. During deformation, the solute atoms will move toward dislocations because of the stress field around dislocations. Thus, an atmosphere formed by these solute atoms can "drag" and pin the dislocations, similar to the Cottrell atmosphere [64]. When the external load keep on increasing, eventually the dislocation can escape the solute atmosphere and move until being caught by the next atmosphere. This process corresponds to one serration event (stress rise and sudden drop) in the stress-strain curve with the PLC effect [53, 54, 57]. However, although the speed of solute atoms increases at higher temperature, the thermal vibration amplitude of atoms increases too. This means that the pinning effect of solutes around dislocations becomes smaller because solute atoms tend to shake away from their low energy sites for pinning. As a result, the slip size will be decreased. Another reason, for the case of $Al_{0.5}CoCrCuFeNi$ HEA in the present study, is related to twinning, since higher temperatures make it more difficult for deformation twins to be induced. This trend is very probably the case in the cryogenic temperature range where twinning occurs during deformation. Increasing the temperature will induce lesser twinning and, thus, a smaller slip size. Other possible reasons may also exist, like phase-transformation-induced changes in the deformation mechanism. This study gives a glimpse of the usefulness of studying the serration statistics to understand the deformation mechanics of new materials. To further test the theory, experimental

studies of the slip statistics for a broader range of temperatures should be performed, and the characterization of microstructures during and after deformation, e.g., using transmission electron microscopy (TEM) to investigate the dislocation and nanotwining [65], is essential to corroborate with our analysis results.

2.2 Miscellaneous Effects on the Plastic Deformation of BMGs

Previous work has reported that miscellaneous effects on the plastic deformation of BMGs, such as the strain-rate, sample-size, and temperature effects. Shear-band operation, i.e., initiation, propagation, and arrest, may be changed dramatically under different loading conditions.

2.2.1 Compressive performance at different strain rates

Similar to the effect on dislocation motion in crystalline materials, strain rate plays an important role in the deformation process of BMGs. In general, deformation behavior in BMGs can be divided into three modes, namely elastic, homogeneous (high temperatures and low strain rates), and inhomogeneous modes (low temperatures and high strain rates), which is first proposed in a form of a deformation map by Spaepen [22]. The deformation map was later reconstructed by several authors to incorporate more BMG compositions [66, 67]. According to this map, several studies have been conducted, concerning the strain-rate effect on BMGs [68-72], but with a focus on the relationship between the fracture morphology and strain rate. However, the deformation mechanisms are still not well understood and require further investigation.

Figure 1 shows an example for the study of strain-rate effects. Different strain rates lead to distinct serration patterns [24]. Interestingly, the magnitude of serration increases as strain rate decreases. Specifically, at a high strain rate of 10^{-2}/s in Figure 1(d), the flow curve becomes smoother, and it is hard to distinguish one serration from another. It is quite noticeable that the deformation mechanism inside the BMGs has changed with strain rate during the dynamic process. Nevertheless, the fracture morphology cannot capture the whole picture.

2.2.2 Sample-size effects

Besides strain-rate effect, sample size can also influence the serration behavior of BMGs. As introduced in Sect. 1.1, the anelastic sites will sufficiently affect the mechanical behavior of BMGs, and the sample size is closely related to the quantity of anelastic sites. Similar to the case in strain-rate effects, the size-dependent mechanical behavior has been studied during recent years [73-82], and the fracture morphology is related to the ductility of BMG samples.

Figure 3 depicts the compressive stress-strain curves of different sample sizes for the $Ti_{40}Zr_{25}Cu_{12}Ni_3Be_{20}$ and $Zr_{64.13}Cu_{15.75}Ni_{10.12}Al_{10}$ (at.%) BMGs, respectively [83, 84]. Regardless of the composition, a conclusion of "smaller is softer" for BMGs could be reached [85]. Furthermore, the serration styles are different for each size, in terms of the quantity of serration events, the amplitudes of serrations, and the trend of serrations (e.g., the magnitude becomes larger towards the failure direction).

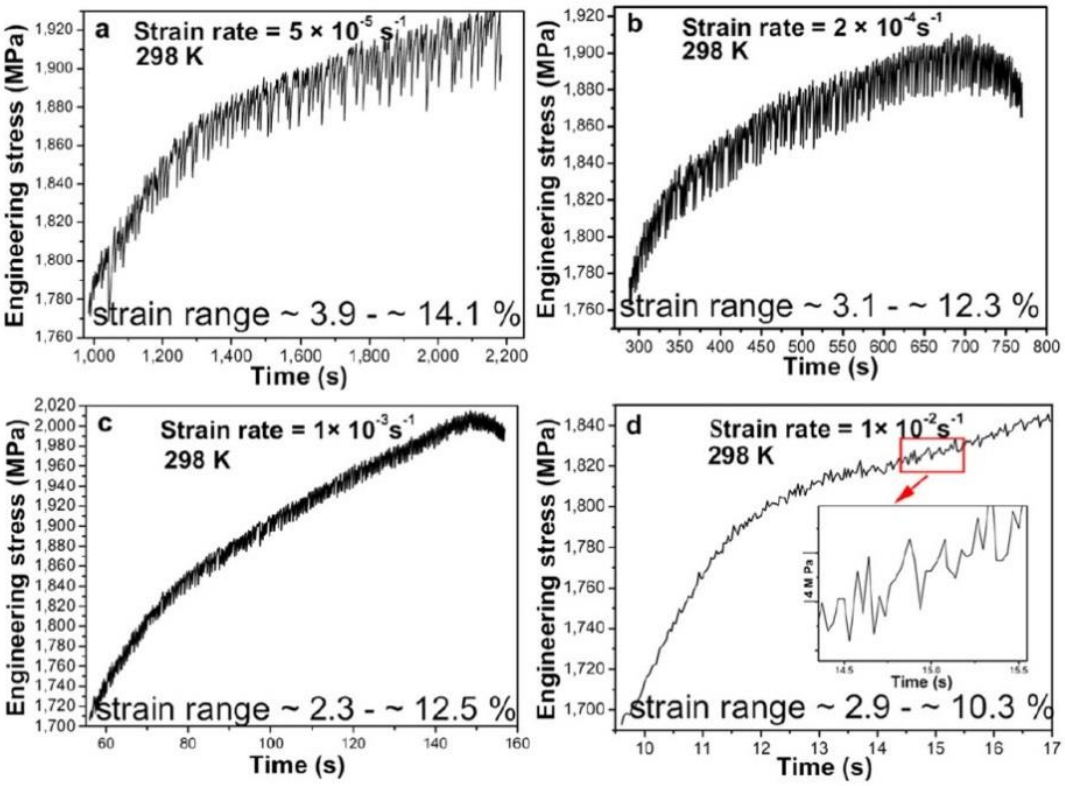

Figure 1. Serrated flow stresses in compression tests for the $Zr_{64.13}Cu_{15.75}Ni_{10.12}Al_{10}$ BMG at different strain rates of (a) 5×10^{-5}/s, (b) 2×10^{-4}/s, (c) 1×10^{-3}/s, and (d) 1×10^{-2}/s [24]

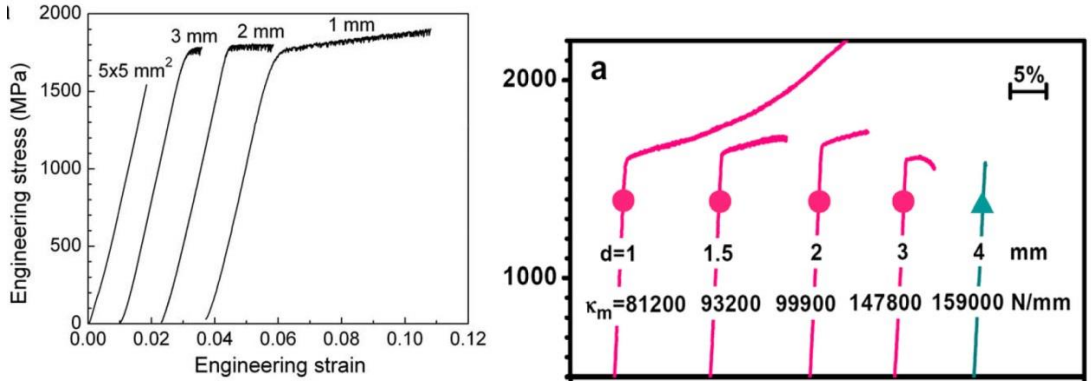

Figure 2. Sample-size effects on (a) $Ti_{40}Zr_{25}Cu_{12}Ni_3Be_{20}$ [83] and (b) $Zr_{64.13}Cu_{15.75}Ni_{10.12}Al_{10}$ BMGs [84]

2.2.3 Temperature effects

Temperature can affect the mechanical behavior of BMGs dramatically, including the yield strength, failure strength, brittle-to-ductile transition, and shear-band patterns, as reported in the previous work [86-92], At cryogenic and elevated temperatures, the shear plasticity in the compression experiment increases largely, and more plastic strains will be obtained than the case in room temperature [89, 92]. However, serrations in the flow curves disappear at temperatures well below or above room temperature [90, 91]. This trend implies that the deformation mechanism may change under different temperature regions.

Figure 3 shows the stress-strain curves of the $Au_{65}Cu_{10.5}Si_{17}Ag_{7.5}$ and $Ni_{60}Pd_{20}P_{17}B_3$ (at.%) BMGs [87, 88], respectively, and stress-time curves of the $Zr_{52.5}Cu_{17.9}Ni_{14.6}Al_{10.0}Ti_{5.0}$ (at.%) BMG [86] at low temperatures. From Figure 3(a) and (b), it's evident that the shear plasticity is increased, as temperature decreases, together with a decrease for the amplitude of serrations. Specifically, at 77 K, serrations become indiscernible or even disappear. With a close look at the serration part, Figure 3(c) clearly indicates that both temperature and strain rate have great impacts on the magnitudes and patterns of serrations. Some work attributes these differences to the temperature-induced changes in the shear-band operation, shear-transformation-zone (STZ) volume, or viscosity [86-88, 92], but the internal deformation mechanism is still unknown.

Figure 7 exhibits the different shear-band patterns of the $Ni_{60}Pd_{20}P_{17}B_3$ (at.%) BMG after compression at cryogenic temperatures [88]. At room temperature, a single shear band dominates the deformation process. As the temperature decreases, multiple

shear bands appear, and the interactions of shear bands intensify. Upon close examination, secondary shear bands intersect with primary shear bands at 77 K in Figure 4d. It is reasonable to relate the ductile behavior at 77 K with the extensive shear-band distribution here [88]. In present study, it's expected to relate the features of shear band distribution with serrated flow behavior druring deformation.

2.3 Slip-avalanche Model

Power-law behavior, or scaling characteristics, has been found in a wide range of systems in nature and man-made phenomena, such as earthquake size [93], large-scale network [94], economic index [95], allometric scaling relations in biology [96], metabolic networks [97], and neuronal avalanche [98]. Extensive efforts have been devoted to studying and characterizing the critical feature (e.g., the particular scaling exponent) of the power-law behavior. Particularly, for the investigation of mechanical behavior of materials, several analytical models have been developed to describe and predict the scaling characteristics, for instance, discrete dislocation-dynamics models [99-106], continuum models [100], phase-field models [107], and phase-field-crystal models [108]. Most of them are originally proposed for crystalline or polycrystalline materials, and focus on dislocation behavior. In contrast, very limited work has been done for BMGs, since the deformation mechanism of BMGs is still under investigation. Generally, BMGs deform via shear-band initiation and propagation behavior [22, 109], which is fundamentally different from the deformation mechanism of crystalline materials, such as the movement of dislocations and grain boundaries. Despite the distinct deformation

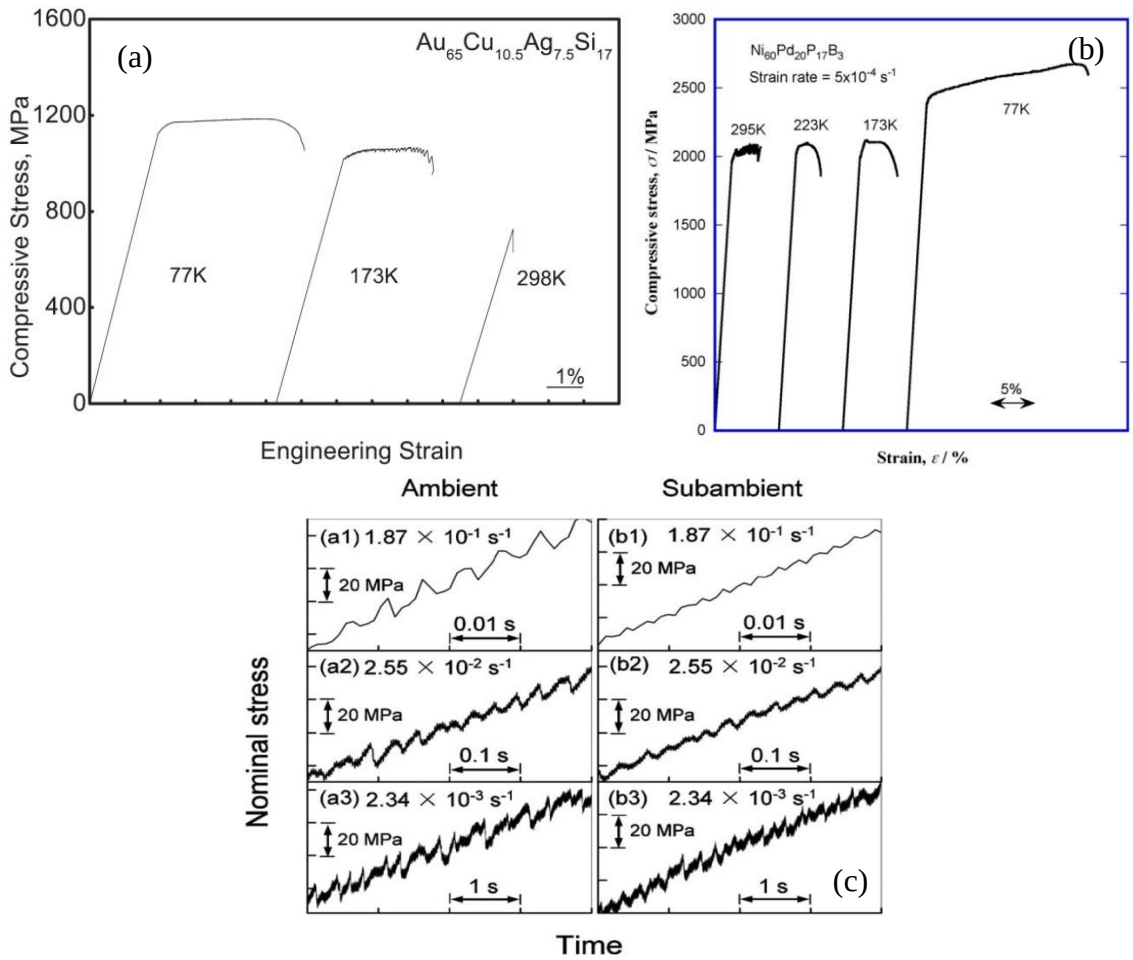

Figure 3. Compressive stress-strain (or stress-time) curves at different temperatures for the (a) $Au_{65}Cu_{10.5}Si_{17}Ag_{7.5}$ [87], (b) $Ni_{60}Pd_{20}P_{17}B_3$ [88], (c) $Zr_{52.5}Cu_{17.9}Ni_{14.6}Al_{10.0}Ti_{5.0}$ BMGs (Ambient: 298 K, Subambient: 194.5 K) [86]

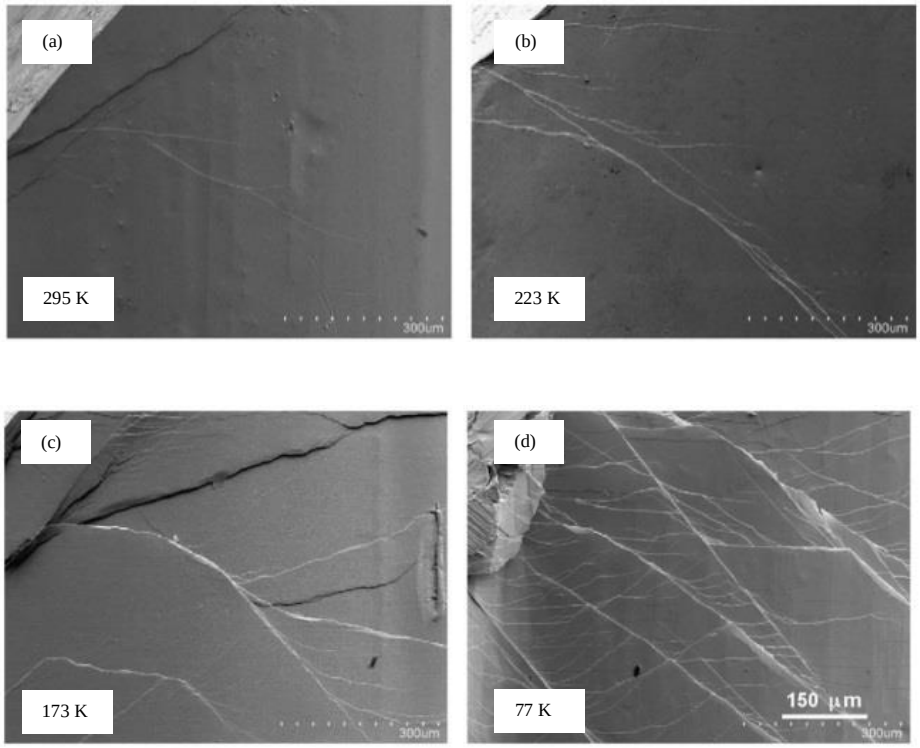

Figure 4. SEM images of a lateral surface of a fractured $Ni_{60}Pd_{20}P_{17}B_3$ BMG showing the shear-band patterns at (a) room temperature (295 K), (b) 223 K, (c) 173 K, and (d) 77 K [88]

mechanism, interestingly, scaling behavior has also been found in BMGs in our preliminary study. Therefore, an analytical model, specifically designed from the theory for BMGs, is essentially needed to uncover the hidden law, which governs deformation characteristics, and to stimulate more in-depth investigations of deformation mechanisms, based on quantitative models and analyses.

In recent years, an MFT model has been developed and applied on the studies of nanocrystals and microcrystals by Dahmen, et al. [25, 26, 110]. The analytical model predicts the serration statistics for the slowly increasing stress-boundary condition or for the small imposed strain-rate boundary condition. With N lattice points, the local stress, τ_l, at a lattice point, l, under the condition of a slowly increasing applied shear stress (F), is given by [25, 26]:

$$\tau_l = (J / N)\, \Sigma_m \left(u_m - u_l\right) + F \tag{1}$$

where J/N is the elastic coupling between sites in the mean-field approximation, u_l is the total fault offset (or cumulative slip) of a lattice point, l, in the shear direction. Under the slow strain-rate loading conditions, the applied stress, F, is replaced by the stress exerted through a slowly-moving sample surface. Thus, the resulting applied stress at a site, l, is given by

$$F = K_L \left(vt - u_l\right) \tag{2}$$

where t is time, K_L is a weak spring constant, modeling the coupling of the site, l, to the sample surface, and v is the speed at which the surface moves in the shear direction. Each point fails when the local stress, τ_l, is larger than the local static failure threshold stress, $\tau_{f,l} = \tau_{s,l}$, or a local dynamical failure threshold stress, $\tau_{f,l} = \tau_{d,l}$ [25, 26]. The random local failure threshold stresses, $\tau_{f,l}$, are taken from a narrow probability distribution. When the

site, l, fails, it slips by a certain amount, Δu_l, resulting in a stress reduction, $\tau_{f,l} - \tau_{a,l} \sim 2G\ \Delta u_l$, where $G \sim J$ is the elastic shear modulus, and $\tau_{a,l}$ is a random local arrest stress, also taken from a narrow probability distribution. The released stress is equally redistributed to the other points in the system, possibly triggering other points to slip, and thus leading to a slip avalanche, which is measurable as a serration in the stress-strain curve or as acoustic emission. Through analyses on the slip avalanche using serration statistics, the model could be employed to explore the distribution of slip sizes, and provide the useful information of the dynamic-deformation process, such as the evolution of defects.

For small imposed-stresses, F, at the lowest temperatures, the MFT model predicts that *in the steady state*, the probability density function (pdf) of the magnitudes, S, of the stress-drop avalanches scales as [25, 110]

$$D(S,F) \sim S^{-\kappa} D'[S(F-F_c)^{1/\sigma}] \tag{3}$$

where $\kappa = 1.5$ and $1/\sigma = 2$ in MFT, are exponents to be determined from experiments, and $D'(x)$ is an exponentially-decaying universal scaling function. If the stress-strain curves have a curvature and flatten out near failure, then F_c is the critical stress at or near which the material breaks. If the stress-strain curves have a large linear region without a significant curvature, as is the case in many hardening crystals, then F_c can be taken to increase with stress or strain such that $(F\text{-}F_c)^{1/\sigma}$ in Eq. (3) is replaced by a constant that is proportional to the hardening coefficient, θ, as derived in Ref. [111]. Given the pdf, D(S,F), the complementary cumulative distribution function (CCDF), C(S,F), can be derived as [25, 110]

$$C(S,F) \sim (F-F_c)^{(\kappa-1)/\sigma} C'[S(F-F_c)^{1/\sigma}] \tag{4}$$

where C'(S,F) is another universal scaling function that can be derived from Eq. (3). The exponents, κ and $1/\sigma$, and the predicted scaling function, C'(x), can be determined for the experimental data by a fine-tuning method (called the Widom scaling collapse), as introduced in detail in [110]. The results are to be compared to the model predictions.

Some issues should be noted and carefully treated. The model predictions from Eqs. (3) and (4) apply to the so called "adiabatic" limit, which is the slow-driving limit where the individual avalanches are well separated in time. Therefore, the experimental tests will be repeated at the slowest possible loading rates to approach the theoretical limit as closely as possible. At the same time, the effects of finite-driving rates on the model predictions will be computed theoretically and compared to experiments.

Based on this model, reasonable agreement has been found between the experimental results and MFT-predicted values for nanocrystals and microcrystals [25, 26, 110]. The model can successfully predict the scaling behavior of slip statistics, and the particular exponent of the power-law distribution for nanocrystals and microcrystals was obtained.

In this work, the model will be applied to BMGs. The prediction of the model will be compared to experimental results, and if needed, refinement of the model will be applied. The present study will focus on different loading/pre-treatment conditions, combined with the theoretical analysis and modeling.

CHAPTER III EFFECTS OF GEOMETRICAL CONSTRAINT IN THE COMPRESSION STUDY

3.1 Introduction

To investigate the plastic behavior of BMGs, it's essential to distinguish that the plastic deformation in the experimental results is indeed the intrinsic feature of specimen, i.e., to separate it from the factors of testing machines. In this study, two important concepts in the analysis of plastic deformation will be clarified: (i) the serration behavior of BMG or machine noises, and (ii) intrinsic behavior of BMG or support from machine? To answer the first question, the compliance of machine needs to be considered. The noises can be detected and quantified through fitting in the elastic region of the stress-strain curve, which should be linear. Any serration with magnitudes smaller than the level of noise would be discarded. For the second question, the constrained and unconstrained tests are designed using the ratio of length to diameter (aspect ratio). With an aspect ratio of 2:1, which is the standard for universal compression tests, the BMG sample will fracture through primary shear bands, as shown in

Figure 5. However, when the aspect ratio is reduced to 1:1, primary shear band is impeded by the platen of machine, resulting in a compressed disk instead of fracture for the sample [81]. Through the analysis of the serration behavior, characteristics of deformation could be extracted and compared between above two conditions.

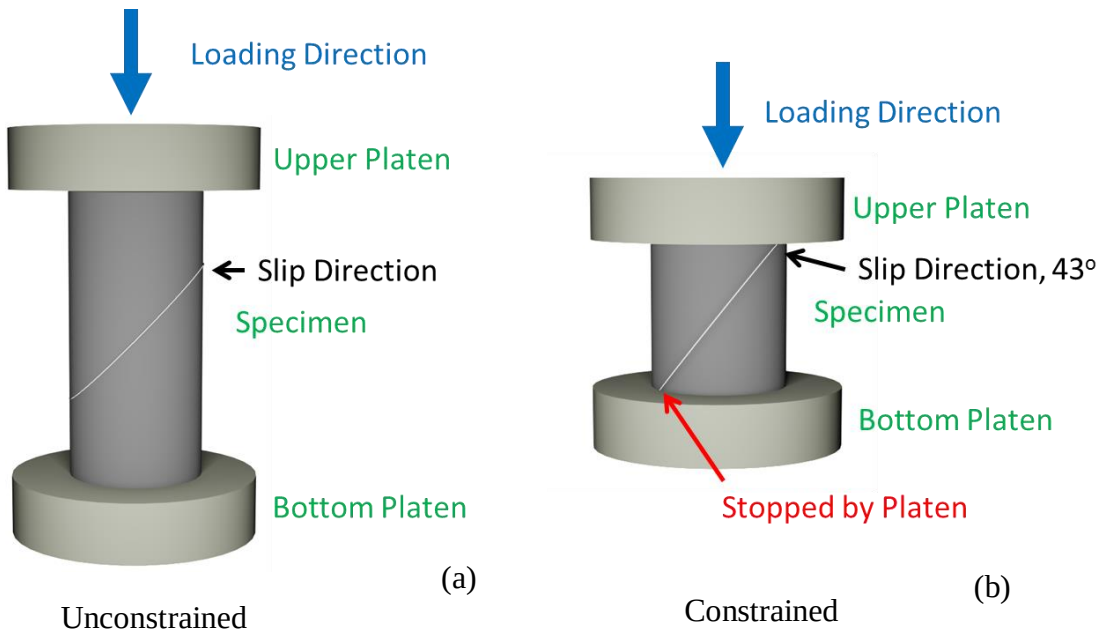

Figure 5. Schematic of (a) unconstrained and (b) constrained conditions in uniaxial compression tests

3.2 Experimental Methods

3.2.1 Sample preparation

Ingots of amorphous $Zr_{55}Cu_{30}Ni_5Al_{10}$ and $Zr_{64.13}Cu_{15.75}Ni_{10.12}Al_{10}$ (nominal atomic percents) BMGs were prepared by arc-melting the alloy mixture of Zr, Cu, Ni, and Al with purity higher than 99.9 weight percent in a Ti-gettered high-purity argon atmosphere. The melting and solicitation processes are repeated at least five times to achieve chemical homogeneity. For $Zr_{64.13}Cu_{15.75}Ni_{10.12}Al_{10}$, the melted mixture is suction cast into a water-cooled copper mold to form a cylindrical cast rod, 60 mm in length and 2 mm in diameter, while rectangular bars were cast for $Zr_{55}Cu_{30}Ni_5Al_{10}$ with a cross section of 3×3 mm. The cast rods were then cut into cylindrical bars with 4 mm in length and rectangular bars with 6 mm in length, respectively. The two compression faces of each bar were then carefully polished to be parallel to each other.

3.2.2 Compression experiments

The $Zr_{64.13}Cu_{15.75}Ni_{10.12}Al_{10}$ sample was uniaxially compressed at 298 K (room temperature) using a computer-controlled MTS 809 materials testing machine at a constant strain rate. Three strain rates, 5×10^{-5} s^{-1}, 2×10^{-4} s^{-1}, and 1×10^{-3} s^{-1} were employed in the compression experiments, with a data-acquisition rate of 33 Hz. Figure 11 shows images taken by scanning electron microscopy of the lateral surfaces of one of the compressively-fractured samples at a strain rate of 5×10^{-5} s^{-1}. The fractograph clearly indicates the multiple shear bands along which the sample deformed.

Figure 6 shows the schematic of a compression test on a BMG sample at a strain rate of 2×10^{-4} s^{-1}. The compression experiment was conducted by a computer-controlled Material Test System (MTS) servohydraulic testing machine, as indicated in Figure 6. An extensometer was utilized to record the strain changes [the inset in Figure 6]. A displacement-control mode is used, and a compression experiment is performed at a constant strain rate during one single test. The specimens were compressed to failure, and three variables, load, displacement, and strain, were recorded at an acquisition rate of 100 Hz.

3.2.3 Nanoindentation

Nanoindentation on the laser-treated samples is performed with a Micro Materials NanoTest using a Berkovich-type three-sided pyramidal diamond indenter. This system is a pendulum-based depth-sensing system, with the sample mounted vertically and the load applied electromagnetically (Figure 7). The test probe displacement is measured with a parallel plate capacitor achieving the subnanometer resolution (details in [112, 113]).

The samples were carefully grinded and polished to achieve a mirror finish using gridding papers of 400P, 600P, 800P, 1200P, and 2400P. The tests are repeated five times using a load control at room temperature. The maximum load is 100 mN, and the loading rate is set to 10 mN/s.

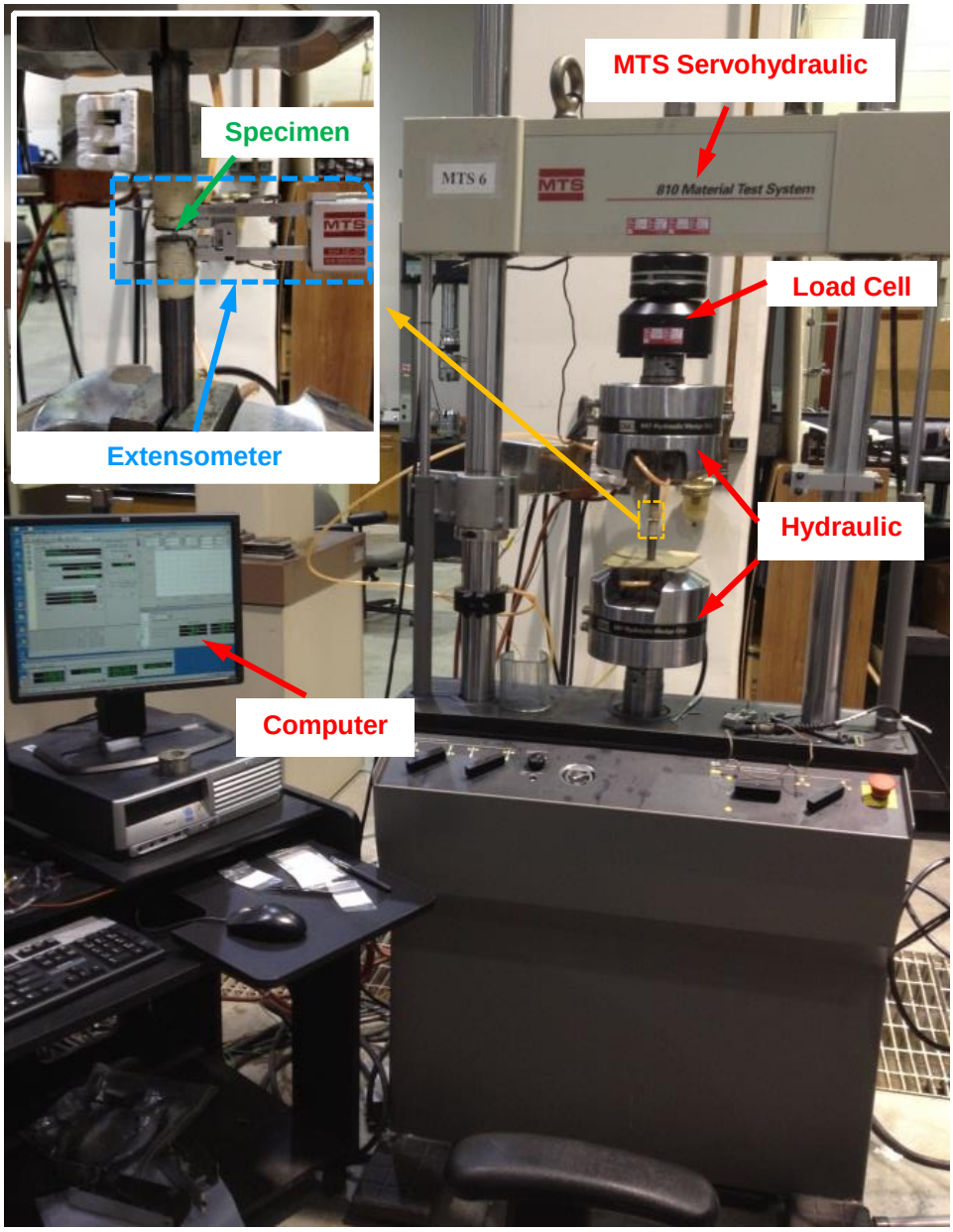

Figure 6. Schematic of a compression experiment for BMGs and the setup of a computer-controlled MTS machine

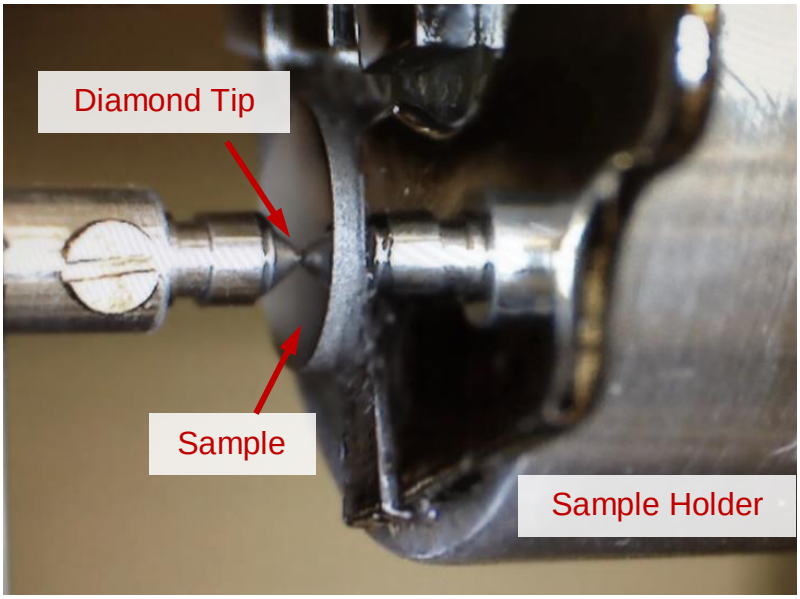

Figure 7. The setup of Micro Materials NanoTest for nanoindentation experiment

3.3 Results

3.3.1 Compressive stress-strain curves

Figure 8 show obvious difference in the stress-strain curves. Under unconstrained condition, only limited ductility can be achieved. In contrast, huge "plasticity" (quote here to indicate that this may not be the intrinsic feature of the sample) was obtained as well as work hardening behavior. Since under constrained condition, the sample is compressed into a disk instead of fracture, we used a cut-level of 3,000 MPa in the following statistical analysis. With careful inspection, the magnitudes and shapes of the serrated flow at different strain rates in Figure 8 are not identical. Figure 8a shows that the magnitude of stress drop is increasing as strain rate increase, but from Figure 8b, we could find that the stress drop with largest magnitude is located after yielding point, and keeps decreasing as external load increases. More detailed analysis will be described at Section 3.4.1. In addition, for unconstrained condition, the plastic strains are 0.17%, 0.38%, and 0.92% for 2×10^{-3} s^{-1}, 2×10^{-4} s^{-1}, and 1×10^{-4} s^{-1}, respectively. Work hardening behavior was not obvious. However, since the sample is continuously compressed, strong work hardening can be observed, possibly due to the support from the machine platens, and constrained the movement or propagation of shear bands, which actually reduce s the freedom of the dynamic system.

3.3.2 Surface morphology investigated by SEM

Scanning electron microscopy (SEM) was performed to investigate the surface morphology on the fractured samples and compressed plate. Under unconstrained condition, the BMG specimen fractured along the primary shear band, indicated as red

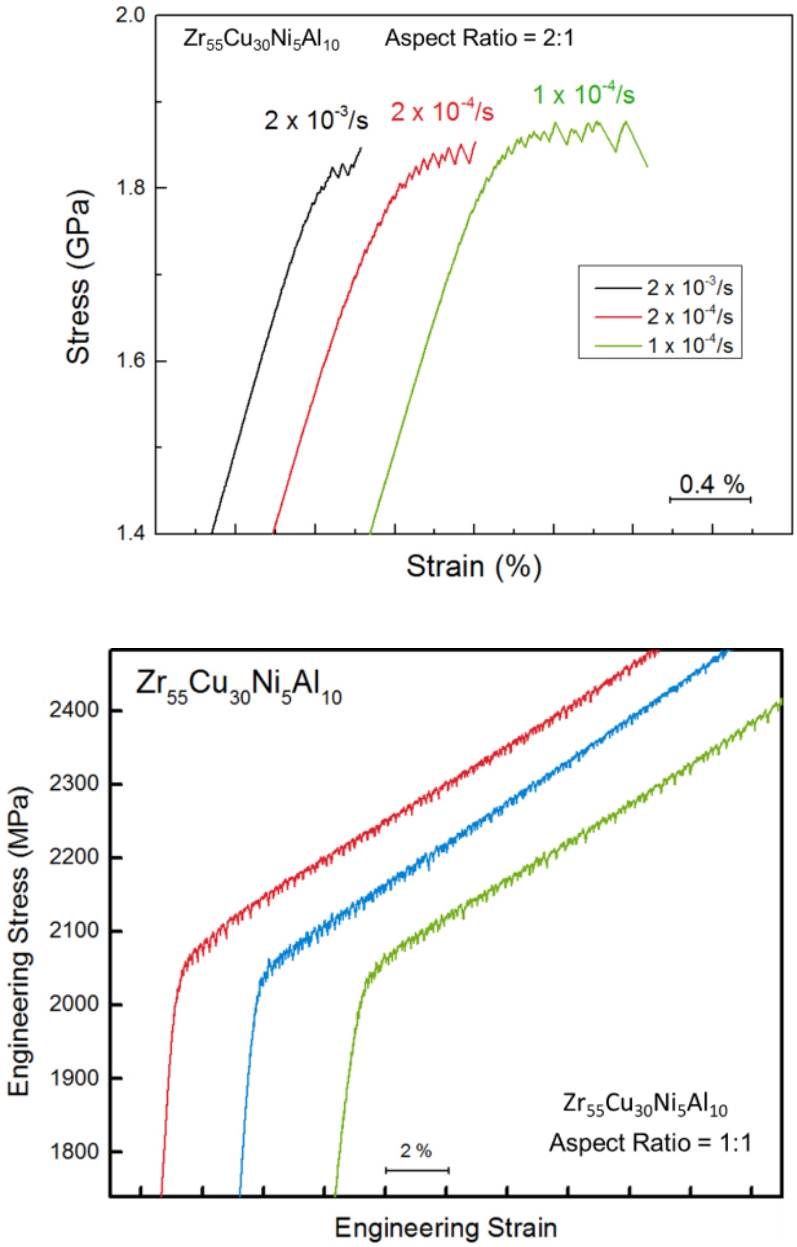

Figure 8. Compression experiments on $Zr_{55}Cu_{30}Ni_5Al_{10}$ BMG (atomic percent, at. %) at different strain levels under (a) unconstrained and (b) constrained conditions

dash-dot line in Figure 9a. On the lateral surface, shear bands only can be found at the corner of the specimen (Figure 9b), due to the stress concentration caused by the geometry during the loading process, implying a relatively brittle behavior. As a contrast, multiple shear bands appear on the lateral surface under the constrained case (Figure 10a), interacting with each other, and form different patterns at several regions, which indicate a ductile behavior. With a close look at these regions (Figure 10b), secondary and even tertiary shear bands can be observed and intersect with each other. The extensive shear bands consumed most energy generated during deformation, and prevented the fracture with the support of the platen.

The morphology of a lateral surface for $Zr_{64.13}Cu_{15.75}Ni_{10.12}Al_{10}$ after compressive fracture is described in Figure 11a. Multiple primary shear bands can be found, denoted by the short white arrows, and their slip direction is indicated by the long white arrow. With a closer look at the adjacent region of the fracture plane, which is marked by a rectangular in Figure 11a, secondary shear bands can be located by the short white arrows in Figure 11b. Furthermore, intensive interactions of shear bands appear in the lower-right part of the figure. The shear-band initiation, propagation, and arrest, including the interaction between different shear bands, are expected to contribute to the serration events, and these processes are closely related to the characteristics in deformation, such as the stress drop in the stress-strain curve.

3.3.3 Nanoindenation

The results are shown in Figure 12. By summarize all the data obtained from five tests, the pop-in size shows a decreasing trend as time goes on. If we plot the time-based

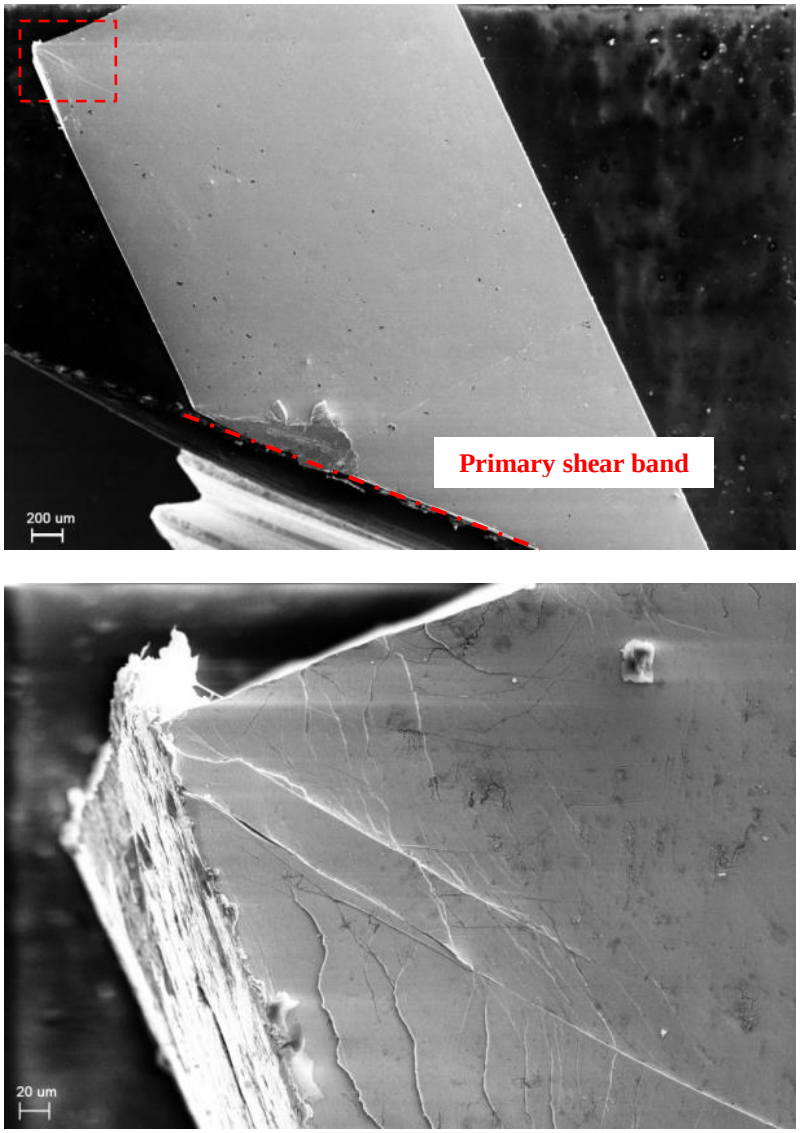

Figure 9. (a) SEM image showing the primary shear bands (fracture plane, indicated as red dash-dot line) on the lateral surface after *unconstrained compression* at the strain rate of 2×10^{-4}/s, and (b) the amplified region showing the interaction of shear bands, much less than the constrained case

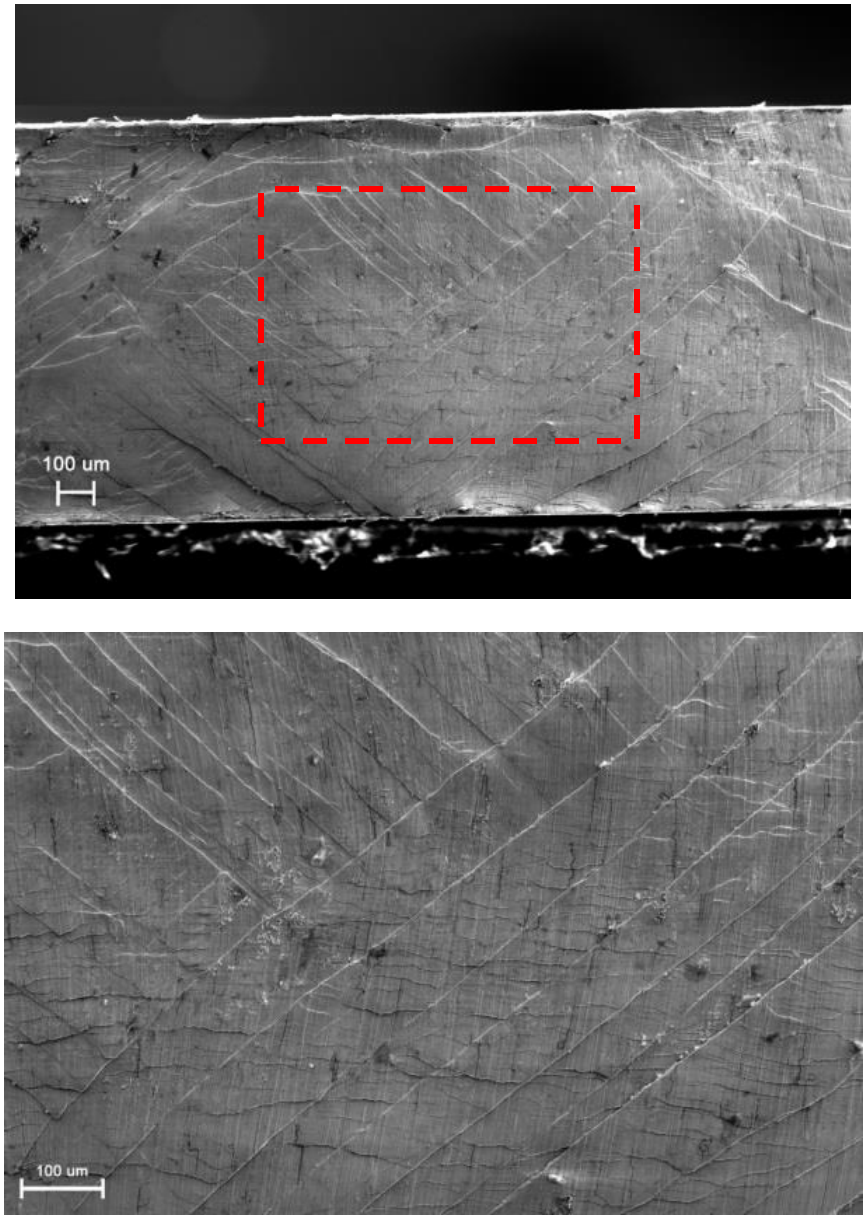

Figure 10. (a) SEM image showing the multiple shear bands on the lateral surface after constrained compression at strain rate of 2 × 10^{-4}/s and (b) the amplified region showing the interaction of shear bands

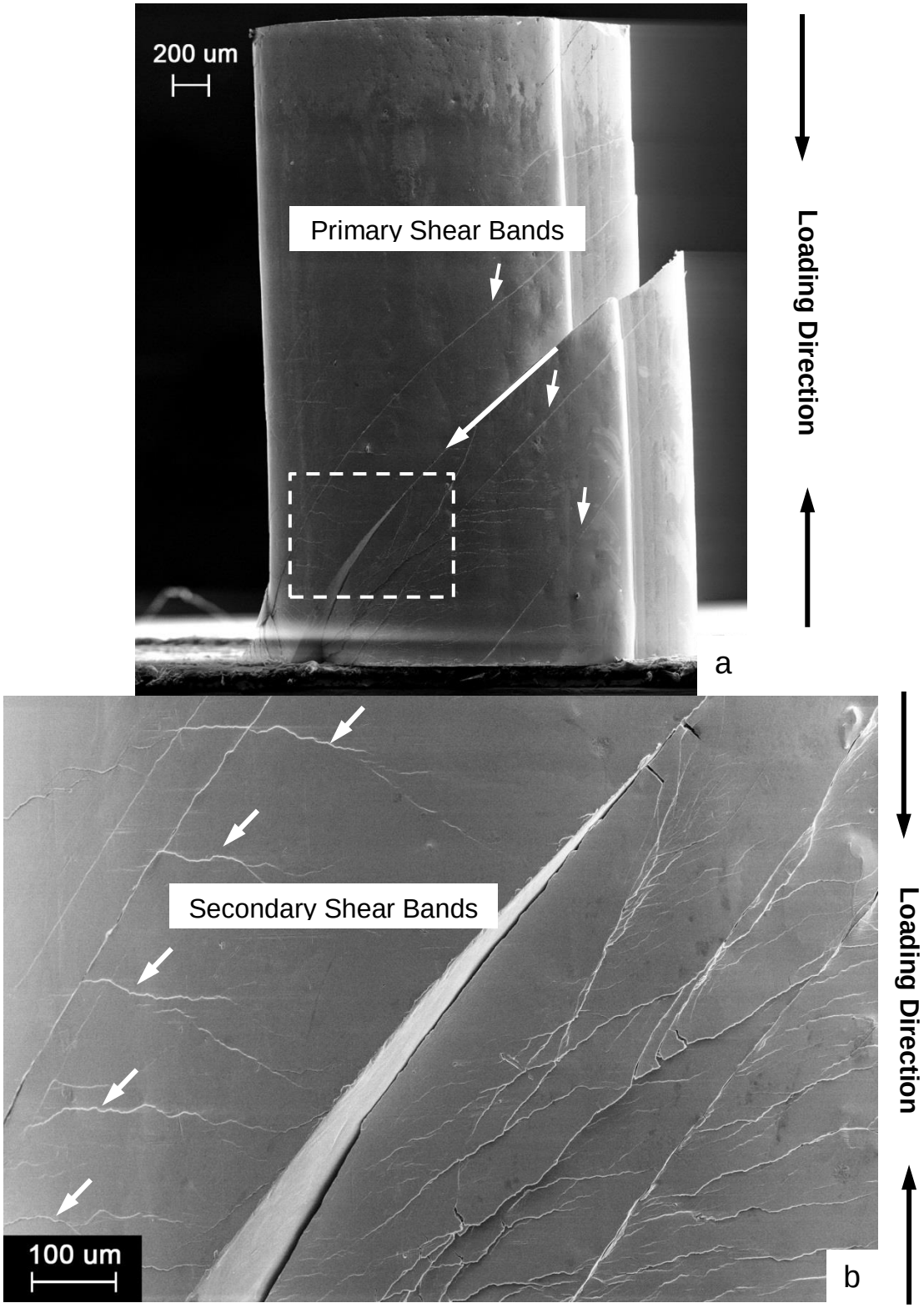

Figure 11. (a) Lateral surface of a fractured BMG sample, $Zr_{64.13}Cu_{15.75}Ni_{10.12}Al_{10}$, after compression at a strain rate of 5×10^{-5} s^{-1}, and (b) magnified region indicated by a rectangle in (a) showing the interaction of multiple shear bands

regional mean value and the corresponding standard deviation, it's much clear that pop-in size is decreasing as the depth increases. Intuitively, one can relate this phenomenon to the above discussed constrained condition. Indeed, the geometrical constraint also can be applied on nanoindentation. Using Berkovich-type three-sided pyramidal diamond indenter, the deformation caused by nanoindentation is actually localized. Previous studies from both experimental and finite element modeling have confirmed the shear-band patterns in the nanoindentation tests. The cross shape of shear-band pattern surrounding the indented points indicated that the deformation is high constrained in the local region. Therefore, the serration trend obtained also works here in the nanoindentation case. By categorizing the feature of serration trend, it's to especially useful to deduce the type of loading condition under which the BMG deforms, and it's also very helpful for us to study the shear-band evolution under new loading conditions. Interesting, the maximum pop-in in this study was found at the position of 2nd or 3rd or 5th, which implies that the shear band initiation actually takes some time, and then suddenly propagates which leads to the max. size.

3.4 Discussion

3.4.1 Statistical analysis of serration characteristics

The stick-slip behavior is composed by many slips. Two curves, stress versus time (S-T) and displacement versus time (D-T), are shown in Figure 13, in order to exhibit their correspondence on stick-slip behavior. Four statistical characteristics were analyzed

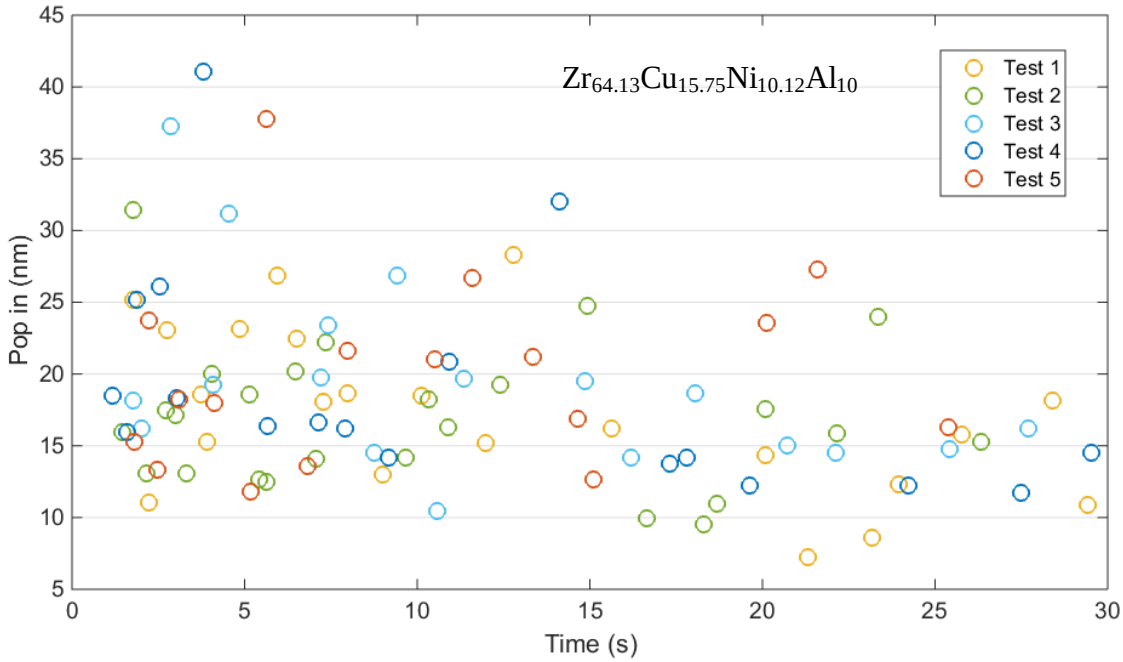

Figure 12. The distribution of Pop-ins extracted from the load-depth curve of nanoindentation experiment in five tests

in this study, namely stress drop, waiting time, slip duration, and displacement burst. Stress drop is defined as difference between the largest and lowest stresses in one slip event. The slip duration is the time duration for one slip. The waiting time is the time interval between the end of one slip and the beginning of the next slip. All these three variables are defined in the S-T curve. Displacement burst is the magnitude of the displacement jump in the displacement-time curve.

Based on the compression results, two curves, S-T and D-T, can be extracted. Even though the compression experiment is controlled by displacement, the displacement burst shows clearly as an indicator of each slip event. The stress drop and displacement burst are consistent with each other for the large slip. However, the S-T curve is more sensitive to detect the minor-scale slip, since it is obvious as a small drop in the S-T curve but become indiscernible in the D-T curve (Figure 13) at the same time.

For each slip, it corresponds to the initiation, propagation and arrest of shear bands. At the end of each slip, the shear band is hindered by some obstacles, such as solid-like sites in BMGs [20, 114-116]. During the waiting time, the elastic energy is accumulated to a critical point, and then released when the slip occurs, leading to a significant temperature rise within shear bands. The accumulated energy will behave in the form of heat dissipation and microstructural changes, when the shear bands propagate again.

The results for the analysis of stress drop, waiting time, slip duration, and displacement burst under unconstrained and constrained conditions are shown in Figure 14. Interestingly, the stress drop shows an increasing trend with time under unconstrained

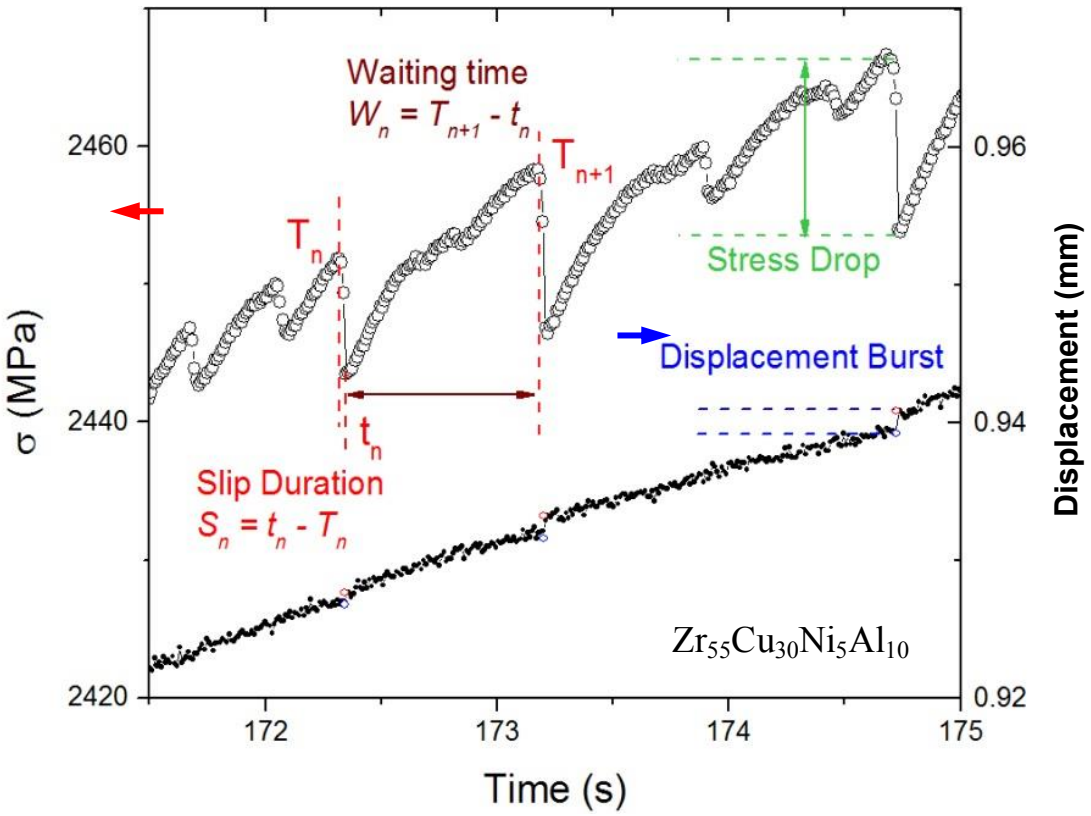

Figure 13. Definition of stress drop, waiting time, slip duration, and displacement burst during serration events, which can be observed in stress-time and displacement-time curves, respectively.

condition, but the opposite behavior under constrained condition. With a larger strain rate, stress drop decreases under both conditions. For the constrained case, the magnitude of stress drop reaches maximum after yielding point, and decreases greatly with time (Figure 14b). Strain rate plays an important role on the maximum stress drop. Slower strain rate causes a larger maximum stress drop.

Waiting time scatters with time under both conditions. But with a careful investigation, waiting time seems to have a slight decreasing trend under unconstrained condition (Figure 14c), and a slight increasing trend for constrained case (Figure 14d). More experiments needed to identify this issue. Nevertheless, waiting time decreases with strain rate increases. It's reasonable because the responding time increases when the loading rate decreases.

For slip duration, it increases slightly with time under constrained condition (Figure 14e), but scatters with time under unconstrained case (Figure 14f). Except this difference, the average magnitude of slip duration seems to be within 0.04 s to 0.06 s for both conditions, that's to say, slip duration doesn't change too much under various strain rates and different sample geometries. Compared to the large difference for waiting time, this fact strongly suggests that shear-band operation is not affected by the external loading conditions, and exhibits as an intrinsic behavior.

The displacement burst shows a clear increasing trend with time for the unconstrained condition (Figure 14g), and decreasing trend for the constrained case (Figure 14h). Meanwhile, increasing strain rate will decrease the slip size. This trend is consistent with that of stress drop, and demonstrates again that stress drop and

displacement burst have corresponding relation. For a convenient comparison, all the above results are summarized in Table 1.

As shown above, the study of stick-slip behavior under different conditions reveals the underlying order for deformation in BMGs. All the findings will be applied in the following study in the laser-treated samples. We expected to uncover the mechanism of plasticity improvement induce by laser shock peening and by investigating the stick-slip behavior.

3.4.2 Comparison using slip-avalanche models

Figure 3 The axes were rescaled by changing κ and λ until the distributions lie on top of each other. For this collapse, it was found that $\kappa = 1.42 \pm 0.20$, and $\lambda = 0.22 \pm 0.02$. The collapse function in Figure 3 is the scaling function, $C'(x)$, of Equation (2). Plugging this information into Equation (2) then predicts the scaling behavior of the slip-avalanche-size distribution for other strain rates as well. Note that for the higher strain rates, the samples break before they reach the steady state — Figure 2 shows that the stress versus time plots have no flat region for strain rates of 2×10^{-4} and 1×10^{-3} s^{-1}.

3.5 Summary

The geometrical-constraint study gives very useful information about the serration dynamics. It provides an easy method to distinguish the plasticity from sample intrinsic properties or from the combination of sample and machine frame. Specifically, under the unconstrained condition, which is the standard for compression tests, the stress drop and

Figure 14. (a, b) Stress drop versus time, (c, d) waiting time versus time, (e, f) slip duration versus time, (g, h) displacement burst versus time for (a, c, e, g) unconstrained and (b, d, f, h) constrained conditions

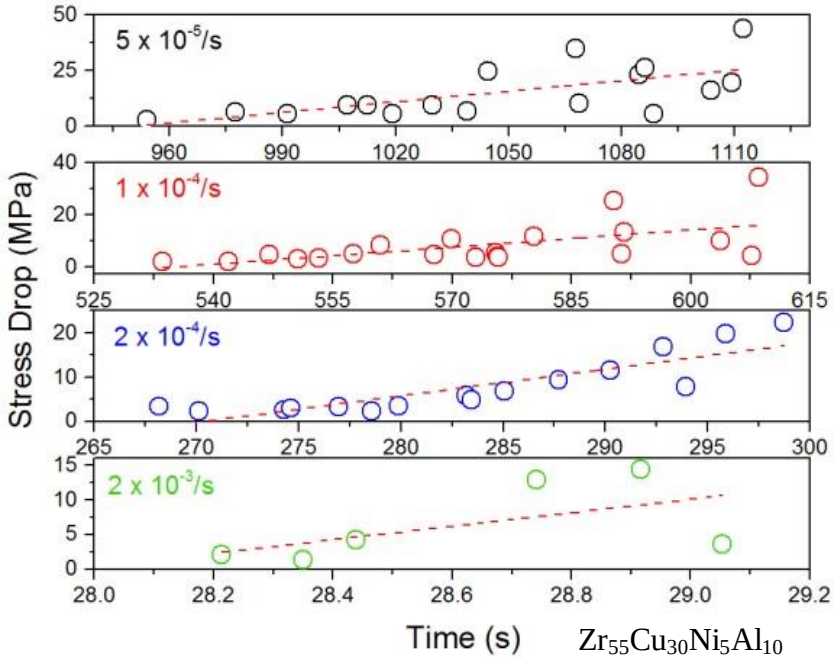

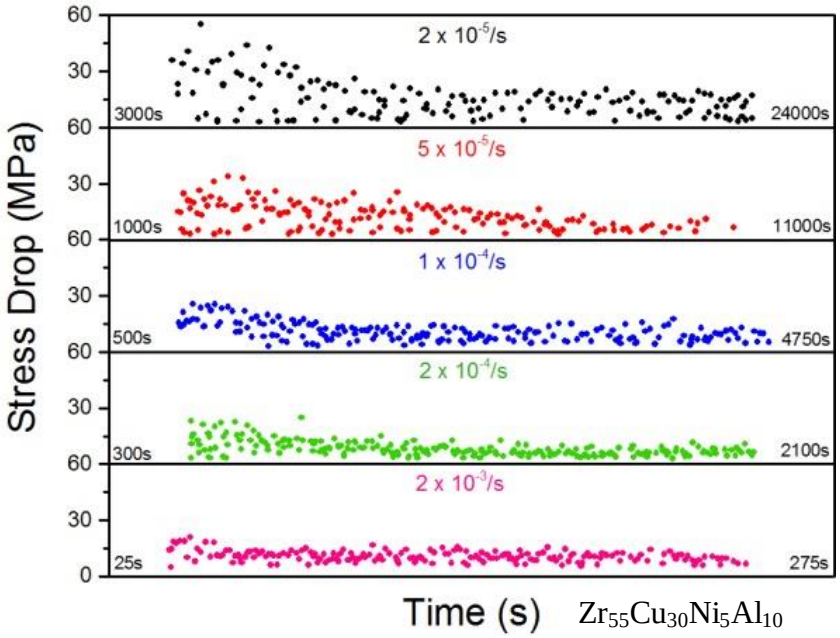

Figure 14 continued

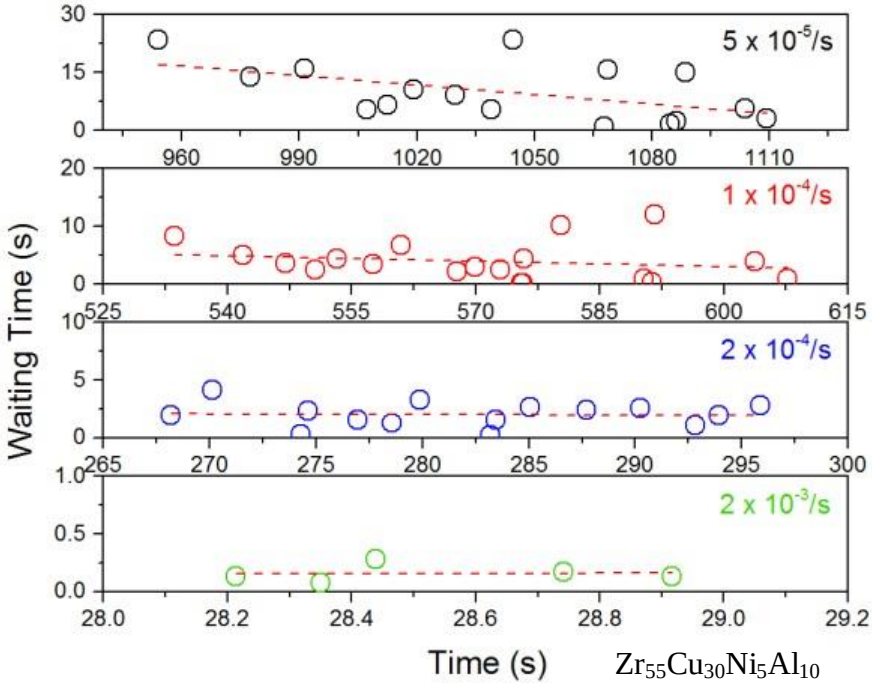

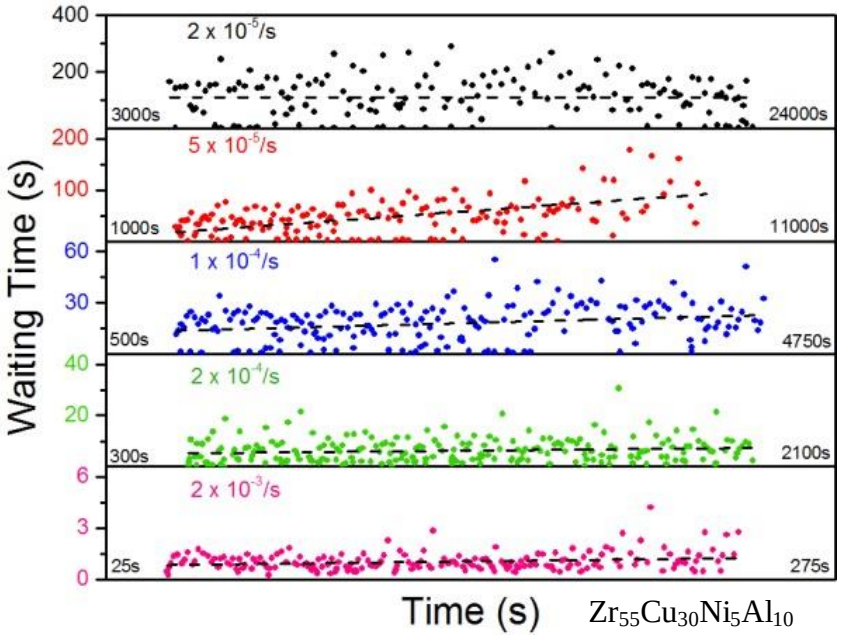

Figure 14 continued

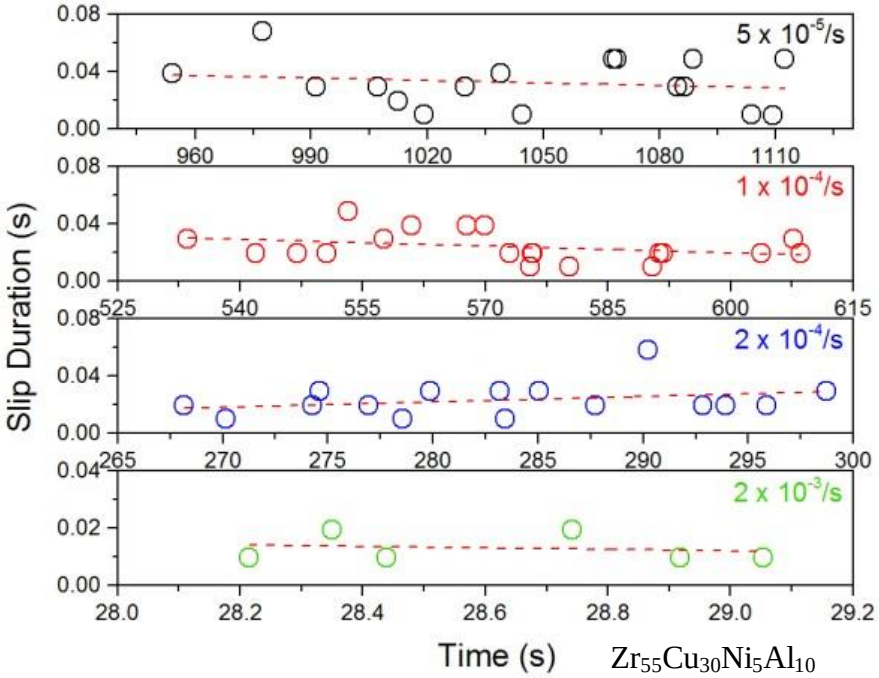

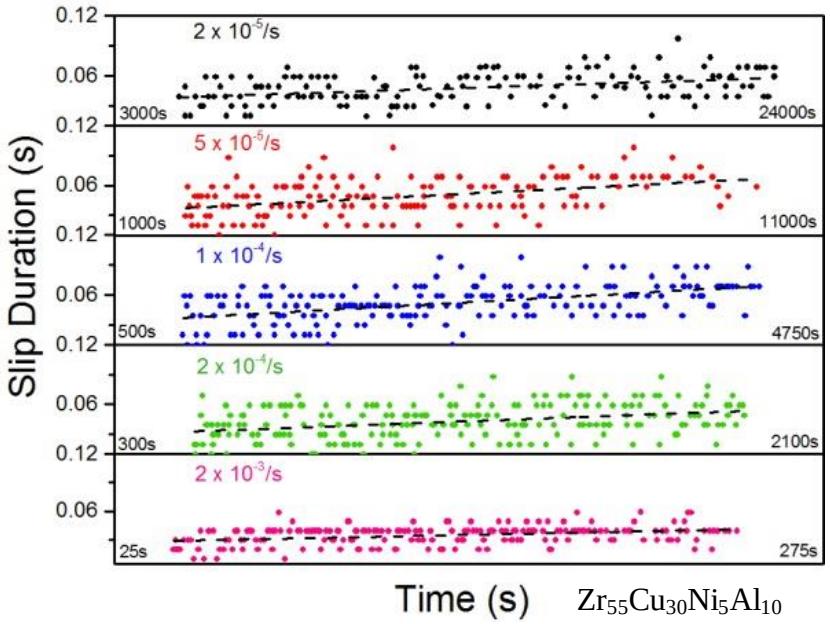

Figure 14 continued

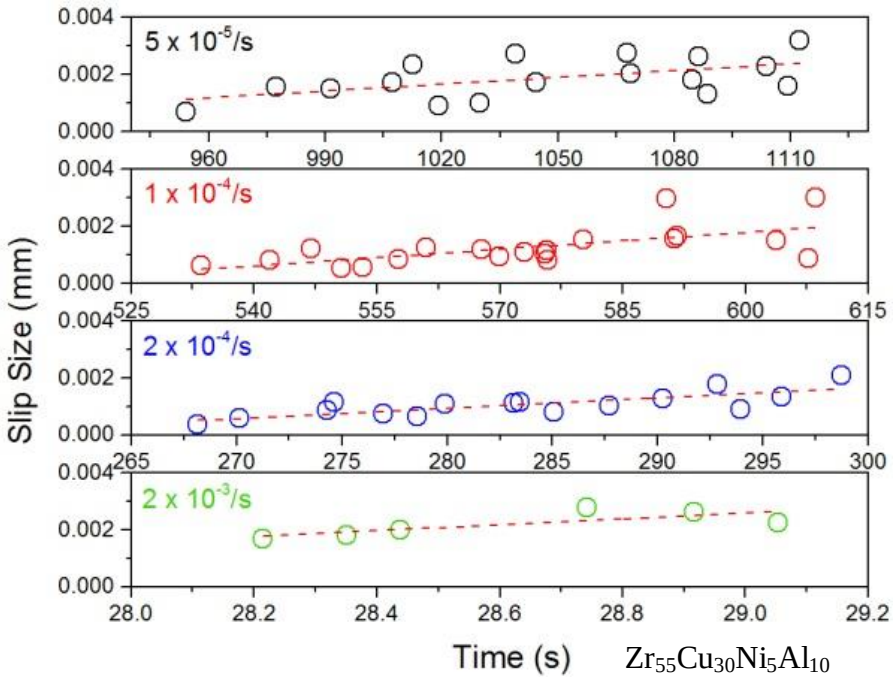

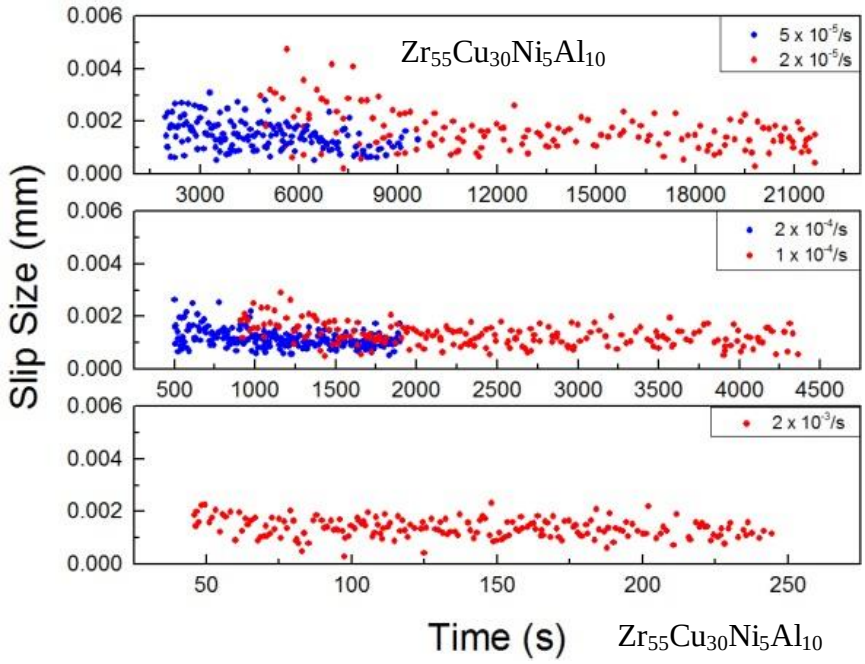

Figure 14 continued

Table 1. Summary of the stick-slip behavior under different strain rates and sample geometries, red texts marked for the difference, and black texts for the similarity

	Unconstrained	**Constrained**
Stress Drop (D)	❖ Increases with time; ❖ D_{max} decreases as strain rate increases	❖ Decreases with time; ❖ D_{max} decreases as strain rate increases
Waiting Time (W)	❖ Slightly decreases with time; ❖ Decreases as strain rate increases	❖ Slightly increases with time; ❖ Decreases as strain rate increases
Slip Duration (S)	❖ Slightly decreases with time; ❖ Slightly decreases as strain rate increases	❖ Increases with time; ❖ Slightly decreases as strain rate increases
Displacement	❖ Increases with time; ❖ Decreases as strain rate increases	❖ Decreases with time; ❖ Decreases as strain rate increases

Table 2. Possible reasons for the different serration behavior in the unconstrained and constrained conditions

	Unconstrained Condition	Constrained Condition
Strain-Rate Effect	❖ As the strain rate decreases, i.e., a slower loading, the response time to accommodate deformation increases. Thus, the stress drop and displacement burst increase, for both unconstrained and constrained conditions; ❖ Our slip-avalanche model predicts the largest slip sizes and slip duration for the lowest strain rates	
Time Effect	❖ The system has no freedom to slip through the entire sample, i.e., the boundary conditions constrain the slips; ❖ This constraint is increasingly the case, since the system becomes more compressed; ❖ Therefore, stress drop and displacement burst become smaller, because there is less and less room for a slip to propagate before it runs into a boundary of the sample.	❖ There is no such boundary effect as in the constrained case; ❖ The slips become larger as the sample becomes slightly weakened by previous slip activities; ❖ Therefore, stress drop and displacement burst increase with time.

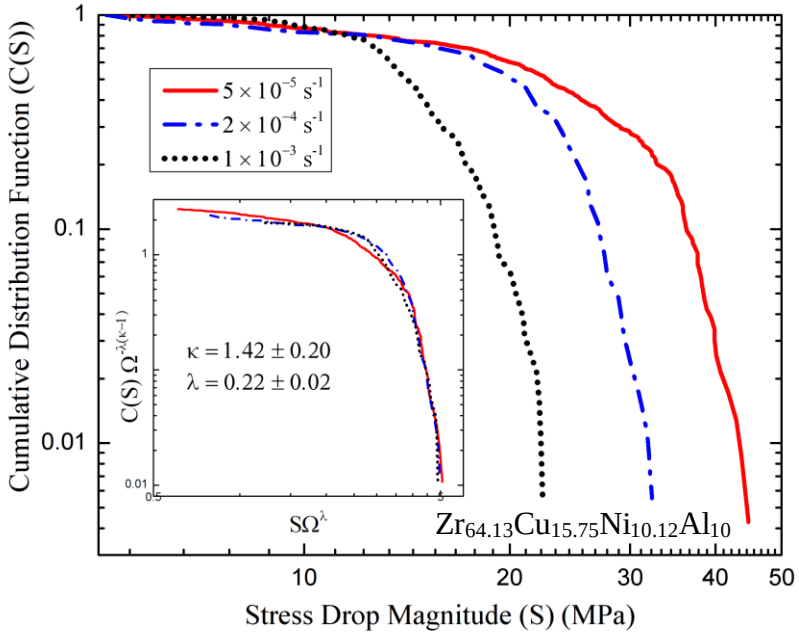

Figure 15. CCDF for the magnitude of stress drop at different strain rates for the $Zr_{64.13}Cu_{15.75}Ni_{10.12}Al_{10}$ BMG under the unconstrained condition, and inset shows the Widom scaling collapse of the curves (cooperated with Mr. J. Antonaglia and Prof. Karin A. Dahmen, reprinted from [117])

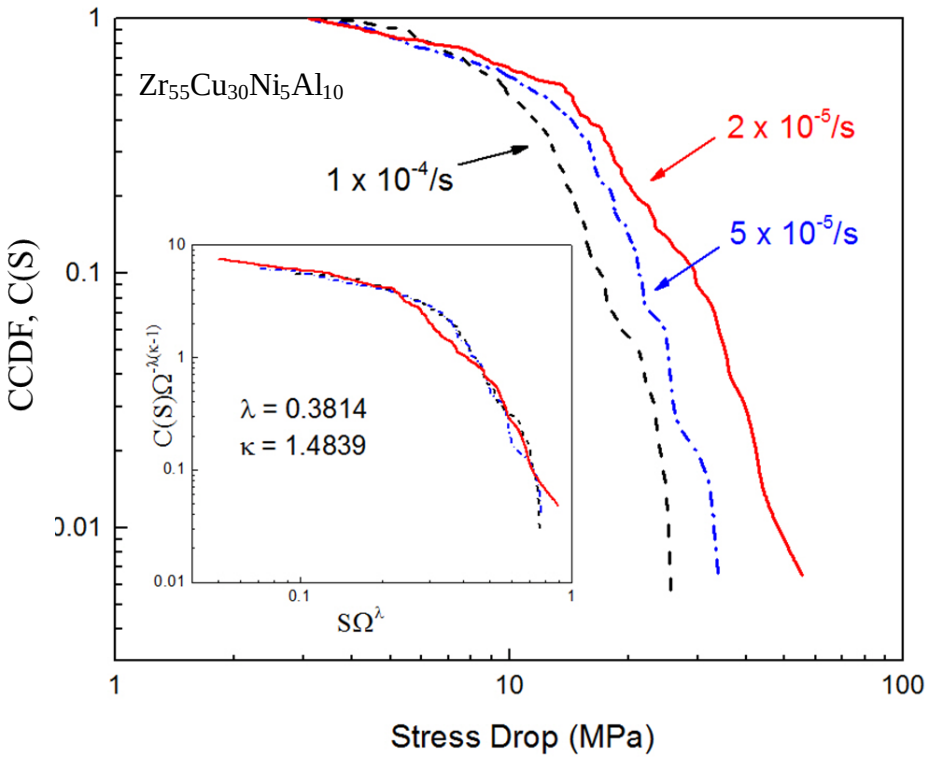

Figure 16. CCDF for the magnitude of stress drop at different strain rates for the $Zr_{55}Cu_{30}Ni_5Al_{10}$ BMG under the constrained condition, and inset shows the Widom scaling collapse of the curves

displacement burst will keep increasing as the system has no boundary constrained for shear band propagation. In contrast, the decreasing trend can be found in the constrained condition, both for the stress drop and displacement burst, implying that the system actually prevents the propagation of shear bands and avoid the catastrophic fracture. Huge shear bands interactions can be observed on the lateral surface of compressed sample under constrained condition, which is responsible for the prolonged plasticity. While only several shear bands can be found in the fractured sample under unconstrained condition. The slip duration and waiting time didn't show strong trend under both unconstrained and constrained conditions at various strain rates. The features of trend were successfully applied in the case of nanoindentation, where the deformation is localized and constrained by the surrounding bulk materials, and good agreement was achieved between the constrained trend and stress-drop pattern from pop-ins.

CHAPTER IV EFFECTS OF PRE-FATIGUE ON THE COMPRESSIVE BEHAVIOR

4.1 Introduction

As discussed in Sect. 1.1 and shown in Figure 17, recent work has reported that weak spots or anelastic sites occupy a large volume proportion in BMGs using the synchrotron diffraction and amplitude-modulation dynamic atomic-force microscopy [116]. From the energy-dissipation map presented in Figure 17, weak spots (liquid-like regions) can be easily identified. It should be pointed out that the correlation length of the heterogeneity equals ~ 2 nm, which is in good agreement with the size of STZs. Furthermore, STZ dynamic simulations, based on the kinetic Monte Carlo method, have been performed to study the interaction between STZs during deformation in BMGs[28]. The results clearly show that at low stress levels, these STZs will behave separately, which corresponds to the elastic-deformation mode. When the stress exceeds a critical value, the activation of one STZ will induce the subsequent STZ activation in its immediate neighborhood, i.e., the slip of one weak spot triggers other weak spots to slip. Thus, in this section, the pre-fatigue induced "damage" at these weak spots will be investigated, and the influence of these "damage" will be studied during compression experiments and characterized using synchrotron X-ray diffraction method.

4.2 Experimental Methods

4.2.1 Sample preparation

Two kinds of BMGs, $Zr_{50}Cu_{40}Al_{10}$ and $Zr_{64.13}Cu_{15.75}Ni_{10.12}Al_{10}$ (atomic percent, at.%), are used in the present study. By arc-melting the mixture of constituent metals with

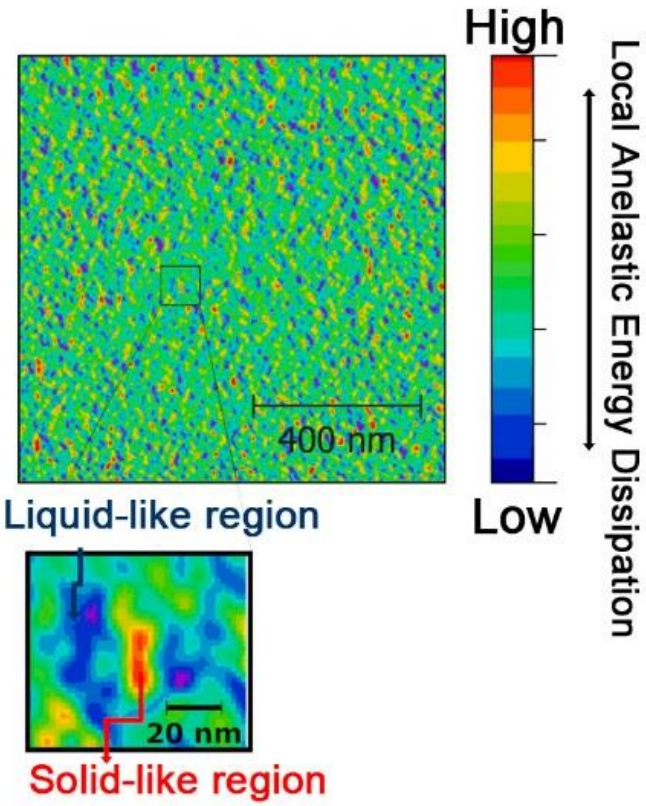

Figure 17. The energy-dissipation map obtained via the amplitude-modulation dynamic atomic-force-microscopy (AM-AFM) scanning of the $Zr_{70}Ni_{30}$ metallic-glass thin film, and the inset showing the liquid-like region (weak spots) and solid-like region (reprinted from [116])

purity higher than 99.9 weight percent in a Ti-gettered high-purity argon atmosphere, the specimen is obtained through suction casting into a water-cooled copper mold to form a cylindrical cast ingot with ~ 60 mm in length and 2 mm in diameter. The ingot is then cut into cylindrical rods with 4 mm in length. Two compressive sides are carefully polished to be parallel.

The master-alloy ingots of the quaternary Zr-Cu-Al alloys were prepared by arc-melting a mixture of pure Zr (> 99%), Cu (99.999%), and Al (99.999%) metals in an argon atmosphere. Iodic refine processed Zr metal (oxygen concentration less than 300 mass ppm) was used in this study to maintain the low oxygen concentration level of cast rods less than about 1000 mass ppm [118]. The arc tilt-casting furnace is characterized by having two arc torches: one is for the alloy melting, and the other rehear for the pouring molten alloy to achieve fully melting state just before casting [119]. In addition, since the surface area of molten alloy is not significantly changed during the casting, we can fabricate high quality cast glassy rods by suppressing the formation of cast defects as exemplified cold shuts.

4.2.2 Fatigue-compression tests

Fatigue-compression experiment is designed for this study. The specimens were tested in the compression-compression fatigue experiments first. Instead of running to failure, the tests were stopped at different fatigue cycles (10^4, 10^5, and 10^6 cycles in this study). Then uniaxial compression experiments were conducted on these pre-fatigued specimens together with the as-cast specimen at a constant strain rate. All samples were

compressed to failure, and their stress-strain curves were recorded. Specifically, the stress range of fatigue tests is set to 1,100 MPa under compression-compression loading conditions. The load ratio, R (where $R = \sigma_{min}/\sigma_{max}$, and σ_{min} and σ_{max} are the applied minimum and maximum stresses, respectively), is 0.1 under a load-control mode using a sinusoidal waveform at a frequency of 10 Hz. During the compression experiments, the initial strain rate is 5×10^{-5}/s, and a data acquisition rate of 100 Hz is employed. To simplify, the as-cast $Zr_{64.13}Cu_{15.75}Ni_{10.12}Al_{10}$ samples, along with ones after 10^4, 10^5, and 10^6 fatigue cycles, will be marked as S1, S4, S5, and S6, respectively, thereafter.

4.2.3 Characterization through synchrotron X-ray diffraction

The diffraction pattern was obtained at the beamline 11-ID-C in the Advanced Photon Source (APS) of the Argonne National Laboratory. The BMG samples, $Zr_{64.13}Cu_{15.75}Ni_{10.12}Al_{10}$, with 10^4, 10^5, and 10^6 cycles pre-fatigue, followed by the compression experiment, were prepared before synchrotron experiment. Since the fatigue may affect local anelastic sites through the whole sample, the diffraction patterns was measured along the center line on the surface of these samples. The beam size is set to 0.2 mm × 0.5 mm, and 18 points were chosen as the incident locations. The setup of synchrotron experiments is described in Figure 18. A load frame and a compression cell are used to perform in-situ diffraction experiment.

4.3 Results

The results of compression experiments are shown in Figure 19. It's evident that fatigue processing prolongs the plastic region of both BMGs in the subsequent

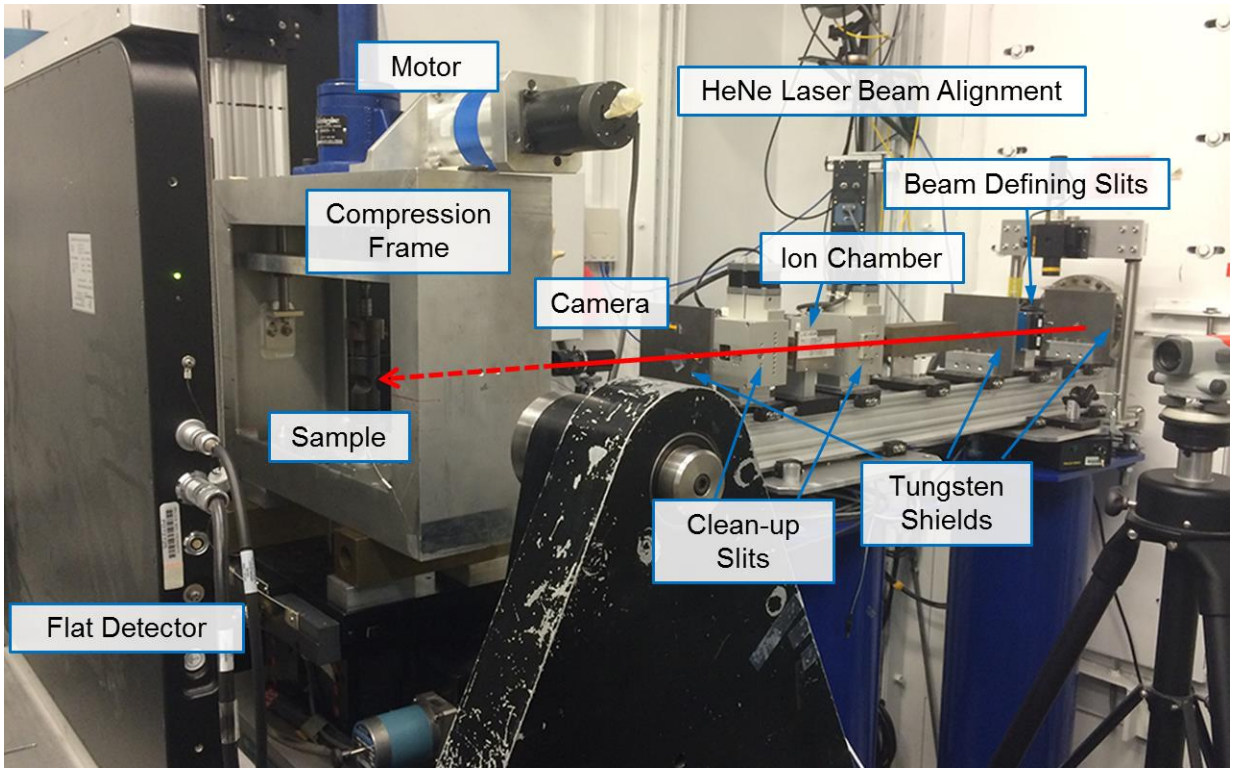

Figure 18. The setup for the synchrotron experiments at the beamline, 11-ID-C, Advanced Photon Source (APS), Argonne National Laboratory

compression experiments. Interestingly, as the fatigue cycles increase, the improvement for the ductility becomes more prominent. However, we notice that the samples pre-fatigued at 10^4 cycles do not show significant difference to the as-cast samples. Compared to $Zr_{50}Cu_{40}Al_{10}$, $Zr_{64.13}Cu_{15.75}Ni_{10.12}Al_{10}$ shows a larger improvement, which may attribute to their inherently ductile properties and the sample-size effects. To clearly visualize the improvement, the plastic strain for each specimen was plotted in Figure 20, and error bar was added to include all tested samples. The improvement for $Zr_{50}Cu_{40}Al_{10}$ BMGs from as-cast to 10^6 cycles loaded is only 0.24%, and the whole level of all plastic strains still stays near zero. For S1 and S4, the average values are similar, around 2.00%. But for S5, the average strain is 2.64% and the maximum is 4.11%, showing an increment of 0.75% compared to S1 for the average value. For S6, further improvement was obtained, with a maximum of 5.53% and an average of 3.55%. It should be noted that during the fatigue experiments, the situation where specimens break and cannot reach the designed cycle number exists. Even for the samples tested in the same pre-fatigue condition, the variation in the ductility improvement indeed. The fluctuation in the fatigue-compression experiments may be resulted from the variation of free volume for different samples, which could dramatically affect the fatigue behavior and the consequent compression results [120, 121]. Nevertheless, the results are informative and promote the following study using synchrotron X-ray diffraction for the structural characterization.

The samples break into two parts after catastrophic fracture, and the fracture morphology was examined by the scanning electron microscopy (SEM). Figure 21 presents the features of fractography for S6, including the lateral surface region below the

shear surface, and the inset showing the whole fractured sample. Typical feature of the shear surface was observed in the samples, that is, a smooth region and vein-like pattern [122, 123]. The direction of primary shear-band propagation is marked by the black arrow in the inset. As magnified in Figure 21, extensive shear bands interact with each other on the lateral surface, which is denoted by the black arrows, and form a network composing of secondary and even ternary shear bands.

4.4 Discussion

It has been noticed that the serration flow for BMGs could be divided into two stages in terms of the magnitude of stress drop (or displacement burst, elastic energy density) [124, 125], and the serration behavior has been found to be closely related to the operation of shear bands, which creates striation patterns (shear steps) on the fracture plane, with one shear step corresponding to one stress drop [122, 126-128]. Furthermore, as the magnitude of stress drop keeps increasing after the onset of yielding, the striation spacing is increasing as well [122], implying that the sample is continuously weakened by the previous shear-band activities during the deformation process. Thus, through the investigation of stress drops, it provides an effective way to study the shear-band operations. Figure 22 presents the stress-drop pattern for $Zr_{64.13}Cu_{15.75}Ni_{10.12}Al_{10}$ BMGs after various fatigue cycles. Two stages can be easily identified for all samples with respect to the magnitude of stress drop, marked by the dashed lines in Figure 22, which is approximately located around the yielding point of the stress-strain curve, as used in previous work [124]. However, a close examination reveals a subtle difference in Stage 1.

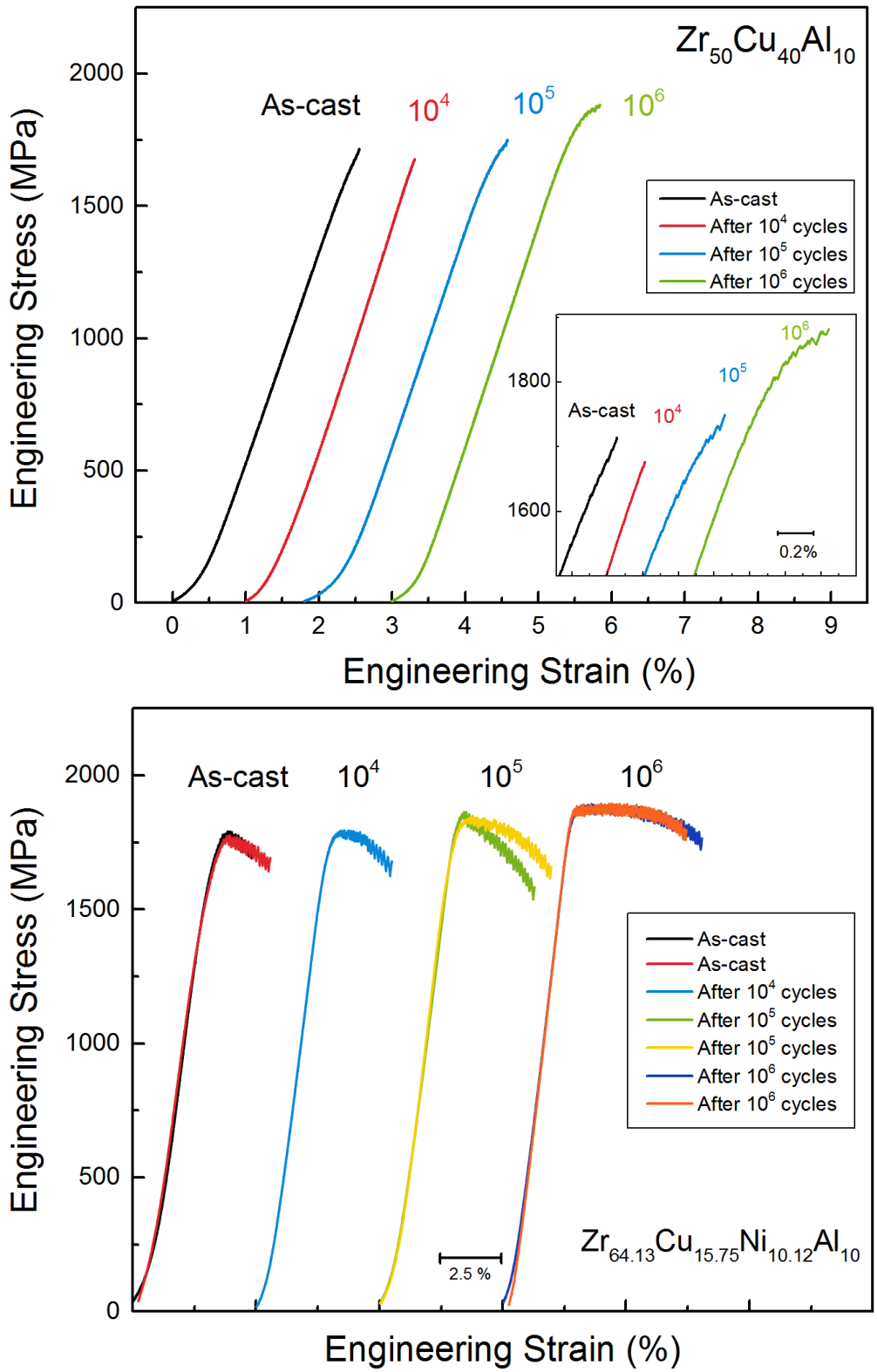

Figure 19. The compressive stress-strain curves for (a) $Zr_{50}Cu_{40}Al_{10}$ and (b) $Zr_{64.13}Cu_{15.75}Ni_{10.12}Al_{10}$ BMGs after different fatigue cycles, compared to as-cast samples.

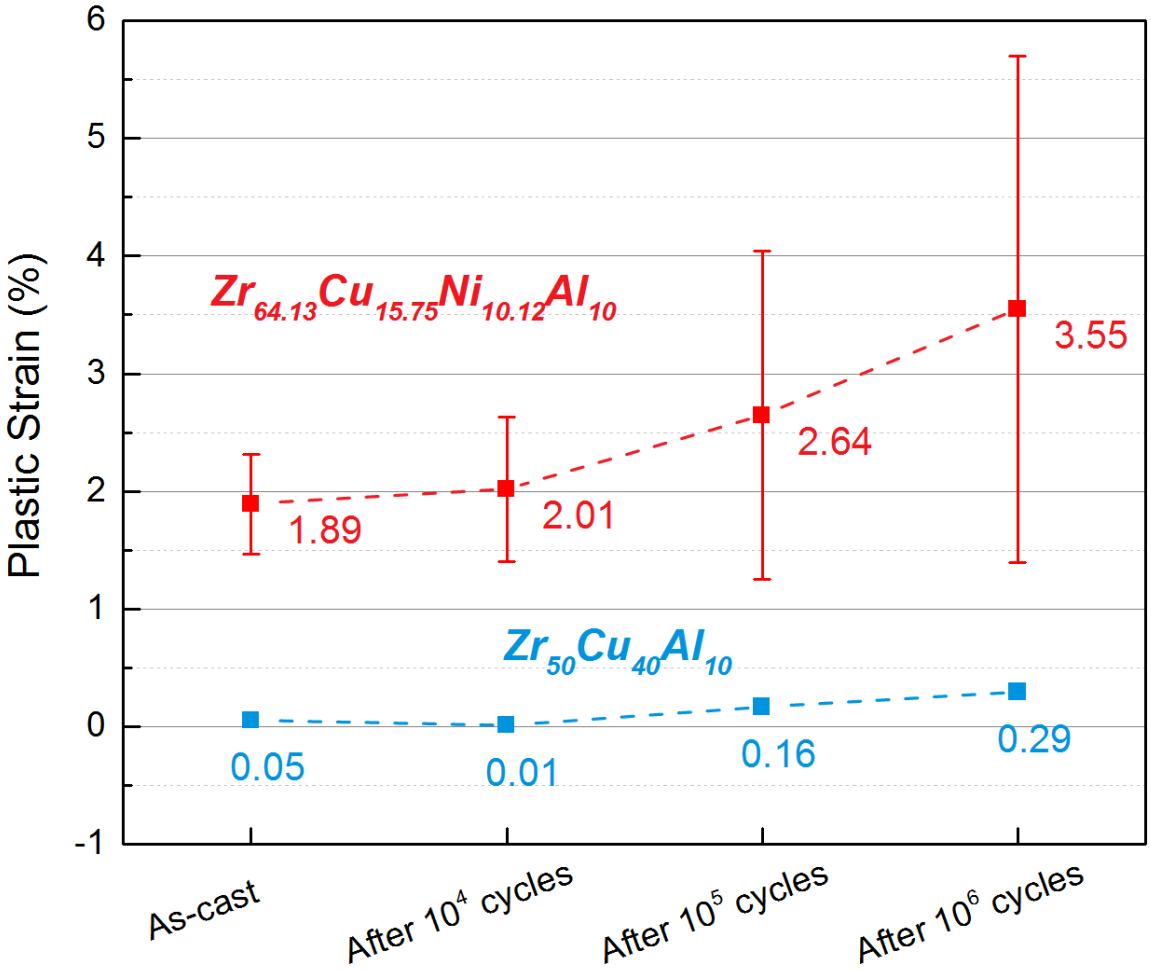

Figure 20. Compressive plastic strains of Zr50Cu40Al10 and Zr64.13Cu15.75Ni10.12Al10 BMGs after different fatigue cycles

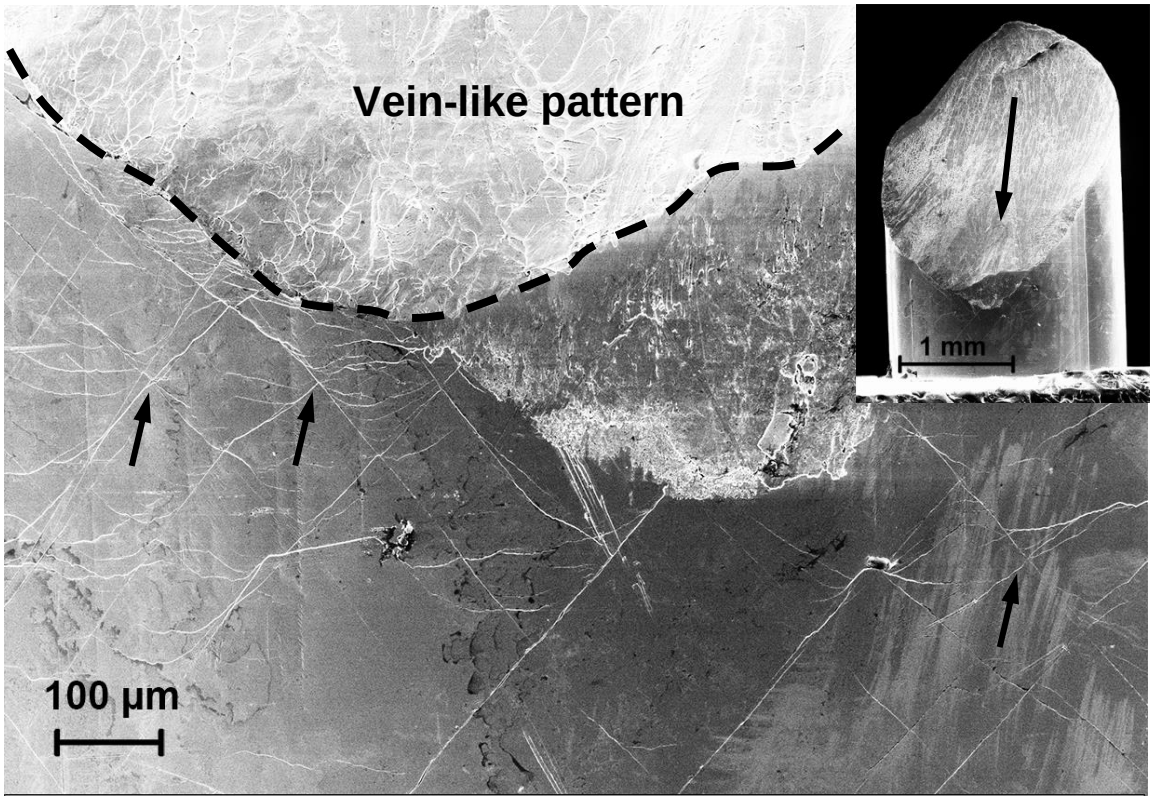

Figure 21. Morphology of compressively fractured $Zr_{64.13}Cu_{15.75}Ni_{10.12}Al_{10}$ specimen after 10^6 cycles of fatigue load. On the lateral surface, the network of primary, secondary and tertiary shear bands can be identified. Black arrows indicate the intersection of shear bands, and the black arrow in the inset shows the direction of primary shear-band propagation.

For as-cast, S4, and one of yellow S5 (right curve in Figure 22) samples, Stage 1 seems to last longer and compose of a large number of small stress drops (37 and 49 for as-cast, 32 for S4, 54 for yellow S5). By contrast, there are less stress drops for green S5 (17 drops, left curve in Figure 22) and S6 samples (20 and 13 drops). It's conceivable that the fatigue process has introduced structural changes even during the elastic loading region, and these changes are toward to the facilitation of the shear-band initiation. Thus, after the onset of yielding, all shear bands could be activated in a fast manner, which "stimulates" the deformation to proceed to Stage 2, i.e., the propagation of mature shear bands. This interprets the short period for Stage 1 of stress-drop pattern for the high-cycle fatigued samples. Furthermore, the formation of shear-band network could hinder the propagation of primary shear bands and prohibit the catastrophic fracture, as reported in previous works [129, 130]. As evidenced in Figure 21, shear bands are heavily branched and intersected, which indicates that the shortening of activation period of secondary or even tertiary shear bands promotes the interactions or intersections between them and the primary shear bands, and contributes to the enhanced ductility. In addition, from the stress-drop pattern, it implies that there is a threshold for the improvement of ductility for BMGs, and in the current work, the threshold of fatigue cycles lies between 10^5 and 10^6 for $Zr_{64.13}Cu_{15.75}Ni_{10.12}Al_{10}$ BMG. It's also worth pointing out that the maximum stress drop is around 70 ~ 80 MPa for all samples regardless of whether they are pre-fatigued or not.

4.5 Summary

With compression-compression fatigue processing, the compressive plasticity of BMG is improved. Furthermore, processing using various cycles leads to different extent of the

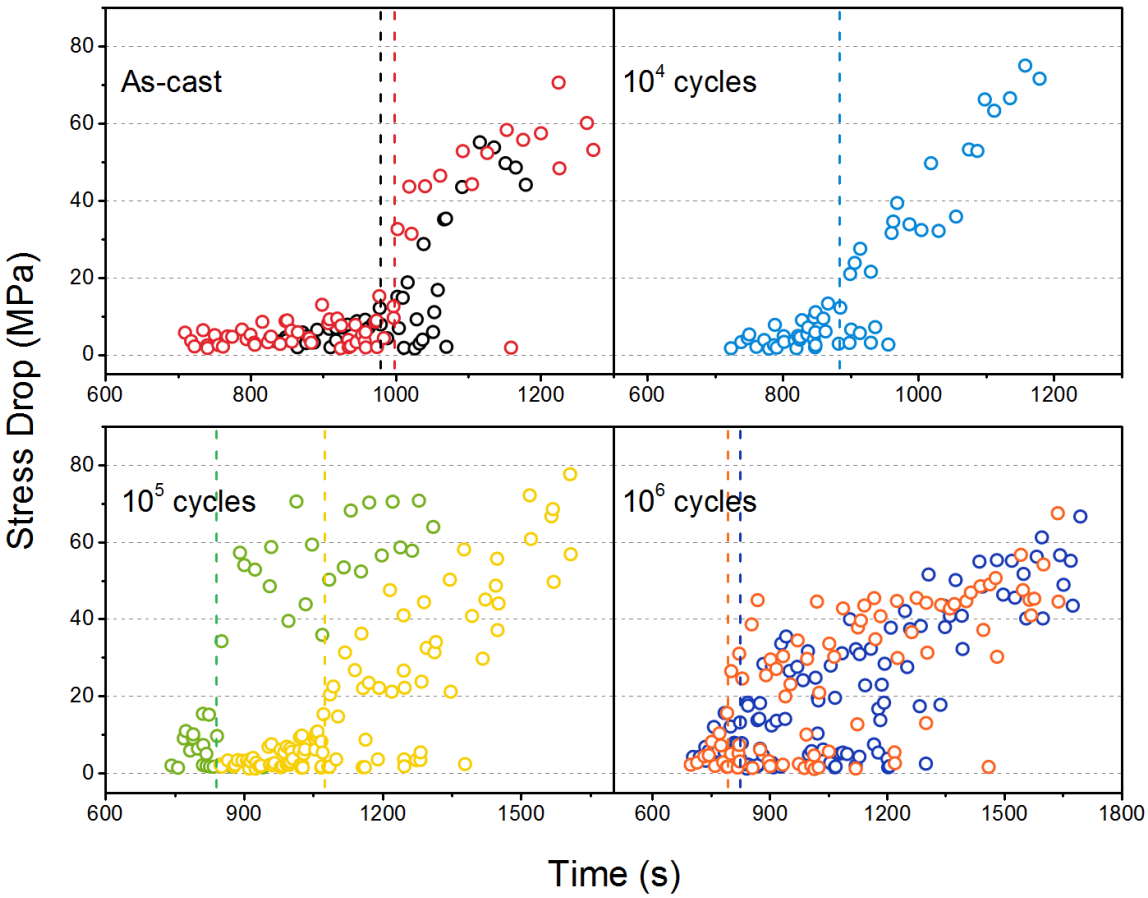

Figure 22. Stress-drop patterns for as-cast and pre-fatigued $Zr_{64.13}Cu_{15.75}Ni_{10.12}Al_{10}$ samples.

improvement. Different compositions also have effects on the improvement, e.g., more improvement can be found for a relatively ductile composition ($Zr_{64.13}Cu_{15.75}Ni_{10.12}Al_{10}$ in this study). Generally, 10^4 cycles didn't contribute to the improvement. From 10^5 cycles, discernible changes can be observed, and when increasing to 10^6 cycles, obvious improvement was obtained, compared to the results of as-cast sample, but large fluctuation of the plasticity is found during the repeated compression experiments. From the characterization of the fracture surface, huge shear-band network can be spotted on the S6 sample, which could result in the extended plasticity. With the statistical method, the stress-drop patterns for all samples are analyzed, and features for processing with different cycles can be distinguished. To investigate the local changes at the anelastic sites, synchrotron diffraction experiment is proposed. The synchrotron data is still being analyzed.

CHAPTER V LASER-INDUCED CONSTRAINT EFFECTS

5.1 Introduction

It was recently reported that the ductility of the Vitreloy 1 (Vit-1) BMG [$Zr_{41.25}Cu_{12.5}Ni_{10}Ti_{13.75}Be_{22.5}$, atomic percent (at.%)] can be improved by controlling residual stresses [131]. Shot-peened BMGs show increased plasticity in bending and compression due to the reduced likelihood of surface cracking and more homogeneous deformation induced by a high population of shear bands [131]. Compared with conventional shot peening which introduces residual stresses into distances of the order of hundreds of microns [132], the laser shock peening (LSP) process is capable of introducing residual stresses to much greater depths (millimeters) in metals and other materials [133, 134]. Several research activities have been done on metallic glasses using the laser surface treatment. To enhance mechanical properties, laser treatment can introduce crystalline phases and make the glassy alloys into BMG composites. For instance, Tariq et al. found that the surface hardness of BMGs can be altered by crystalline particles formed during the laser-pulse irradiation [135]. Wu et al. found that the plastic strain of the CuZr-based BMG is prolonged by the laser surface treatment through embedding micro- or nano-crystals [136]. Besides the above two cases, laser surface melting, along with the helium jet flow at high cooling rates, was reported to be capable of improving the compressive plasticity of BMGs without crystallization [137]. In present study, we will utilize a LSP process with water confinement and Al-coating to introduce compressive residual stresses into the BMG material, so as to investigate the extent to which this process can improve the plasticity of BMGs without introduction of crystalline phases under compression testing. This work is expected to provide an easy and effective way to prolong the ductility of intrinsic brittle BMGs. Besides, the LSP

process could introduce large magnitudes of residual stresses and leave a smooth surface, and can be automated and fully-developed in industry. By taking these advantages, the present work is expected to speed up the commercialization of BMGs, broaden their engineering application, and eventually facilitate our daily life with their unique properties.

5.2 Experimental Methods

5.2.1 Sample fabrication

The Zr-based BMG Vitreloy 105 (Vit-105, $Zr_{52.5}Cu_{17.9}Ni_{14.6}Al_{10.0}Ti_{5.0}$ in atomic percent, at.%) is chosen because it has been well documented in the literature and possesses good glass-forming ability [1, 138-142]. The samples were prepared by arc-melting mixtures of pure Zr, Cu, Ni, Al, and Ti metals in an argon atmosphere. The final rod shape is cast to 60 mm in length and 3 mm × 3 mm in cross-section. Then the rods are cut into rectangular bars having dimensions of 4 mm × 2 mm × 2 mm. After consecutively polishing using P600, P800, P1200, and P2500 grinding papers, the BMG-sample surface to be shock peened has the dimension of 4 mm × 2 mm.

5.2.2 Laser shock peening (LSP) procedure

(Cooperated with Dr. Yunfeng Cao and Prof. Yung C. Shin)

The 4 × 2 × 2 mm BMG sample was coated with an ablative Al tape before being placed into a water tank and shock peened using a laser wavelength of 1,064 nm and

pulse duration of 6 ns with the power densities from 5 GW/cm^2 to 10 GW/cm^2. The laser-beam diameter was set to about 1.25 mm, and the overlap ratio was selected to be 50%. Three consecutive tracks of peening were applied to the surface with a distance of 0.625 mm between track centerlines. In this study, specimens with one treated surface are used for residual-stress measurements and for comparison with model predictions, while all four surfaces were laser peened for the compression tests. Note that four-side peening may introduce the multi-axial residual stress by the shock wave on the measured surface and complicate the measurement. So one-side peening is performed to show a clear trend of the depth profile of residual stresses introduced by laser.

The setup of laser shock peening (LSP) is shown in Figure 23. The movement of the workpiece along the x and y directions was controlled by two linear motion stages. An Nd-Yttrium aluminum garnet (YAG) laser was used to generate a laser beam. Using this setup, the laser-power density and the beam size can be easily adjusted by fine-tuning the laser-beam path, the orientation of the half-wave plate, and the distance between the focus lens and the surface of the work-piece.

5.2.3 Compression experiments

Compression experiments were conducted at a strain rate of 2×10^{-4}/s, using a Material Test System (MTS) servohydraulic-testing machine controlled by a computer. The results for the as-cast and laser-peened samples were compared to study the influence of the LSP process on compressive behavior of BMG samples. For compression experiments, one group of Vit-105 samples was treated using a lower laser power density of 7.0 GW/cm^2, while another group was treated at 9.0 GW/cm^2, as

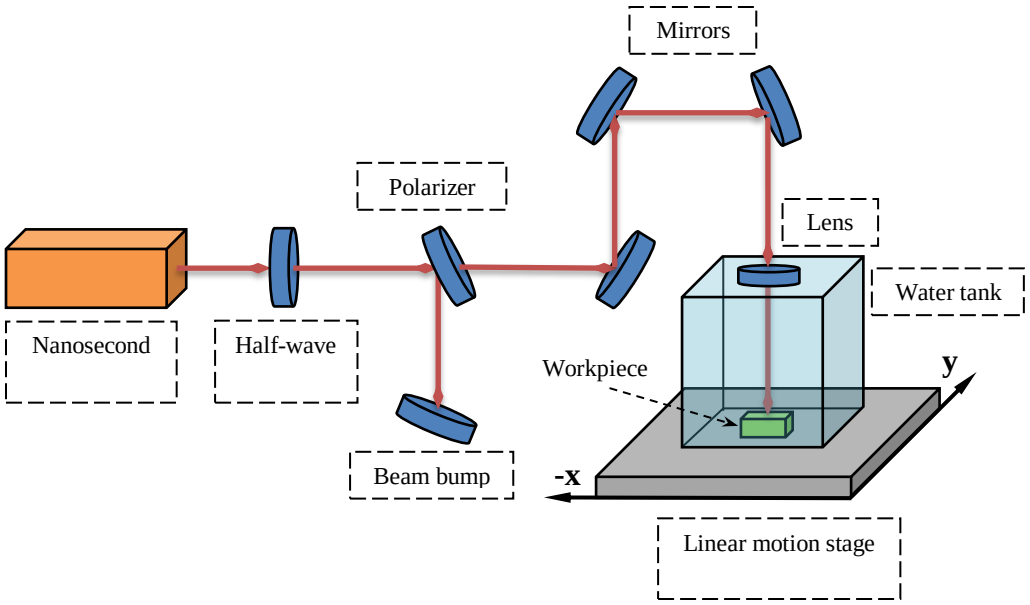

Figure 23. Experimental setup for laser shock peening (LSP)

described later. For each sample, the four lateral sides (4 mm $\times$ 2 mm) were treated with the same power density.

5.2.4 Four-point bending fatigue

Four-point bending fatigue experiments were conducted in a computer-controlled Material Test System (MTS) servohydraulic testing machine at different stress ranges and with a fixed R ratio, where $R = \sigma_{\min} / \sigma_{\max} = 0.1$, and $\sigma_{\min}$ and $\sigma_{\max}$ are the applied minimum and maximum stresses, respectively. In our experiment, three stress ranges, 550, 600, and 700 MPa, were chosen, while the nominal stress is calculated from the relation with applied force on each pin:

$$\sigma_{nom} = \frac{3P(L-t)}{2Wh^2} \tag{5}$$

where P is the total applied load, L and t are the distances between two outer pins and two inner pins, and W and h are the width and height of the rectangle samples, respectively.

5.2.5 Nanoindentation

Nanoindentation on the laser-treated samples is performed with a Micro Materials NanoTest using a Berkovich-type three-sided pyramidal diamond indenter. This system is a pendulum-based depth-sensing system, with the sample mounted vertically and the load

applied electromagnetically (Figure 7). The test probe displacement is measured with a parallel plate capacitor achieving the subnanometer resolution (details in [112, 113]).

At the lateral surface as to the laser-treated side, a 5×10 matrix was used to map the hardness affected by laser peening. For each indent, a load control mode was used with a loading rate of 0.05 *mN*/s and a max load of 10 *mN*. Between loading and unloading processes, a 5 s holding period was set at peak load for creep testing. To properly capture the pop-ins, thermal drift was kept below 0.05 nm/s.

5.2.6 Residual stress mapping using micro slot cutting method

(Cooperated with Dr. Bartlomiej Winiarski and Prof. Philip J. Withers)

To map the stresses, a series of micro-slots of $15 \times 2 \times 0.4$ μm^3 in size were made on the specimen surface (Figure 24a & b) using the FIB of a dual-beam Field Emission Gun Scanning Electron Microscope / Focused Ion Beam (FEGSEM/FIB) instrument [143]. In order to measure the displacement field caused by each microslot, a pattern of nano Pt dots was applied locally by the FIB-assisted deposition (Figure 24c) [144]. The deformation fields in the vicinity of slots were, then, reconstructed by the digital image correlation (DIC) of FEGSEM photos recorded during milling (Figure 24d). Since each slot has a wedge shape and a finite length, the residual stresses are inferred by fitting a reference displacement field obtained from the finite-element model (FEM) with the recorded displacement field [143]. In this way, residual-stress distributions have been characterized as a function of the distance from the laser-peened surface to a depth of 1,200 μm with a spatial resolution of 30 μm (arising from the spacing between the slots

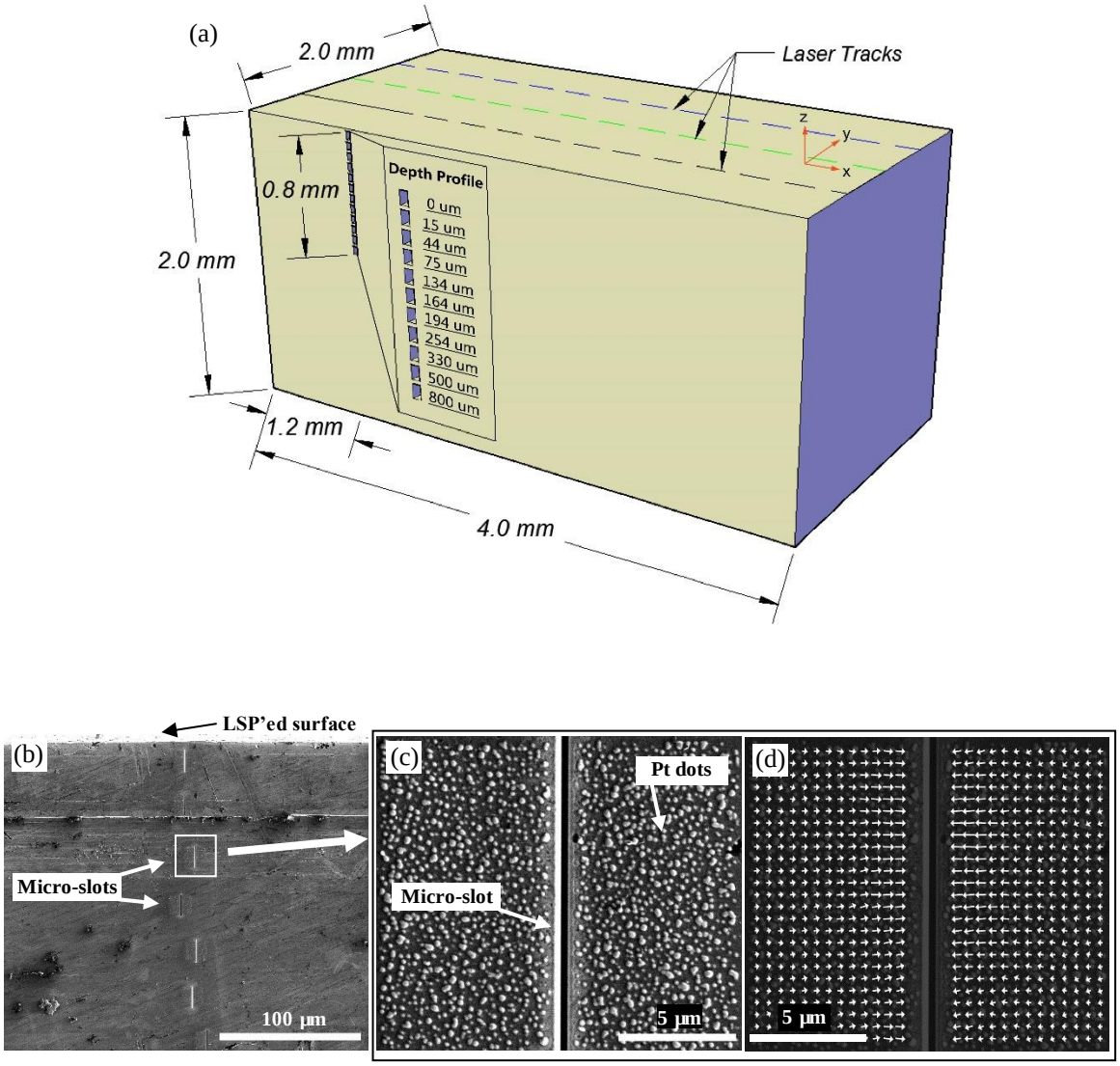

Figure 24. The micro-slot cutting method. (a) Schematic of residual-stress measurements on the side of the sample laser shock peened on the top surface, (b) Scanning electron microscopy (SEM) image showing a series of micro-slots introduced into the side of the specimen, (c) SEM image showing the random Pt-dot pattern deposited in the vicinity of a 0.4 m-wide micro-slot, and (d) a displacement field (indicated by arrows proportional to the deformation) inferred by the digital image correlation (DIC) analysis.

see Figure 24c). Residual stresses were measured in this way for the as-cast BMG, after mechanical polishing and after laser peening.

5.2.7 Synchrotron x-ray diffraction

High-energy synchrotron X-ray diffraction was performed at the Advanced Photon Source (APS) of the Argonne National Laboratory. The specimens with one surface treated by 9 GW/cm^2 laser were used in this study. The geometry of the samples is 6 mm $\times$ 3 mm $\times$ 3 mm. As described in Figure 25a, eight points from the laser-treated surface to the bulk center, i.e., at 0.2 mm, 0.3 mm, 0.4 mm, 0.5 mm, 0.6 mm, 0.8 mm, 1.0 mm, and 1.5 mm from the surface, were selected as the incident locations. The energy of the beam is 115 keV, and the beam size is 0.1 mm (direction *z* in Figure 25a) $\times$ 0.3 mm. The powder diffraction data was processed by software Fit2D, and the pair distribution function (PDF), *G(r)*, was obtained by software PDFgetX2 [145], which can be calculated from the Fourier transform of $Q[S(Q)-1]$ [146]:

$$G(r) = \frac{2}{\pi}\int_{Q=0}^{Q=\max} Q[S(Q)-1]\sin(Qr)dQ \tag{6}$$

where Q is the magnitude of the wave vector, $Q = 4\pi\sin\theta/\lambda$, and the structural factor, *S(Q)* is the coherent part of the total diffracted intensity of the material,

$$S(Q) = 1 + \frac{I_{coh}(Q) - \left[\sum_{i=1}^{n} c_i f_i^2(Q)\right]}{\left[\sum_{i=1}^{n} c_i f_i^2(Q)\right]^2} \tag{7}$$

In which, c_i and $f_i(Q)$ are the atomic concentration and the scattering factor of the atomic species of type i respectively [147].

5.2.8 Confined Plasma Model

(Cooperated with Dr. Yunfeng Cao and Prof. Yung C. Shin)

For nanosecond pulses with irradiances of several GW/cm^2, the plasma induced by the laser ablation of metal targets can be described by hydrodynamic equations for the whole physical domain, where the condensed phase contributes a mass to the plasma region mainly through hydrodynamic expansion. The one-dimensional (1-D) hydrodynamics model developed earlier by Wu and Shin [148] can be used to calculate the plasma pressure generated during LSP in a water-confinement regime. In their model, the plasma expansion was treated as the 1-D phenomenon, because the two-dimensional (2-D) effects are important only when the laser beam diameter is very small. Wu and Shin [149] further demonstrated that the 1-D assumption is valid, when the laser-beam diameter is equal to or larger than 300 μm. Since the laser-beam diameter used in this work is around 1.25 mm, it is sufficient to use this 1-D model in the present work to describe the confined plasma behavior under water.

A schematic diagram of the model for the interaction of laser radiation with a target surface in the confining medium (water) is shown in Figure 26. Initially, the metal surface is located at $z = 0$, the workpiece is at $z < 0$, and the water is in the $z > 0$ region. The sample is irradiated normally to the surface from the z direction. For this system, the

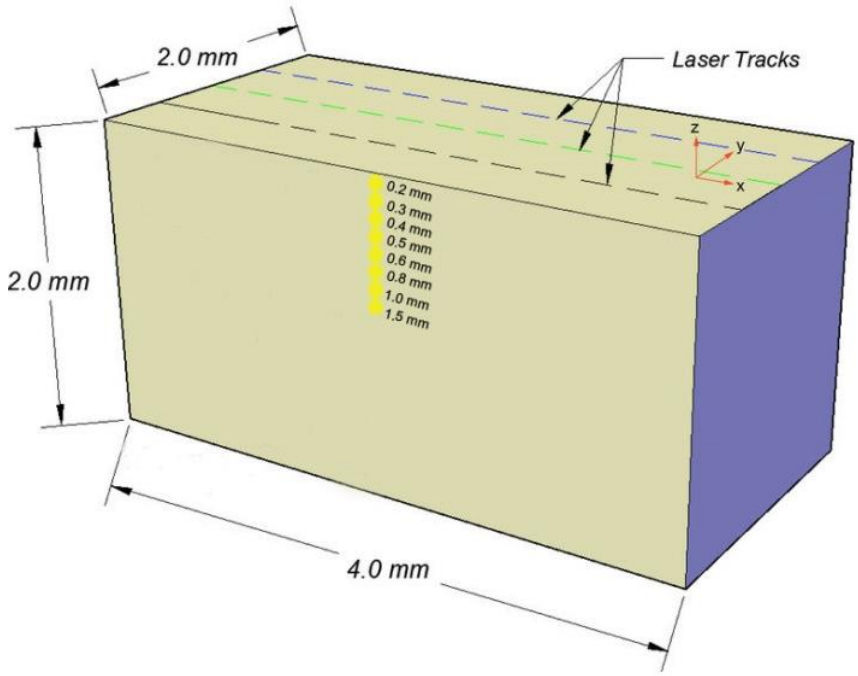

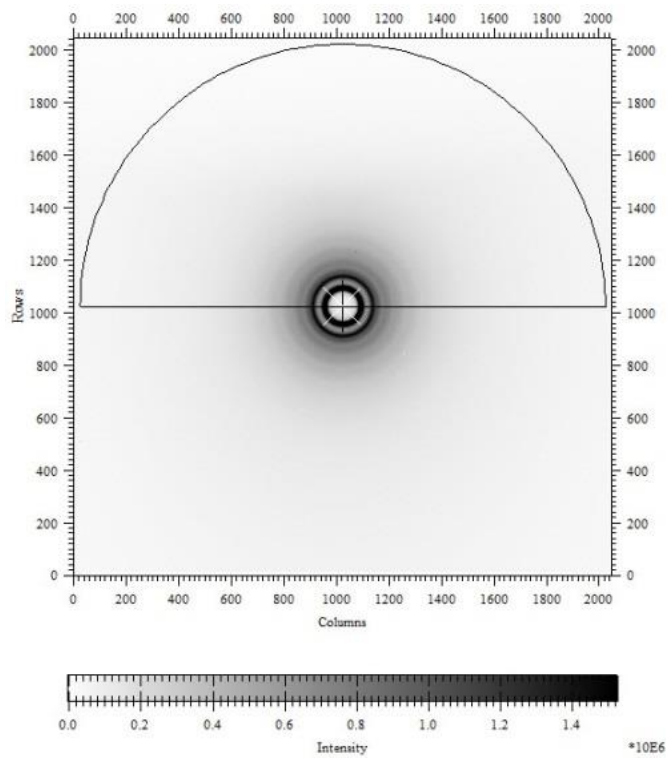

Figure 25. (a) Sketch of the specimen (Vit-105) used in the synchrotron diffraction, and (b) The diffraction pattern of Vit-105

1-D hydrodynamic equations, governing the conservation of mass, momentum, and energy, can be expressed as [148]

$$\frac{\partial}{\partial t}\begin{bmatrix} \rho_1 \\ \rho_2 \\ \rho u \\ E+\frac{1}{2}\rho u^2 \end{bmatrix} + \frac{\partial}{\partial z}\begin{bmatrix} \rho_1 u \\ \rho_2 u \\ \rho u^2 + P \\ u\left(E+\frac{1}{2}\rho u^2 + P\right) \end{bmatrix} = \frac{\partial}{\partial z}\begin{bmatrix} 0 \\ 0 \\ 0 \\ -q + k\frac{\partial T}{\partial z} + I \end{bmatrix} \tag{8}$$

where ρ_1 and ρ_2 are the densities of the metal and air (or water), respectively. ρ is the total density defined as $\rho = \rho_1 + \rho_2$. u is the velocity, P the pressure, E the volumetric internal energy, T the temperature, k the thermal conductivity, I the net flux in laser radiation in the z direction, and q the radiative heat flux in the z direction. To obtain the radiative heat flux, the radiative transfer equation needs to be solved in the diffusion approximation[S9]:

$$\begin{aligned} q &= \int_{\omega} q_{\omega} d\omega, \qquad \frac{\partial q_{\omega}}{\partial z} + ck_{\omega} ED_{\omega} = ck_{\omega} ED_{b\omega} \\ q_{\omega} &= -\frac{c}{3k_{\omega}}\frac{\partial ED_{\omega}}{\partial z}, \quad ED_{b\omega} = \frac{8\pi h\omega^3}{c^3\left(e^{h\omega/kT}-1\right)} \end{aligned} \tag{9}$$

in which c is the speed of light, ED_{ω} and $ED_{b\omega}$ are the spectral energy densities of the plasma radiation and blackbody radiation, respectively. k_{ω} is the absorption coefficient, and the index, 'ω', denotes the frequency-dependent quantity.

To solve the hydrodynamic equations, appropriate equations of state (EOS) must be employed. For the metal targets, the quotidian equation of state (QEOS) [150] is applied, which is an EOS model for the hydrodynamic simulation of high-pressure

phenomena. For water, the EOS developed by Ree [151] is applied, which covers the density range between 2 g/m^3 and 400 Mg/m^3 and the temperature range between room temperature and 25 keV (2.9 $\times 10^8$ K) by combining theoretical codes and experimental data. Several complex phenomena are considered, such as the ionization process and the chemical equilibrium among dissociation products of water [151].

Figure 26 shows the plasma pressure predicted by this model for the laser beam of a 6-ns full width at half maximum (FWHM) with a 100-μm aluminum tape on the Zr-based BMG substrate. The laser-power density used in this example is 8.64 GW/cm^2. The pulse duration for the pressure wave is approximately twice the laser pulse duration due to the confinement effect of the water layer, which has been observed by several researchers [148, 149, 152, 153].

5.2.9 Residual-Stress Calculation Procedures

(Cooperated with Dr. Yunfeng Cao and Prof. Yung C. Shin)

Figure 27 describes the procedure of the FEM calculation. The load is modeled as a distributed pressure in ABAQUS [154, 155], and its distribution is controlled by a user subroutine, VDLOAD [156]. The bottom surface of the sample (the xy plane, Figures 1a and S1) is considered to be rigid.

The structural coupling between the coating-layer shock-wave pressures and the substrate structural displacements at their common surfaces (the interfaces) is accomplished with the tie constraint option in ABAQUS [153, 154]. With this constraint

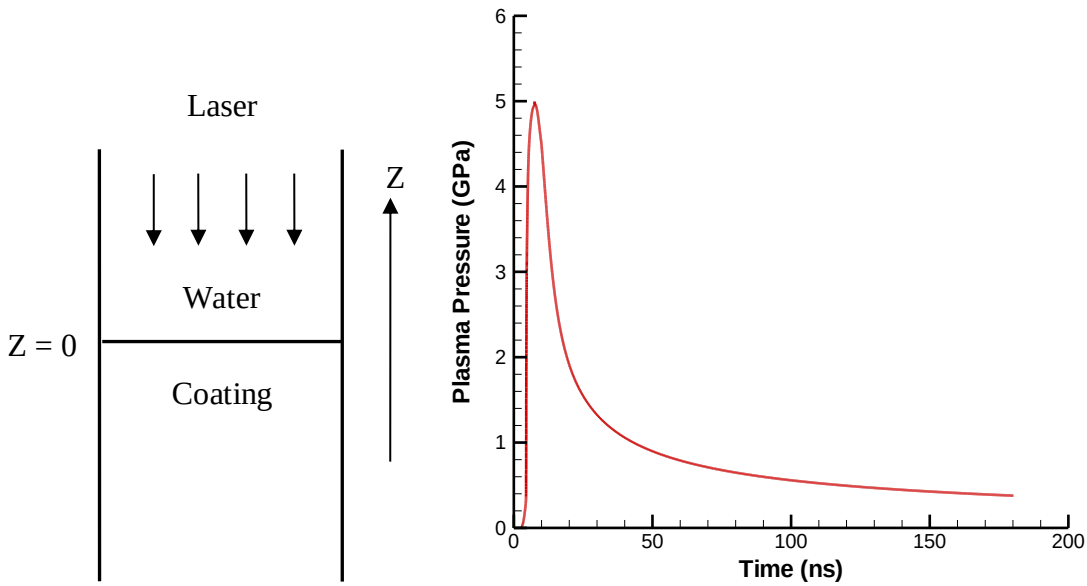

(a) (b)

Figure 26. (a) Schematic diagram of the 1-D model setup, (b) plasma-pressure history for laser shock peening of a BMG sample (Laser power density: 8.64 GW/cm^2, laser wavelength: 1,064 nm, full width at half maximum (FWHM): 6 ns, coating: 100-µm Al tape, and substrate: Vit-105)

in the loading direction, the continuity of displacements of nodes in the interface region between the coating layer (the slave surface) and the substrate (the master surface) is ensured.

The parameters used in the calculation are listed as follows. The Young's modulus is 82 GPa, Poisson's ratio is 0.36, shear modulus is 35 GPa, the density is 6,810 kg/m^3, and yield stress is 1.7 GPa [138-142].

5.3 Results

5.3.1 Morphology of sample surface after laser shock peening (LSP)

The BMG sample was shock peened using a laser wavelength of 1,064 nm and a pulse duration of 6 ns with the power densities of 7 and 9 GW/cm^2. The laser-beam diameter was set to about 1.25 mm, and the overlap ratio was selected to be 50%. Three consecutive tracks of peening were applied to the surface with a distance of 0.625 mm between track centerlines.

Figure 28 reveals changes of the surface morphology introduced by laser peening using optical microscopy. To maximize the laser-peening effect, we applied a relatively-higher laser power (10 GW/cm^2). Compared to the smooth surface before the laser treatment, the peening introduced a certain extent of surface damage in the form of linear shear cracks/bands (Figure 28), which is the direct result of the plastic deformation in the surface region. The presence of plastic deformation is due to the formation of localized shear bands. Concerning the observed change in plasticity (Figure 29), the formation of

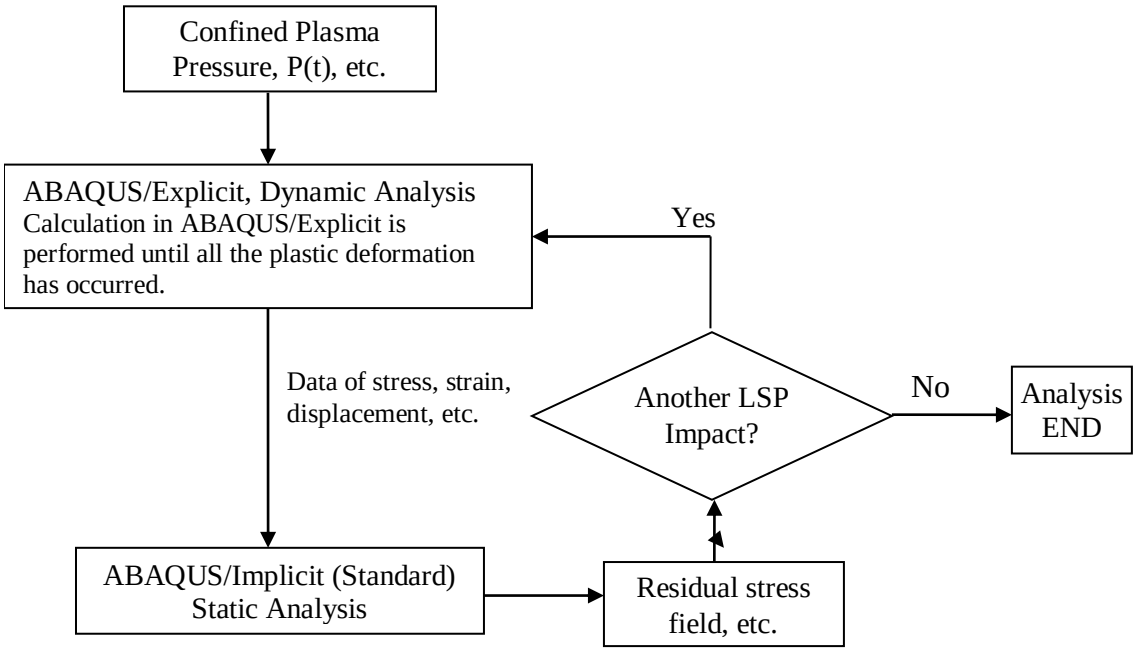

Figure 27. Finite-element modeling calculation procedures of residual stresses

the localized shear bands is the fundamental contributing factor affecting plasticity. And the surface-roughening behavior might contribute to the change in some other mechanical properties, for example, the ultimate tensile strength. This surface-roughening phenomenon is similar to the observation of the surface of the BMG subjected to the high-speed impact [157].

5.3.2 Stress-strain curves

Compression experiments were conducted to determine any improvement in plasticity introduced by LSP. Figure 29a shows the stress-strain curves of laser-peened Vit-105 [$Zr_{52.5}Cu_{17.9}Ni_{14.6}Al_{10}Ti_5$, atomic percent (at. %)] BMG samples under different laser power densities. The solid (black) line describes the stress-strain behavior of the as-cast sample, which shows very little plasticity (0.137%). The dash-dotted (red) and dashed (blue) lines depict the laser-treated samples, with the plastic strain improved to 0.505% for 7 GW/cm^2 and 0.744% for 9 GW/cm^2, respectively. Note that the fracture strain, ε_f, here equals the elastic strain, ε_e, plus the plastic strain, ε_p (i.e. $\varepsilon_f = \varepsilon_e + \varepsilon_p$,). The serrations were observed for the stress-strain curves during the plastic deformation stage (shown inset in Figure 29a). Interestingly, the fracture strength of 1,745 MPa for the as-received condition increases to 1,869 MPa and 1,834 MPa for 7 GW/cm^2 and 9 GW/cm^2, respectively. The inset describes the serration part of the stress-strain curves at a magnified scale.

Figure 29b describes the stress-strain curve of the laser-treated $Zr_{50}Cu_{40}Al_{10}$ BMG. As indicated by the curves, a laser power of 5 GW/cm^2 fails to improve the plasticity,

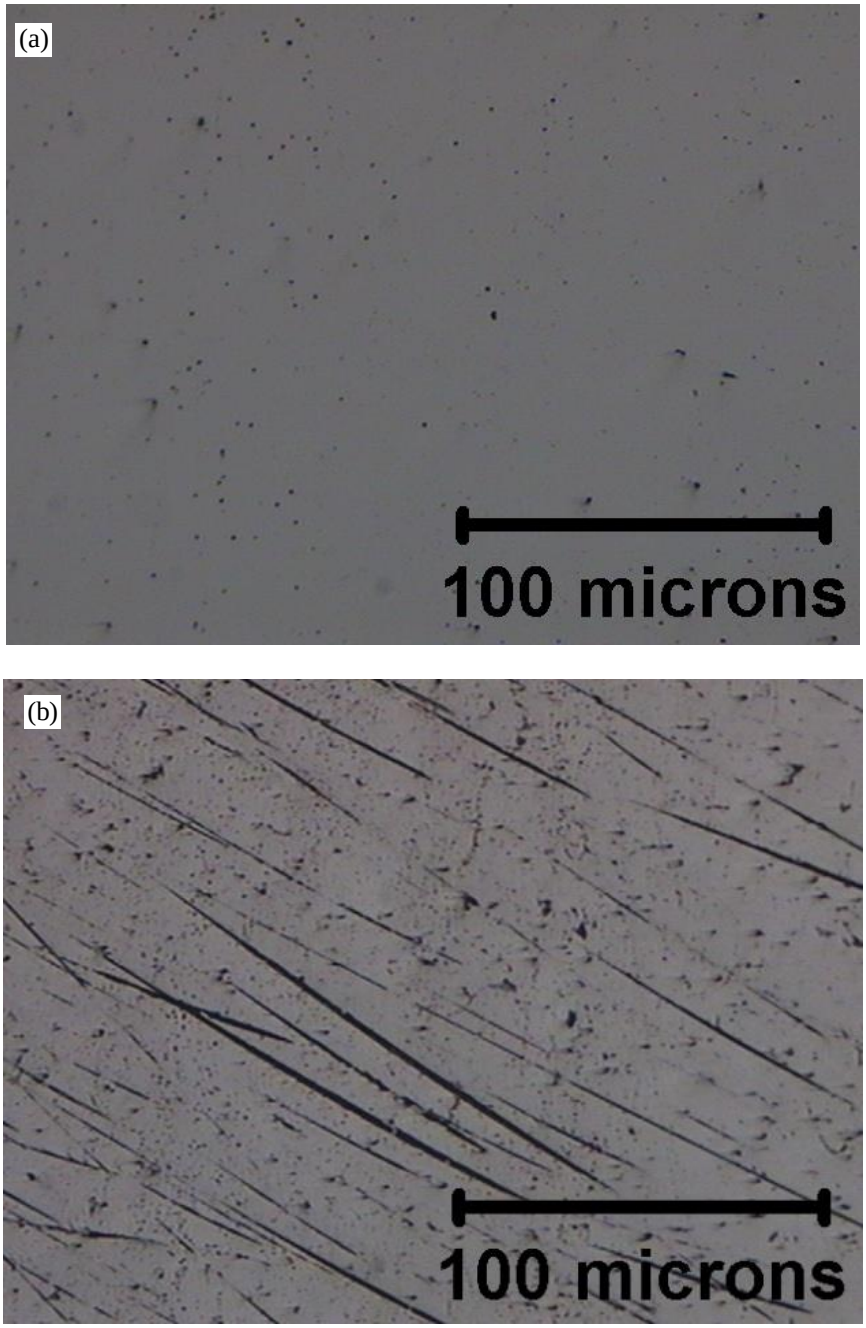

Figure 28. Surface morphology of bulk metallic glass (BMG) samples (a) before LSP and (b) after LSP using a power density of 10.0 GW/cm^2

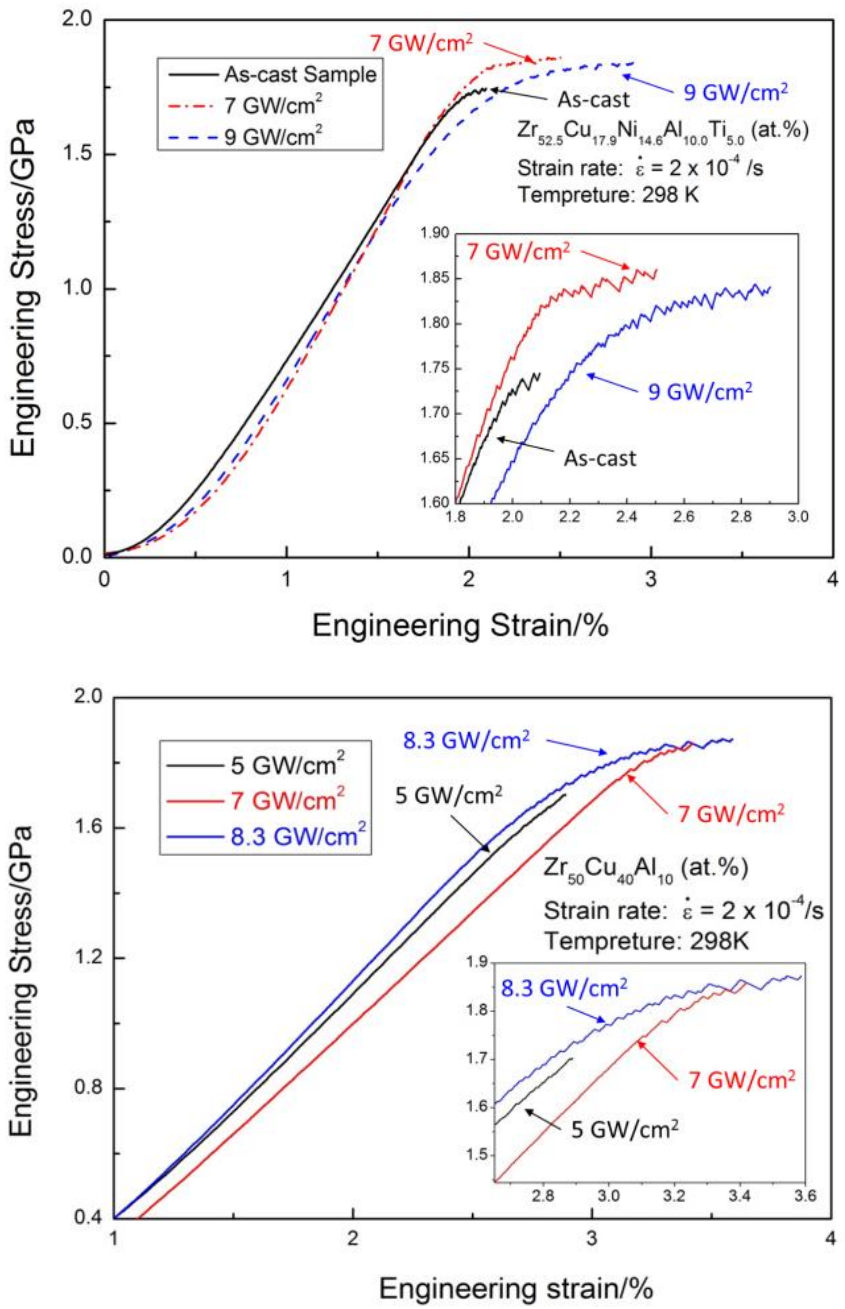

Figure 29. Compression results of laser-treated BMGs (a) $Zr_{52.5}Cu_{17.9}Ni_{14.6}Al_{10}Ti_5$, and (b) $Zr_{50}Cu_{40}Al_{10}$ by different laser power levels.

while 7 GW/cm^2 extends the plastic strain to 0.1% and 8.3 GW/cm^2 to 0.7%, respectively. The serrations appear, as the plastic deformation proceeds.

5.3.3 Results of fatigue resistance

Figure 30 shows the fatigue test results on three $Zr_{50}Cu_{40}Al_{10}$ samples, compared with the surface severe plastic deformation (S^2PD) process in Tian et al.'s work [158]. In their work, one side of the rod was repeatedly bombarded by 20 WC/Co balls with a diameter of 1.6 mm using a Spex 8000 miller in a back-and-forth mode at a frequency of 60 Hz in an argon atmosphere. The black dots denote the samples treated by LSP. In the low-cycle-fatigue area (e.g., the fatigue life lower than 10^5 cycles), the fatigue behaviors of black dots are similar to S^2PD-processed and as-cast ones, but some difference between two techniques was observed in terms of fatigue lifetimes. At the stress ranges of 700 and 550 MPa, the fatigue lifetimes of laser-peened samples are slightly lower than those of S^2PD-processed and as-cast ones, which implies that the laser-peening causes negative effects on fatigue properties to some extent. However, at a stress range of 600 MPa, fatigue life was extended. If we summarize the laser effects along with the S^2PD effects, the changes of fatigue life present a "curvy" shape, i.e., the fatigue resistance is only improved at specific stress ranges (intermediate range here), and will be depressed at higher and lower ranges. Previous work [159] indicates that bombardment may cause surface contaminations and damages in the sample surface layer, which may shorten the fatigue lifetime. For BMGs, the laser peening may introduce some shear bands into the surface layer, which could serve as the origin sites of crack during fatigue process.

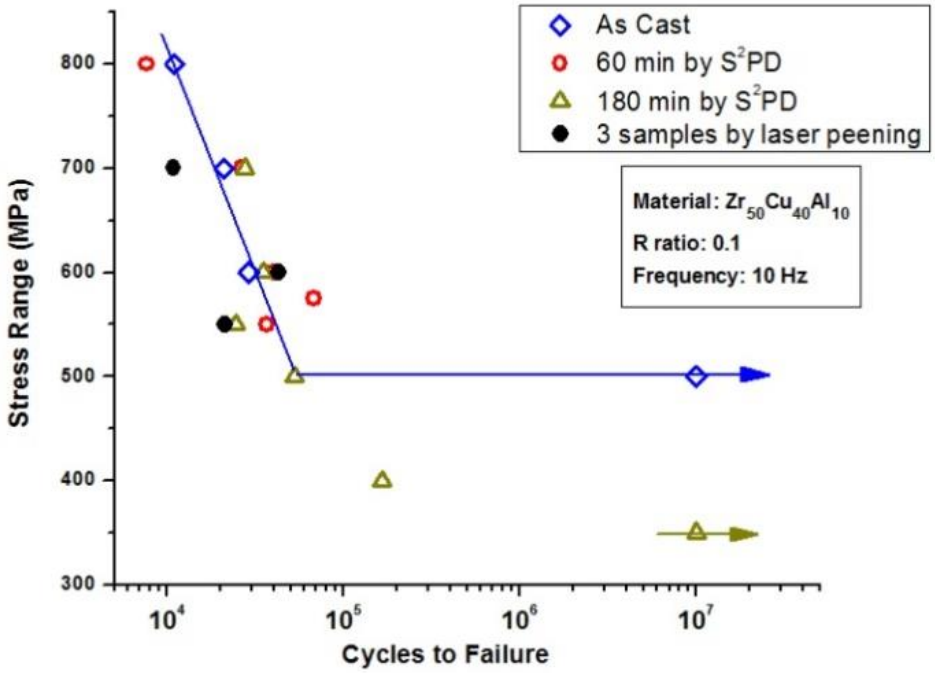

Figure 30. Four-point bending fatigue-test results on the laser-treated samples and the samples treated by surface-severe-plastic-deformation (S^2PD) process [158]

5.3.4 Morphology of fractured surfaces of laser-peened samples

The fracture surfaces after compression were investigated using scanning electron microscopy (SEM). For as-cast Vit-105 samples, the single primary shear band along the fracture surface dominates the failure. For the laser-treated samples, as shown in Figure 31a, we found the secondary shear bands at the lateral surface of the fractured laser-treated sample. It's reported that the simultaneous nucleation of shear bands is responsible for the good plasticity of BMGs [160]. In Figure 31b, multiple shear bands interact with each other, and as a result, the plastic deformation is extended [161, 162], since the interaction of shear bands creates steps on each other and restricts shear-band rapid propagation [163], which confirms the effect of introduced residual stresses.

Figure 32 describes the typical vein-like pattern on the fracture surface, and the direction of shear-band propagation is denoted by the arrow. The vein-like pattern corresponds to the separation of the surfaces along the interface where the viscous flow may take place. A very low viscosity, and, therefore, a very short duration of slip is required for the surface-tension driven flow to produce the smooth surface within the pattern lines [164]. The anisotropic pattern indicates the sample fractured under the normal separation of surfaces and the tangential discontinued displacements. The former will lead to the void (cavity) formation, and the latter to the hardening behavior.

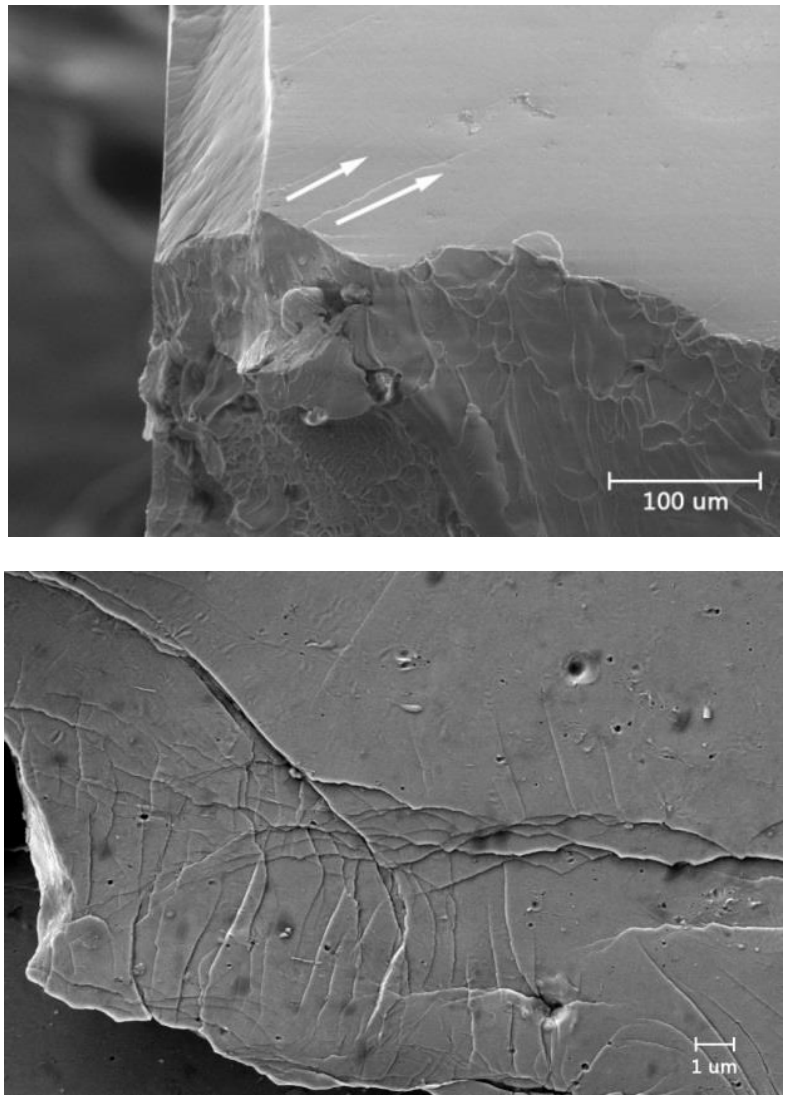

Figure 31. Morphology of the compressive fracture surfaces of the laser-treated Vit-105 by SEM. (a) secondary shear-band propagation on the lateral surface, and (b) Magnified region with the existence of multiple shear-band interactions.

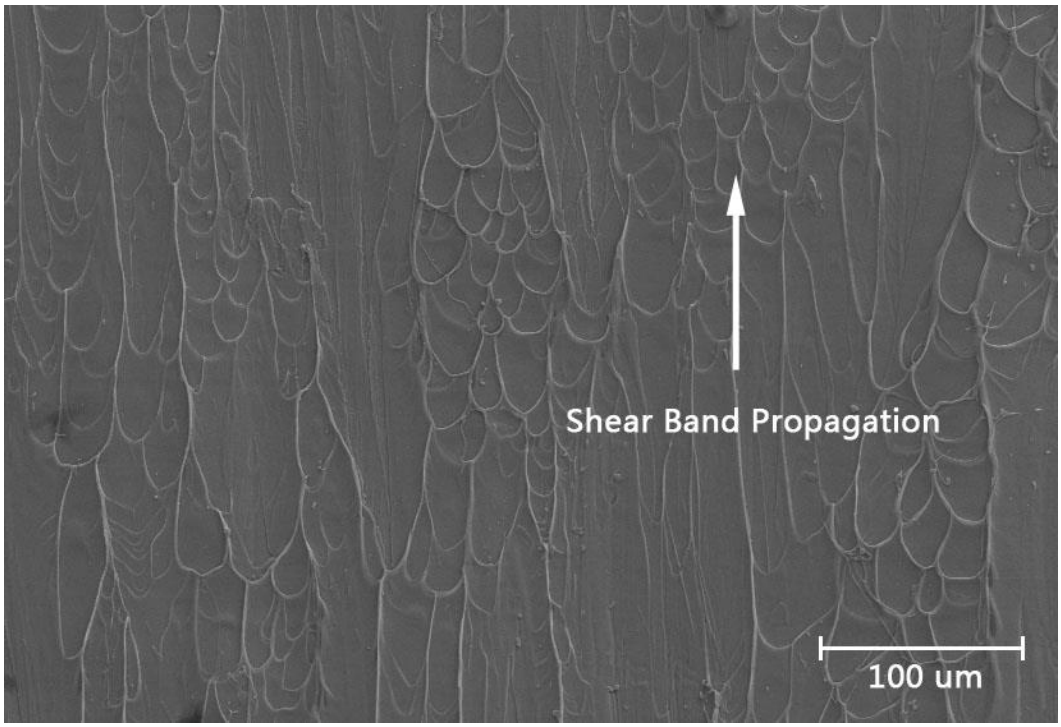

Figure 32. The vein-like patterns formed along the shear direction at the fracture surface

5.3.5 Load-depth curve and hardness

Recent work [131] reported that shot peening could affect the hardness in the peened layer. Same as the advanced surface processing technique, we performed nanoindentation experiments to characterize the laser effect on the hardness at the local region of BMGs.

The hardness is defined as the ratio of the maximum load, P_{max}, and contact area [165, 166]. Thus it is expressed as

$$H = \frac{P_{max}}{Mh^2} \tag{10}$$

where M is the geometrical constant depending on the shape of an indenter and h is the indentation depth.

The load-depth curves at different location from the laser-treated surface are shown in Figure 33a. Pop-ins can be found in every curves. Since load control is used, the pop-ins indicates the local plastic deformation and behaves as plastic serrated flow, which is similar to the stick-slip behavior in the compression.

Using Eq. (10), the hardness mapping is described in Figure 34. Obviously the laser-treated layer can be identified by the magnitude of hardness. To a depth of ~ 45 μm, the hardness is reduced by almost 20%, from 8 GPa to 6.5 GPa, averagely. Meanwhile, the nanoindentation also depicts the local heterogeneity of BMGs.

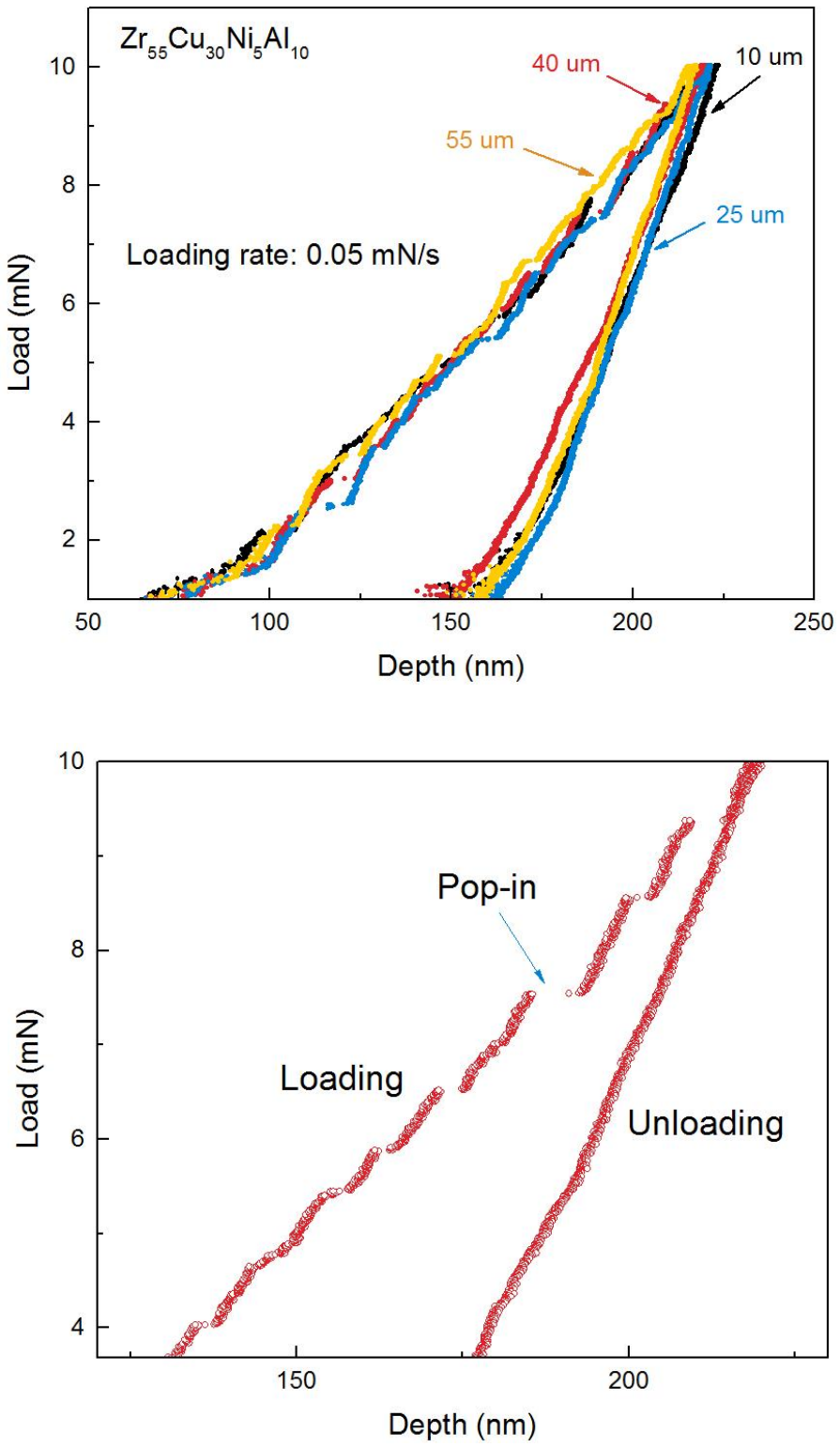

Figure 33. Load-depth curves for (a) different locations from the laser-treated surface, and (b) amplified region indicating the pop-ins.

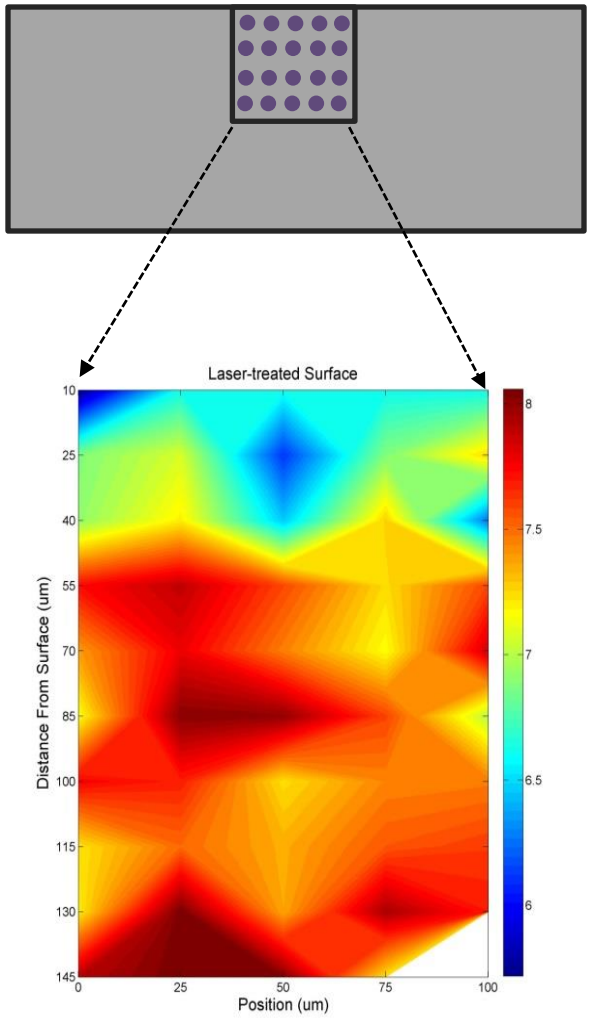

Figure 34. Hardness (GPa) mapping on the lateral surface by 5 × 10 points using Nanoindentation, (a) schematic of the mapping region, and (b) results of the amplified mapping region

5.3.6 Residual stress mapping on the laser-treated sample

(Cooperated with Dr. Bartlomiej Winiarski and Prof. Philip J. Withers)

The measurements were taken at the slot locations shown in Figure 24a as a function of distance from the peened surface. The slots were oriented so as to measure the residual stresses along the longitudinal direction (the x direction) of the sample.

The slots were milled in a single increment to give the stress averaged over the removed slot depth (~ 2 microns). For an infinitely long, narrow slot, the surface displacements away from the slot, U_x, are given by the following equation (see Ref. S5 for details).

$$U_x = \frac{2.243}{E'}\sigma_x \int_0^a \cos\theta \left(1 + \frac{\sin^2\theta}{2(1-\nu)}\right) \times \left(1.12 + 0.18 \sec h(\tan\theta)\right) da \qquad (11)$$

where x is the distance from the slot, ν is the Poisson's ratio, $E' = E/(1-\nu^2)$, E is the Young's modulus, σ_x is the residual stress, a is the slot depth, and $\theta = \arctan(x/a)$.

The variation in the measured residual stress after laser peening as a function of depth are described in Figure 35 (the red solid line). The peak compressive stress (810 MPa) occurs at a depth of about 50 m. Note that the residual stress for a small sample size could be lowered due to the lack of constraint, when compared to a thicker sample. It is also noteworthy that the stress reaches a plateau of - 300 MPa at a depth of about 300 m. Measurements on the as-cast samples show that the fabrication process gives rise to a compressive residual stress of - 40 MPa near the surface, and that these stresses can rise to between - 110 and - 400 MPa after mechanically polishing. Consequently, it would

appear that the residual stresses measured on the polished sides of the sample at distances greater than 300 m from the peened surface are due to sample preparation.

5.3.7 Pair distribution function (PDF)

The PDF describes the atomic density distribution as a function of inter-atomic distances, and thus can reveal the useful local atomic pair information, such as the distances between central and neighboring atoms [167]. Using Fit2D, we obtained the diffraction pattern, which is shown in Figure 25b. To remove the influence of edge effect, that is, when the incident pulses of the synchrotron beam are at the edge of the specimen, we just process the upper half plane of the diffraction pattern, as indicated in Figure 25b.

Figure 36 present the experimentally obtained structure factor *S(Q)* and PDF *G(r)* calculated from Eq. (6). It's evident that no crystalline phase was found here, indicating that the laser peening didn't induce crystallization to the amorphous alloys. The first peak in the PDF reflects the structure information in the short-range order, which is extraordinarily important for the study of their mechanical properties. Figure 36c is the enlarged part of the nearest pairs in Figure 36b, and the curves are plotted as the depth from the laser-treated surface. As an effect of laser peening, significant changes can be observed in the peak profile. Interestingly, the first peak of *G(r)* decreases when the incident beam goes deep, indicating a compressive status for the atoms in the surface layer, compared to the curve at 1.5 mm, which is just at the center of the bulk. The curves from 0.2 mm to 0.6 mm match well, and exhibit an obvious separation from the other curves, suggesting an equal stress status among this area. Note that the resolution of the synchrotron beam is 0.1 mm along the depth direction. A smaller beam size may give

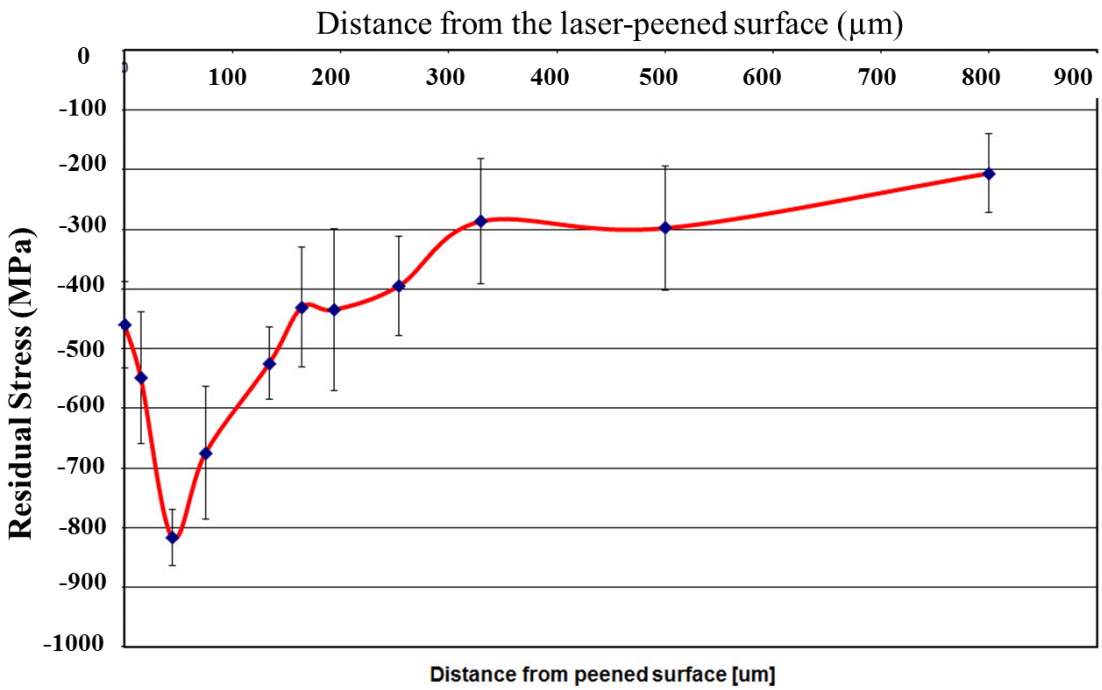

Figure 35. Residual stresses for the bulk metallic glass (BMG) sample (Vit-105) after LSP to a power density of 8.64 GW/cm

more detailed information about the stress distribution. The first peak shifts to the lower *r* as the depth decreases from 1.5 to 0.6 mm, showing the compressive stress is increasing from the bulk center to the surface.

5.3.8 Predicted residual stress from FEM

(Cooperated with Dr. Yunfeng Cao and Prof. Yung C. Shin)

In accordance with the conditions studied for the residual-stress measurement, a laser power density of 8.64 GW/cm^2 was considered in the modelling efforts. The residual stresses predicted by our FEM are shown in Figure 37a. The depth of the compressive residual stress zone after LSP is predicted to be around 300 μm, which is in good agreement with the effective depth of 300 μm measured experimentally. The predicted maximum residual stress of - 830 MPa along the center track is very close to the maximum value of - 820 MPa measured. Some differences can be observed for the residual stresses along different tracks due to the overlapping effect of the laser treatment.

It should be noted that the dynamic behavior of the coating and substrate material play an important role in the shock-wave propagation and development of residual stresses. In the LSP process, the typical strain rate can be as high as 10^7 s^{-1}. Thus, the dynamic yield strength of the coating material is significantly increased due to the strain-rate hardening effects introduced by LSP. Here we describe the dynamic behavior of the coating material by the Johnson-Cook model [168]:

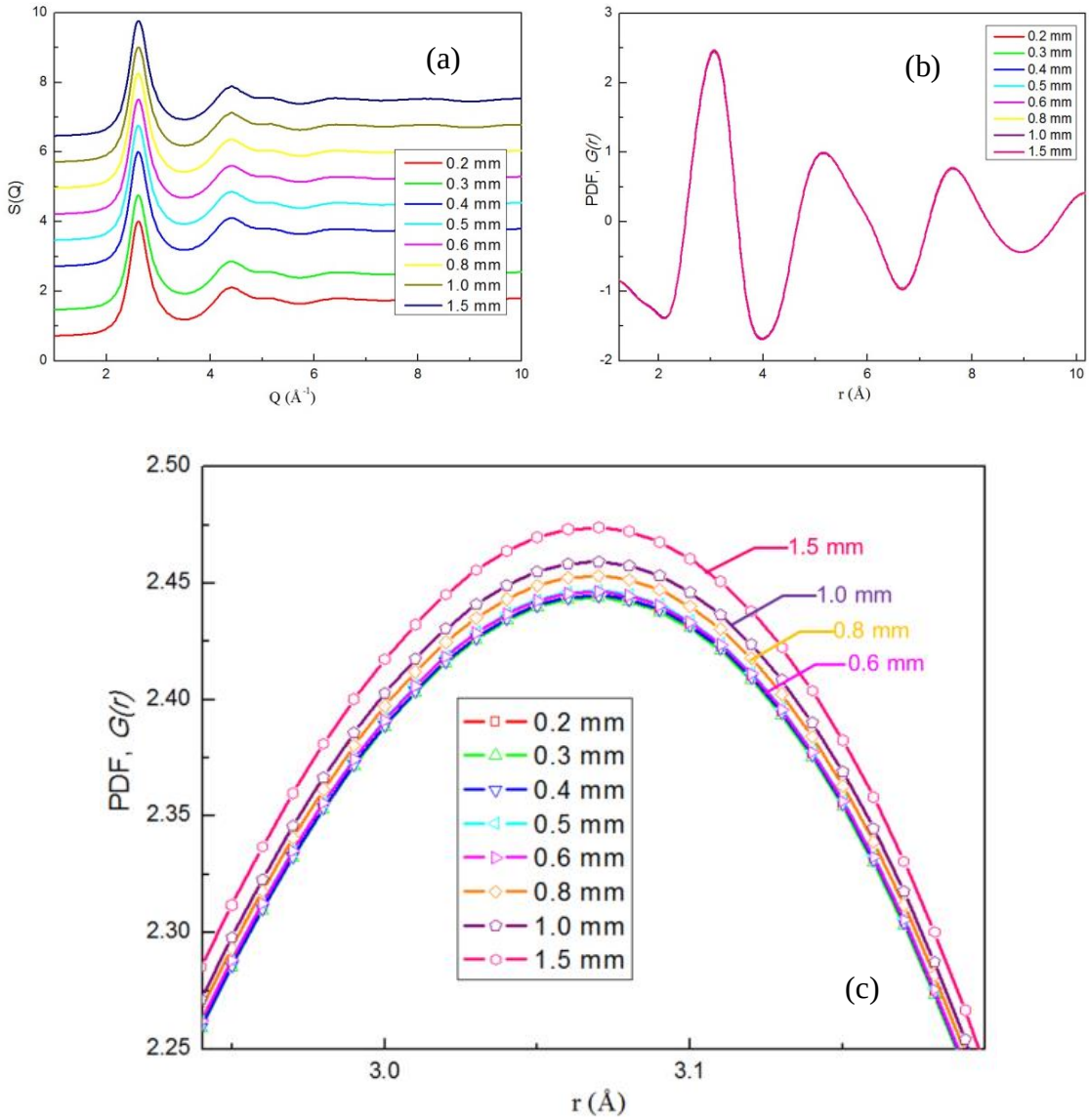

Figure 36. (a) Structure factors, *S(Q)*, (b) the PDF curves plotted as the depth profile from the laser-treated surface for Vit-105 BMGs, and (c) the enlarged area of the first peaks in (a).

$$\sigma = (A + B\varepsilon^n)\left[1 + C\ln(\frac{\dot{\varepsilon}}{\dot{\varepsilon}_0})\right] \text{ where } \dot{\varepsilon}_0 = 1\ s^{-1} \tag{12}$$

where σ is the flow stress, A = 120 MPa, B = 300 MPa, C = 0.1, and n = 0.35 are material constants for the aluminum coating [169], ε is the plastic strain, $\dot{\varepsilon}$ represents the strain rate, and $\dot{\varepsilon}_0$ is the effective plastic strain rate of the quasi-static test used to determine the above materials constants. Previous work [92] has shown that the peak yield stress varies slightly with the strain rate up to 1,000 s^{-1} at low temperatures (at least 295 K and 473 K) for the Zr-based Vit-1 BMG, which has a similar chemical composition to Vit-105. From the thermodynamic aspect, typically for LSP, the coating layer (e.g., Al) is ablated, preventing a significant increase in the temperature of the substrate, and hence thermal effects are neglected in our model. Thus, the substrate (e.g., Vit-105 BMG) can be modeled as an elastic-plastic material without a significant strain-rate effect.

In order to assess the effect of strain rate on yielding and, hence, the laser-peened residual-stress state, we estimate the stress-strain curve based on the results [170] up to a strain rate of ~ 5,000 /s, since there is no available data for the strain rate as high as to 10^7 /s. The residual stresses after LSP were recalculated, using this strain-rate-softening effect, and the results were presented in Figure 37b. The predicted depth of the compressive residual-stress zone after LSP is increased from around 300 to 450 μm (relative to the static case, Figure 37a) depending on the LSP track due to the strain-rate softening effect [170]. Apart from this feature, the predictions are similar to those for the static case, for example, in predicting a maximum stress of - 800 MPa between 50 and 100 m from the surface (Figure 37b).

When considering the predictions, it should be remembered that the constitutive model of the BMG material in the present work may not be sufficiently accurate because the high strain-rate experimental data are not available. The available experimental data run out at 5,000/s, which is far less than the maximum strain rates typically observed in LSP (~ 10^7/s). Therefore, the strain-rate softening behavior of BMGs under LSP may be underestimated. As indicated in Refs. [170-173], the temperature rise inside the shear band may introduce strain softening at high strain rates, which may further increase the depth of the compressive region after LSP. Above all, the present study provides novel methods to improve the plasticity and strength of BMGs through both experimental and theoretical modeling effects. The combined experimental and theoretical strategy of laser treatments can open up wide opportunities to process BMGs with desired properties for applications.

5.4 Discussion

5.4.1 Compression results

It is evident from Figure 29 that the plasticity and the fracture strength of both BMG samples are improved upon LSP. From the insets of Figure 29, the serrated flow regime of the laser-treated samples is about 3 ~ 7 times longer than that of the as-cast ones. Even though the mechanism of the stress-flow serration in metallic glass is still unclear, it is almost certainly connected to shear-band propagation [24, 174]. The present result suggests that near-surface shear bands introduced by laser peening along with the associated compressive residual stresses may impede the catastrophic propagation of

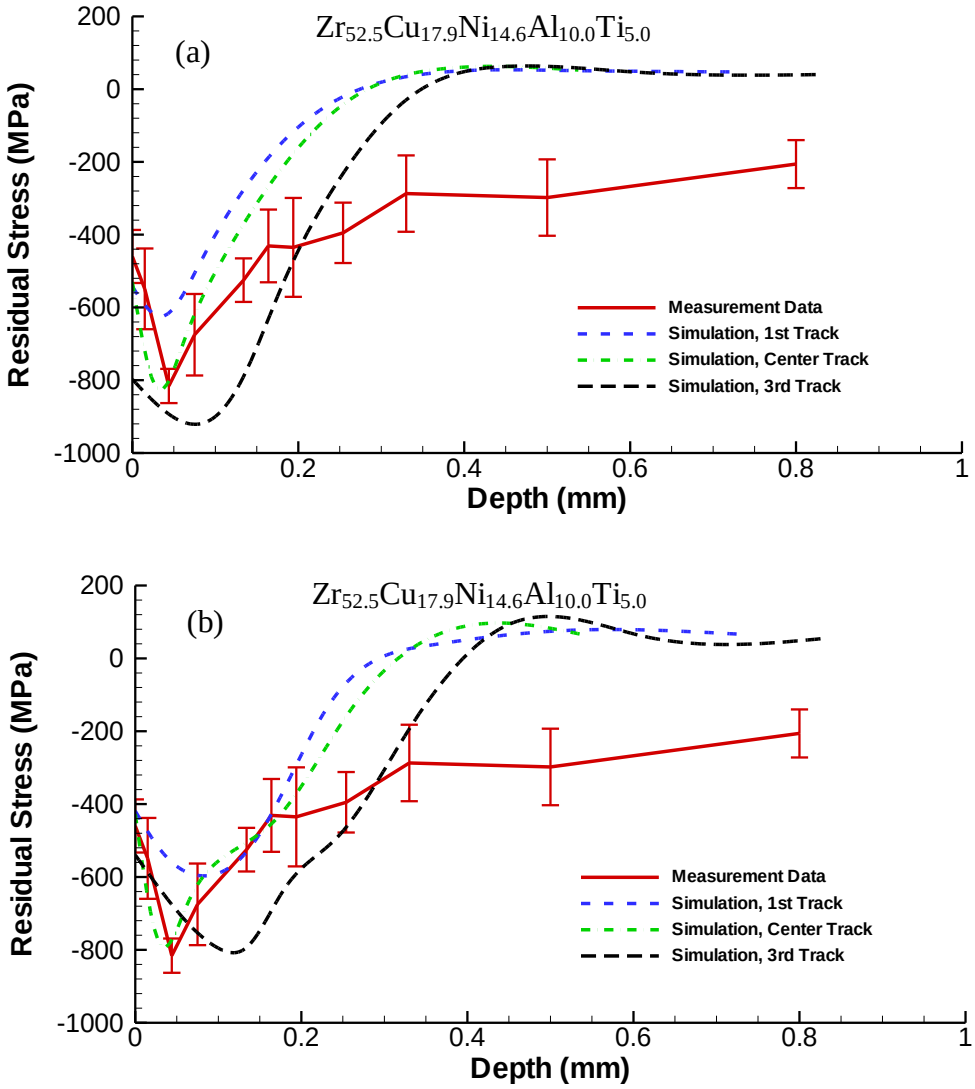

Figure 37. Residual stresses for the bulk metallic glass (BMG) sample (Vit-105) after LSP to a power density of 8.64 GW/cm, compared to model simulations, (a) assuming that there is no strain-rate effect, and (b) including strain-rate softening at high strain rates. The compressive plateau is taken to be the residual-stress state introduced by the surface preparation prior to micro-slotting. The colors of simulated tracks correspond to those in Figure 24a.

macro-shear bands, allowing a more distributed network of shear bands to develop, which is beneficial for the plastic deformation.

5.4.2 Serration behavior of laser-peened BMGs

To quantify the characteristic serration during the plastic deformation, we employed the statistics analysis of stress drop avalanches,

The compression experiments are under the strain-rate control, so a discrete avalanche event is characterized by a sudden drop in applied stress. By defining the first derivative of stress with respect to time to be the velocity of a stress drop, we could obtain the magnitude of stress drop avalanches. To remove small fluctuations caused by machine noise, a threshold is set, and a discrete avalanche is considered for each set of points in time where the velocity is consistently above the threshold, which is calculated:

$$v_{threshold} = v_{mean} + a\sigma \tag{13}$$

where v_{mean} is the mean velocity (displacement over time) of the sample, σ is the standard deviation of the velocities, and a is a constant greater than 0, which is tuned so that the $v_{\mathrm{threshold}}$ lies above all the characteristic noise.

Furthermore, we studied the serration regime in the stress-strain curve, and the complementary cumulative distribution function (CCDF) for stress drops, as described in Figure 38. Each stress drop represents a slip avalanche, and is caused by shear-band propagation. In terms of energy, shear-band propagation and arrest refer to periods of elastic energy release and accumulation, respectively. The serrations, or stress drops, in

the stress-strain curves are seen, wherever the stress suddenly drops from a higher to a lower value. The CCDF, *C(S)*, of the stress drop sizes *S*, gives the number of stress drops larger than or equal to a size *S*, *N(S)*, divided by the total number (N_{total}) of stress drops observed in the experiment (see Reference [30] for more details), which can be expressed as:

$$C(S) = N(S) / N_{total} \tag{14}$$

This definition implies that C(S) decays monotonically with C(S = 0) = 1 and C(S = S_{max}) = 1/N_{total}, where S_{max} is the largest stress drop observed in the experiment. It is clear from Figure 3b that the total number of slips (the reciprocal of the right end value in the CCDF curve, i.e., 670 for the as-cast case, 180 for 7 GW/cm^2, and 140 for 9 GW/cm^2) decreases for higher laser powers. Also in the as-cast brittle case, the range of slip sizes appears to extend down to smaller slip sizes than is observed for the laser-treated samples.

The CCDF plot of Figure 38 clearly depicts the shear-banding process and the different deformation mechanisms in the as-cast and laser-treated samples. For high laser-power treated samples (7 and 9 GW/cm^2 for Vit-105 and 8.3 GW/cm^2 for ZrCuAl), most of the avalanche located in the interval of large stress drop values (around 1 MPa), while for the as-cast sample and low-power treated samples, most slips has values at the order of 0.1 MPa. It is reasonable to expect that the laser-peening induced shear bands behave as pre-existing shear bands at the surface (Figure 28), and facilitate the initiation of further deformation at these locations in the compression tests. In other words, these shear bands accommodate the deformation and reduce the chance of shear-band initiation at other places. In contrast, for the as-cast samples, new shear bands will nucleate at more

places without the pre-existing shear bands. However, the primary shear band (along the fracture direction) will dominate during the deformation process, resulting in relatively short lifetimes for these new shear bands. Therefore, more small slips will be present for as-cast samples than that for the laser-treated samples. This trend agrees with the results shown in Figure 38, where clearly the as-cast samples have more small slips than the laser-treated samples. Meanwhile, the laser-induced compressive residual stresses impede shear-band propagation under the uniaxial loading and, thus, extend the elastic energy-accumulation period prior to 'plastic' deformation by slip. The combination of above factors contributes to the larger plasticity for laser-peened samples, again in agreement with Figure 38, which shows that the laser-treated samples have fewer slips that are on average larger than in the as-cast samples. This mechanism is, hence, confirmed by the results of Figure 38.

5.4.3 Assessment of strain-rate effects

(Cooperated with Dr. Yunfeng Cao and Prof. Yung C. Shin)

In order to assess the effect of strain rate on yielding and hence the laser peened residual stress state, a strain-rate-sensitive model was also applied. A dynamic compression test of the Zr-based bulk metallic glasses (BMG) Vit-1 was reported using the split Hopkinson pressure bar [170]. As introduced in Ref. [170], it can be seen that the dynamic yield stress is close to the quasi-static value of 1.9 GPa reported in Refs. [92, 170, 171, 175] for strain rates below 1,000/s. For strain rates greater than 3,000/s,

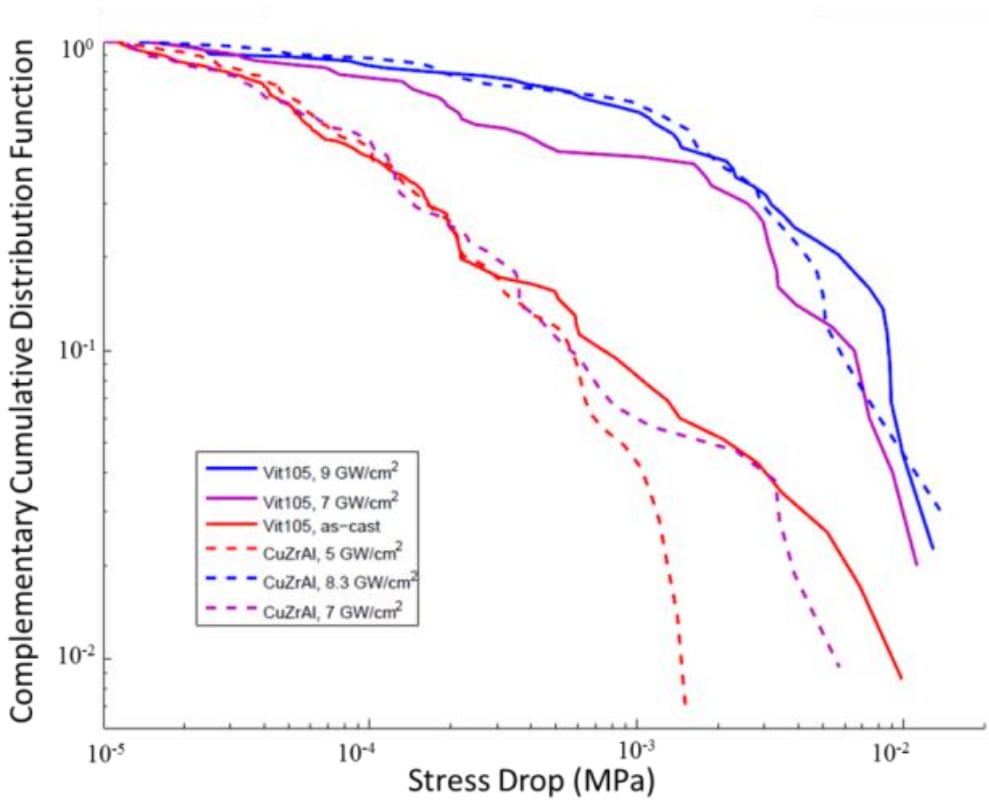

Figure 38. Log-log plot of the complementary cumulative distribution (CCDF) of stress-drop sizes during the serration regime in the stress-strain curve for Vit-105 (solid lines) and $Zr_{50}Cu_{40}Al_{10}$ (at. %, dashed lines)

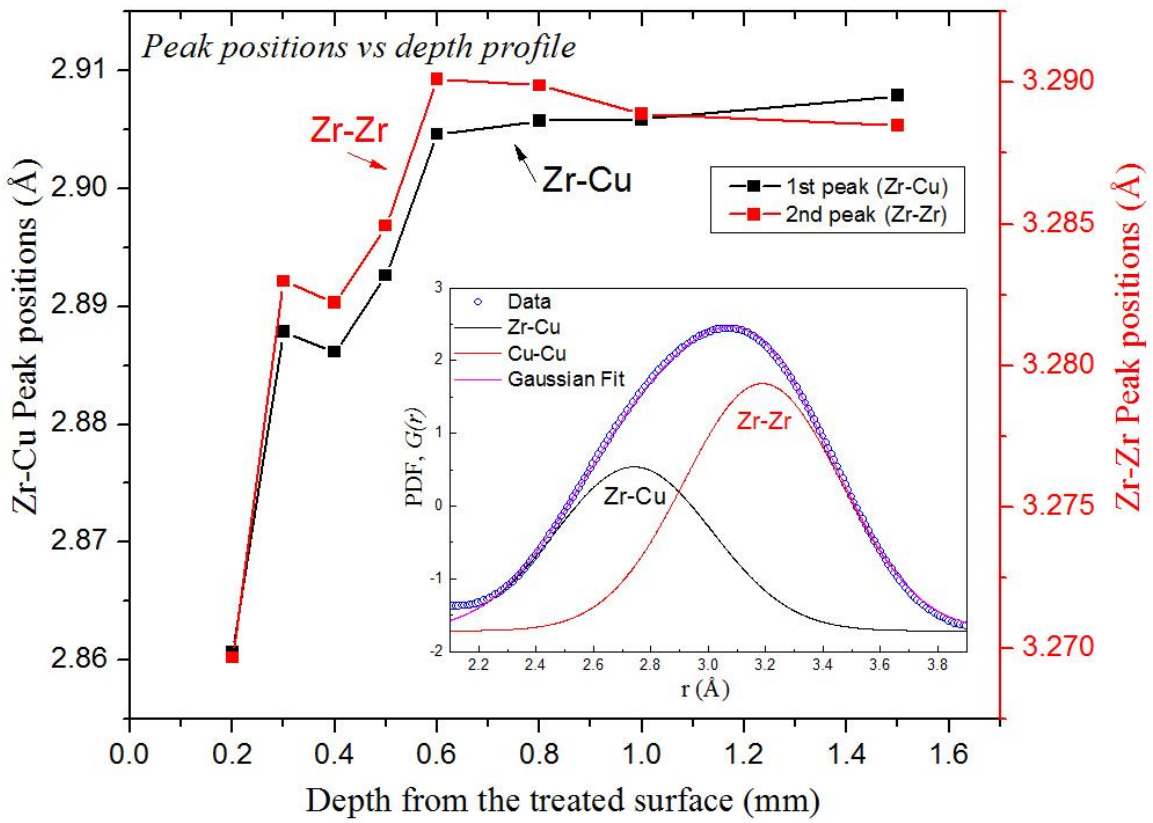

Figure 39. Fitted peak positions vs. depth profile using Gaussian fitting, the red solid line represents Zr-Zr pair, and the black solid line represents Zr-Cu pair, and inset shows an example of the fitting method

however, the compressive yield stress decreases monotonically with strain rate (strain-rate softening) [92]. Therefore, the strain-rate softening effect on dynamic yield strength can be obtained [170].

The stress-strain curve shown in Figure 29a is considered to be in a quasi-static or static-loading condition. The stress-strain curves appropriate to different strain rates were inferred by proportionally translating the plastic part of the curve to match the different strain-rate-dependent yield stresses in Ref. [170] to give the best guess curves in Figure 40. It should be noted that the above analysis assumes that the Young's modulus is independent of strain rate. It is possible that the stress-strain curve takes a different form at high strain rates. However, in view of the lack of the available data, the curves plotted in Figure 40 are probably the best estimate available at this time. If the strain rate is higher than 4,900/s, the dynamic behavior of the BMG at 4,900/s is assumed, which will clearly underestimate the strain-rate softening effect at very high strain rates.

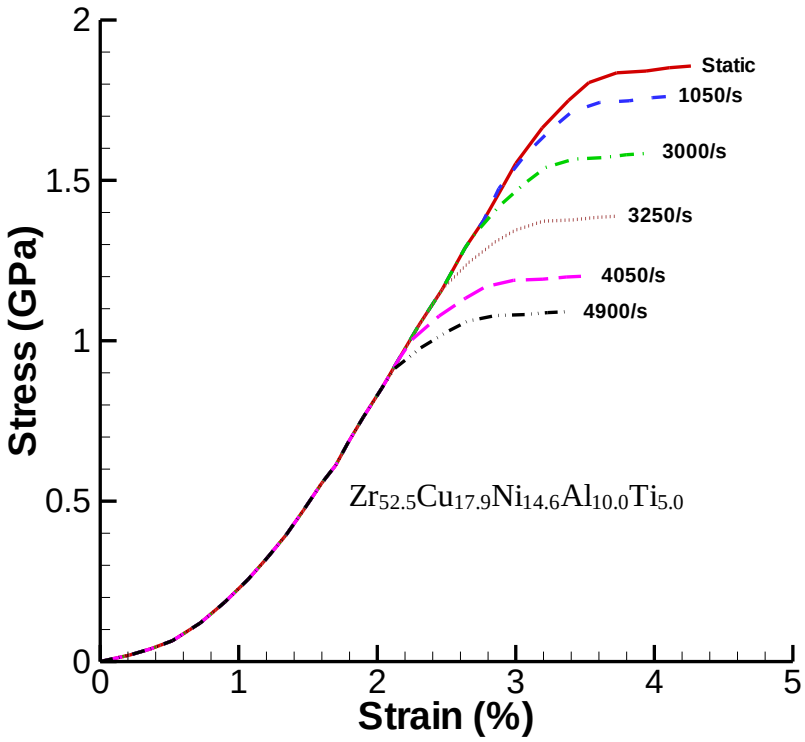

Figure 40. Inferred strain-rate effects on the stress-strain curve for BMG (Vit-1)

5.5 Summary

The main results for laser effects on the plasticity improvement of BMGs can be summarized as follows:

- The composition of BMGs is found to have no effect on the laser-induced improvement, that is, laser shock peening can improve the ductility for both relatively ductile and brittle BMGs investigated in this study;
- The compressive stress-stain curves of Zr-based BMGs treated by different levels of laser power were obtained and plasticity was improved increasingly from laser power of 7 GW/cm^2 to 9 GW/cm^2;
- The morphology with the interactions or intersection of shear bands after laser treatment was found at the sample surface as the plasticity improved;
- The hardness changes on the lateral surface after laser shock peening were mapped using nanoindentation. Compared to the bulk center, the hardness of laser-peened layer is reduced;
- The fatigue behavior was investigated and no obvious changes compared to shot-peened method.
- Residual stresses (RS) was measured by focused-ion beam (FIB) assisted micro-slot cutting method, the maximum RS was found at around 50 um below the surface, and depth profile of RS were obtained;
- The microstructure changes were studied using the pair-distribution function (PDF) obtained from synchrotron X-ray diffraction, and the peak shift was observed in the PDF which indicates the RS was introduced by laser peening;

- The relationship between the shear-band operation and the stick-slip behavior was investigated.
- The CCDF curves have been calculated to describe the serration behavior of BMGs, and were successfully applied on laser-treated BMGs, revealing the information of shear-band activities.

CHAPTER VI THERMOGRAPH INVESTIGATION ON SHEAR-BAND EVOLUTION

6.1 Introduction

As widely accepted, bulk metallic glasses deform through shear bands' formation and propagation. Thus, the investigation and characterization of shear bands are essential to understand the deformation mechanism of BMGs. However, currently very limited techniques could be applied for the in-situ study of shear-band activities, since shear band operates at tens of nanosecond and several nanometers, such as acoustic emission, which has very high sensitivity for temporal resolution, but lost the capability to characterize the spatial information of shear bands. Recent work has shown that temperature rises significantly within shear bands [172, 176, 177]. It was assumed that the temperature increases may play a critical role in shear-banding phenomena, subsequent deformation, and fracture [178]. Inspired from this point, in the present study, thermograph imaging technique was used to provide a unique way to identify and quantify the shear band operations.

During the compression experiment, the local temperature evolution [178] can be described by

$$\rho C_v \frac{\partial T}{\partial t} + v \cdot \nabla T = T : \nabla v - \nabla \cdot q \tag{15}$$

where T is the specimen temperature, ρ is the density, C_v is the specific heat capacity, ∇v is the velocity gradient tensor (corresponding to the strain rate), and q is the heat flux. This equation applies to every point in the sample. The velocity gradient tensor ∇v in compression is

$$\nabla v = \begin{pmatrix} \dot{\varepsilon} & 0 & 0 \\ 0 & \frac{\dot{\varepsilon}}{2} & 0 \\ 0 & 0 & \frac{\dot{\varepsilon}}{2} \end{pmatrix} \tag{16}$$

where $\dot{\varepsilon}$ is the strain rate in units of reciprocal second. Hence, the deviatoric stress contribution to the temperature equation is

$$\sigma : \nabla v = 3\eta\dot{\varepsilon}^2 \tag{17}$$

Therefore, we can obtain the one dimension form of Eq. (13):

$$\rho C_v \frac{\partial T}{\partial t} = 3\eta\dot{\varepsilon}^2 - k\nabla^2 T \tag{18}$$

6.2 Experimental Methods

In this study, the Zr-based BMG Vitreloy 105 (Vit-105, $Zr_{52.5}Cu_{17.9}Ni_{14.6}Al_{10.0}Ti_{5.0}$ in atomic percent, at.%) was used according to its relatively good glass forming ability and ductility. The samples were prepared by arc-melting the mixtures of constituent metals with purity higher than 99.9% in a Ti-gettered high-purity argon atmosphere, and the molten alloy is suction cast to a rod with a length of 60 mm. To prepare for the compression experiments, the rods were cut into cylindrical specimens with 4 mm in length and 2 mm in diameter. Two compression ends were carefully polished to be parallel.

The compression experiment was conducted by Material Test System (MTS) 810 machine controlled by a computer at room temperature. The initial strain rate was set to 2 $\times 10^{-3}$/s, and a data-acquisition rate of 100 Hz was used for the analysis. During compression process, a FLIR SC5000 Infrared (IR) Imaging System was employed to observe the in-situ dynamic evolution of temperature on the surface of the specimens at a frame rate of 300 Hz. This camera operates in the 2.5 to 5.1 μm waveband, and is equipped with a cooled Indium Antimonide (InSb) detector with a sensitivity (or Noise Equivalent Temperature Difference, NETD) smaller than 20 mK at room temperature. The spatial resolution of this camera can reach 15 μm. Before experiment, a thermocouple was attached to a specimen to calibrate the IR camera. Each frame of the recorded video and temperature data were then analyzed.

6.3 Results

The temperature evolution on the sample surface was plotted in the video using the raw data from IR camera. 28 serration events can be identified by the heat bands. The occurrences of heat release and stress drop matches very well. Even the small spots of temperature burst are perceptible in the video. The histogram of the temperature data is plotted at the right up corner, showing the distribution of temperatures for each frame. From the beginning of the video, it is evident that heat activation can be found from both ends. Intuitively, each serration exhibits as a heat band on the surface, and its temperature and width generally becomes larger as external load increases. As plotted in Figure 41, one single heat releasing process is illustrated using five representive points. At point 1,

the peak of each stress drop, temperature bust can be found on the sample surface as a thin and discontinued heat band, implying the initiation of the sudden slip. During the drop, as shown at point 2, the released heat is increasing, leading to a dramatical temperature rise. At point 3 at the valley bottom of the stress, which roughly marks the end of the heat releasing process, the heat band becomes wider and wider, due to the activity of heat dissipation or heat conduction. At point 4 in the stress rise region, no heat burst can be observed and the heat continues diffusing to the surrounding bulk materials. At point 5 which is far away from the heat releasing event, the temperature on the surface diminishes significantly. This process summarizes the thermal activities for the period of each sudden slip and the following stress rise.

To check the consistence of the location for each path of different serrations, the first frame of each serration (28 in total) was superimposed with appropriate transparency. As plotted in Figure 42(a), the ridge-like morphology readily reveals that most paths are located at the same position on the sample surface. Indeed, from 5th serration, almost all paths follow the same path in the video, except 7th and 11th serrations, which will be discussed later. If we look along the view angle marked by the black arrow in Figure 42(a), the lateral view are obtained and plotted in Figure 42(b). Besides the main ridge, there exist temperature bursts at different places (right-hand side), which are attributed to shear-band operation at very beginning period (4th and 7th serration), which can be observed in the video. The superposition indicates that after 5th serration, the primary shear-band path is softened and "percolated". The consecutive serrations mostly occur along this same softened path, suggesting a reactivation process of shear band instead of new nucleation. Note that even though we talk about path here, it's actually an ellipse

cross-section plane in a 3-dimensional space. Here for the plane we roughly refer to the surface for shear-band activities, which is not the single atomic plane as Ref. [128] discussed.

Generally, as the external load continuously increases, the released heat of each serration keeps rising up, as well as the magnitude of stress drop. Interestingly, as shown in Figure 43(a), the occurrence of stress drop and the temperature burst can be found as synchronized, clearly demonstrating that the serration behavior is associated with shear-band activities from the data aspect besides from the observation in the video. Thus, the magnitudes of temperature rise and stress drop are calculated, and plotted in Figure 43(b). A very good linear relationship can be found between these two quantities. Temperature is comes from the released heat, and stress drop is related to the energy stored or accumulated during the stick-slip process. The relationship between released heat and stored energy will be delineated later.

6.4 Discussion

6.4.1 Model of shear-band propagation

For most BMGs, the first stress drop actually can be found far below the nominal yielding point in the stress-strain curve. Thus we use "yielding region" to name the range from the first stress drop to the nominal yielding point. According to the thermograph results in the present study, the deformation can be divided into two stages: immature shear-band and mature shear-band stages. We will use Stage I and Stage II for simplicity thereafter in the current work. For Stage I (serration No. 1 - 4, corresponding to the

yielding region), primary shear band is activated from both sides simultaneously and prepares a potential sliding plane. At beginning, only the heat release at both ends can be detected, which indicates that the sliding actually starts from both ends of the path and the center region is relatively cold, i.e., the heat generated from deformation is not homogeneously distributed along the plane. Meanwhile, localized shear bands can be found to initiate at places other than the sliding path, which also manifest as the small stress drops. Within Stage II, the primary shear band "percolates", and the softened path is prepared. From now on, the deformation is mainly accommodated within the path, as demonstrated in Figure 42. Still there are few localized shear-band activations, which are scattered within the sample, leading to the tiny stress drop which overlaps the main stress drop. So actually we can combine 7th and 8th serrations as one, as well as 11th and 12th serrations. The heat release becomes larger as external load increases, which may be attributed to the continuously weakened path (or plane) by serration events. The above two-stage model can be named as single shear-band control model (SSBCM), and is especially suitable for relatively brittle BMGs. There are actually other cases where multiple shear bands dominate for ductile BMGs, which is a more complicated process. In recent work, two models were suggested for shear-band propagation [179-181]. One is the most used and simulation supported, which describes that shear band initiates at one side and propagates to the other sides [179-183]; the other simultaneous model was also proposed, simply illustrating that the shear occurs actually simultaneously across the plane [179-181, 184]. However, the SSBCM from current work is a slightly different and revealing more specific details compared to the simultaneous model [179-181], that is, at Stage I, the shear already occurs across the plane, but the heat generated is

inhomogeneous, showing hot at both ends of path but cold in the center; while at Stage II, the softened path is served as the main deformation zone, as discussed above. The IR camera can capture every detail about the heat releases, and clearly unveil their corresponding relationship to shear-band activities and serration. This is especially the case for the yielding region or stage I, as well as the small or tiny stress drops within the overlapping serration in the stage II, which is usually omitted in the previous works with focus on the stage II, or using high-speed camera but very hard to detect [185, 186]. These details are indispensable to paint the whole picture of the shear-band evolution process. In addition, one should note that even though the grouped serrations used for each stage here may not be so accurate since it's only from the surface temperature, it has no influence on the description of the above model.

6.4.2 Spatiotemporal fitting

Besides, the thermo-analysis can be made based on the temperature data to extract the paramount information about shear-band operation. The thin-film solution of the 1-D heat diffusion equation can be expressed as [172]:

$$\Delta T = \frac{H}{\rho C_p} \cdot \frac{1}{\sqrt{4\pi\alpha t}} \exp(\frac{-x^2}{4\alpha t}) \tag{19}$$

where H is the heat content, ρ the density of the material, C_p the specific heat capacity, t the elapsed time, x the distance from the shear band center, and α the thermal diffusivity, which can be obtained by $\alpha = k / \rho C_p$ with the thermal conductivity, k. For the materials investigated in the present study, specific heat C_p = 330 J/kg·K [187, 188], density ρ =

6730 kg/m^3 [189], $\alpha = 3 \times 10^{-6}$ m^2/s [190-192]. Plugging all these constants into Eq. (1), one can easily obtain the function $\Delta T(x,t)$ with undetermined H, which depicts the distribution of temperature rises over spatial and temporal domains. In previous studies, heat content H can be deduced by measuring the hot-band width using fusible-coating method [172], or estimated based on the heat converted from entire work done by shear with a coefficient [190, 192-195], which uses the limited number of shear offsets or shearing layer thickness from the microscopic measurement, or approximated values. Even though these methods can calculate the representive value of H, it's very hard to acquire the heat release for each serration, which is resulted from the difficulties to match each single serration event with the corresponding microscopy-obtained hot-band width, or shear offset, or thickness of shearing layer. However, H carries the information of the extent to which sample deformed, thus, should be treated individually, which is essential to reveal the evolution of shear-band activities, as found in Figure 43(a) that maximum temperature and stress drop becomes larger as external load increases. Therefore, in the present study, a spatiotemporal fitting procedure is proposed to derive H for each serration event. As shown in the inset of Figure 44, a path perpendicular to the heat band marked by the black arrow line was selected to collect the thermodata. The red crosses are experimental temperature data from IR camera, and the surface is fitted using Eq. (1) based on the least-squares algorithm, which gives the best fitting when the minimum of the squares of residuals are achieved, and in principle is expressed as:

$$LQ = \min \sum_i \left| y_i - \hat{y}_i \right|^2 \tag{20}$$

where y_i is the experimental temperature value at each point of the spatiotemporal surface in Figure 44, and $\hat{y}_i$ is the predicted value using Eq. (1) which is presented as the surface in Figure 44. Given the initial values of parameters (e.g., *H*), the minimized *LQ* can be found with enough iteration (details in the supplement file).

All the values of fitted *H* are listed in Table 3. The results of current work range from 789.27 to 8034.31 J/m^2 for Vit-105, which is well comparable to the reported *H* lying in-between 400 - 2200 J/m^2 for Vit-1 [172]. Moreover, the fitting method readily shows that the heat release exhibits in an increasing trend. As investigated by the work, other factors, e.g., sample size, can also affect the quantity of heat content. The surface fitting considers the temperature evolution utilizing 3-D data from both spatial and temporal aspects, which dramatically improves the accuracy of the fitted results compared to 2-D fitting of temperature vs. either time or distance from shear band center.

Now the scenario of shear-band activities is much clearer. More specifically, energy is accumulated during the stress-rise period, and suddenly releases in the form of heat along shear bands with the stress drop occurring (may also induce structural changes but cannot be observed in the thermo image), and dissipates to the vicinity of shear band. Thus, the accumulated energy stored for each serration event was calculated, and compared to the fitted *H*. The calculated results were also listed in Table 3. The average percentage of released heat (fitted H) to the stored energy is 0.664 ± 0.173, smaller than the coefficient, 0.9, used in the estimation of previous work [193, 195].

Table 3. The comparison between the fitted heat content, H, from the thermodata and the calculated H from the stress-time curve and stress-displacement curve

	Fitted H from Thermodata (J/m^2)	Calculated H from S-t curve (J/m^2)	Calculated H from S-D curve (J/m^2)
7	2223.36	3252.13	2940.31
9	2391.01	1926.54	3768.93
10	2544.87	4737.91	5258.91
13	4264.73	3866.33	3047.69
14	2085.56	4276.09	3907.16
15	2478.45	5035.66	3943.91
16	2484.95	3400.25	3426.32
17	3868.88	5179.05	4618.06
18	4140.95	6793.42	4733.96
19	4726.56	5902.23	5127.61
20	4854.47	7961.13	7484.99
21	3672.42	4700.98	4724.10
22	3637.28	6318.20	4464.12
23	5464.29	4849.83	4062.73
24	4987.31	8197.53	6887.91
25	7055.91	7760.09	6156.39
26	7844.57	9460.05	8418.11
27	8034.31	9267.45	7241.37
28	6870.26	8761.10	5386.41

* Here S: stress, t: time, and D: displacement

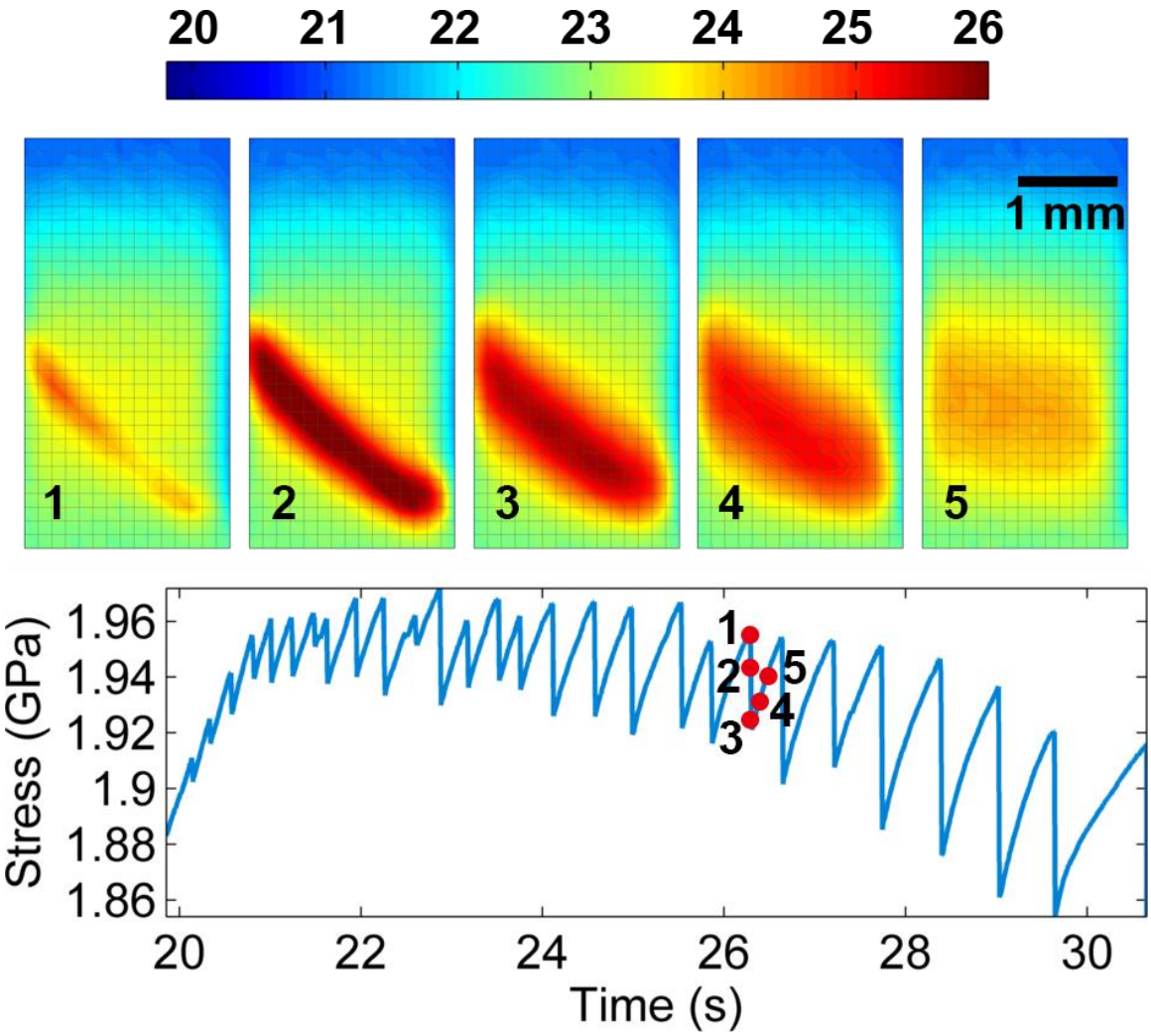

Figure 41. Thermography image shows the relationship between the heat dissipation from the shear-band evolution (figures marked by 1, 2, 3, 4, and 5) and the corresponding stress (points marked by 1, 2, 3, 4, and 5) with IR camera at 300 Hz. The temperature scale (°C) is indicated by the color legend.

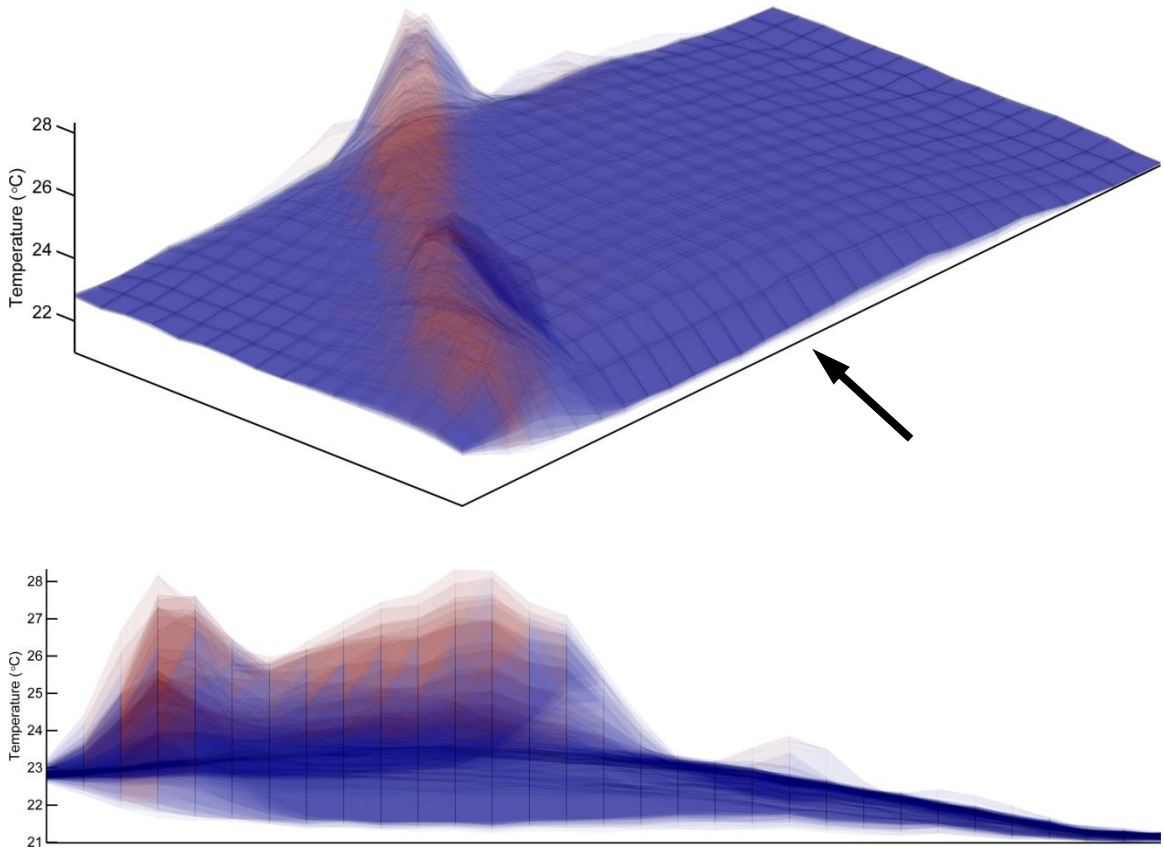

Figure 42. (a) Ridge-like morphology of temperature distribution obtained by superimposing the first frame of each serration event (28 in total), indicating that mature shear band initiates at the same location; (b) lateral view from the black arrow direction in (a) shows that there exist temperature bursts at different places (right-hand side), which are attributed to shear-band operation at very begin period, which can be observed in the video.

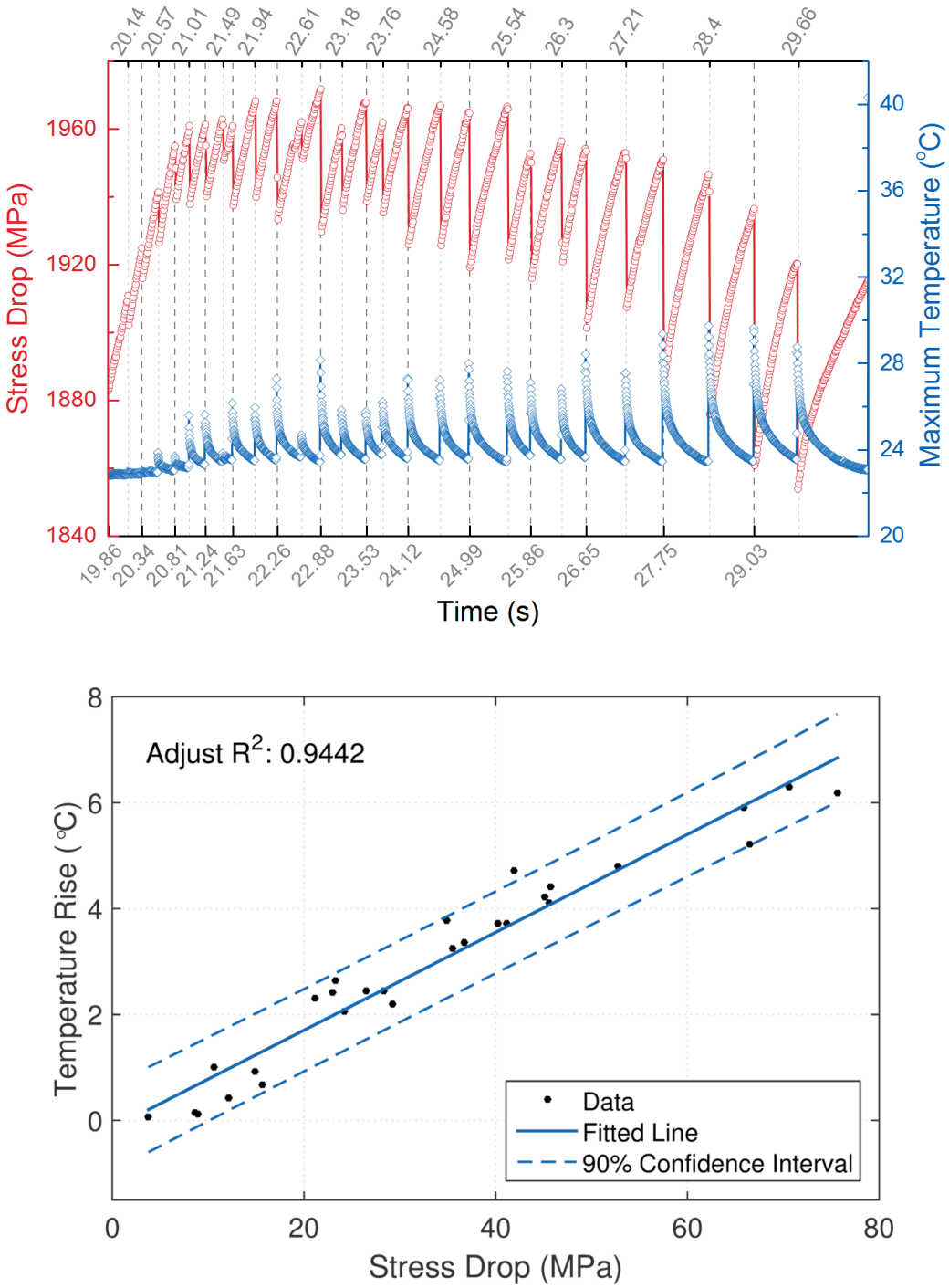

Figure 43. (a) The corresponding time for the occurrence of stress drop and maximum temperature, and (b) the linear relationship between temperature rise and stress drop

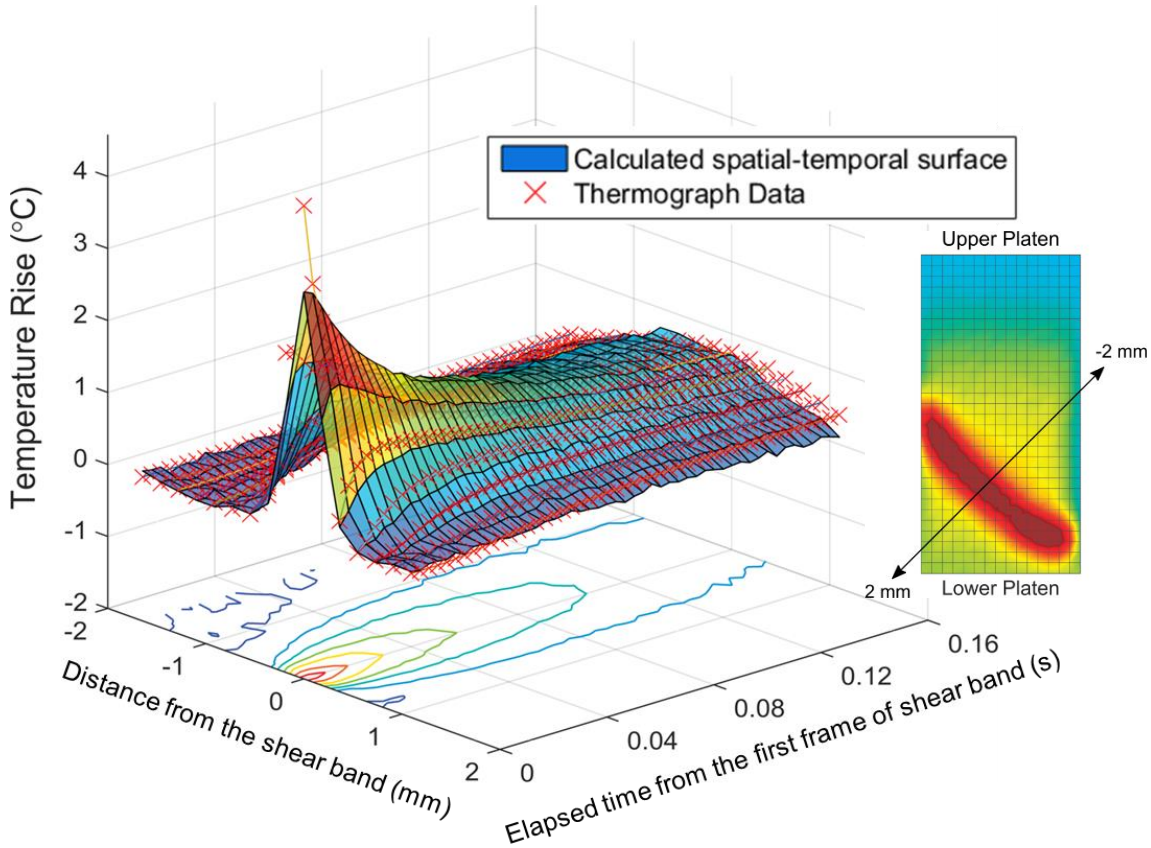

Figure 44. Spatial-temporal surface fitting of the temperature data from thermograph, and the inset shows the linear profile used for the spatial calculation, which is perpendicular to the shear-band softened path.

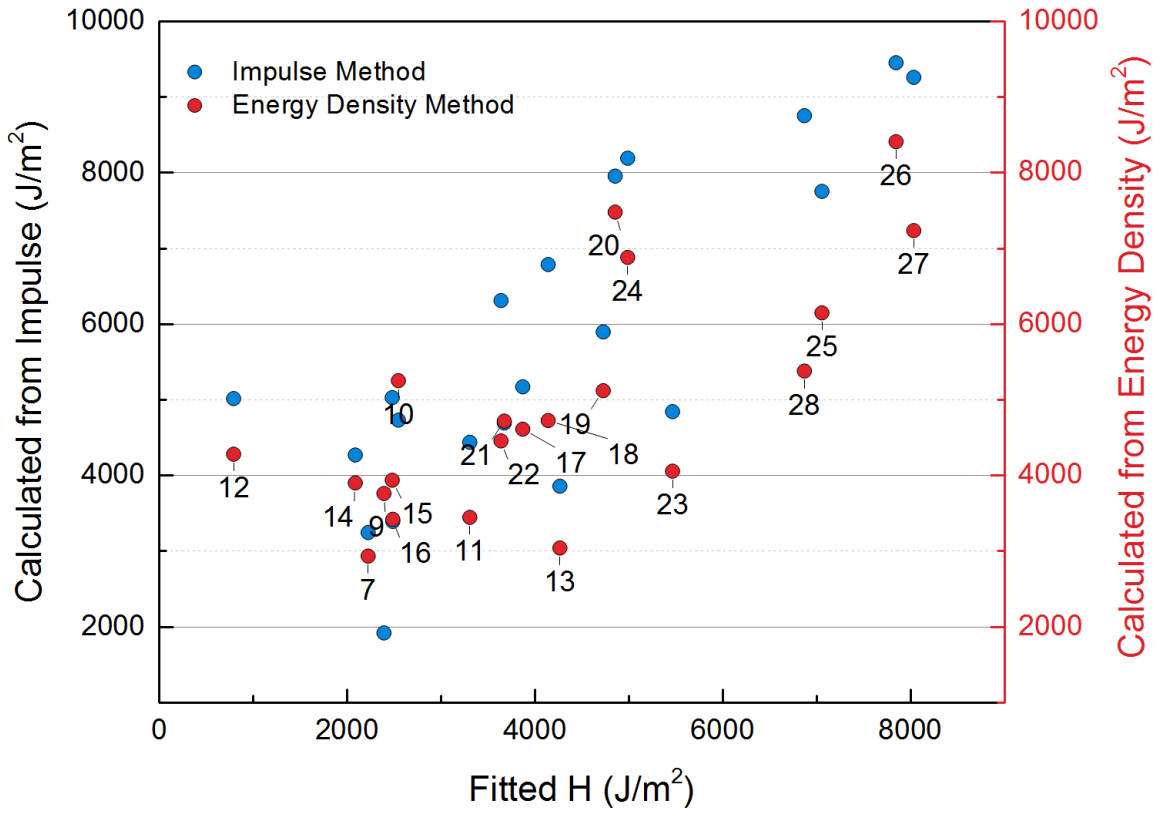

Figure 45. The relationship between the fitted *H* from the spatial-temporal surface and the energy content calculated from stress-strain curved using time-based (left Y-axis) and displacement-based (right Y-axis) methods. The marked numbers indicate the sequence of serration events.

6.5 Summary

Through the thermograph study, plenty of information was unveiled for the shear-band evolution, which is usually neglected in previous work, and the following issues are clarified. The stress drops in the serration region are one to one corresponding to the shear band activities. The small stress drops in the yielding region and tiny drop overlapping on the large stress drop in Stage II are also indicates the operation of shear bands. A modified model of the shear-band propagation was proposed. The linear relationship between stress drop and temperature rise was revealed. Besides, The heat content H was fitted from the spatiotemporal surface of the temperature data using IR camera, and is comparable to the literature value for Vit-1, which gives an easy way to extract the H for each serration event. The stored energy was also calculated from the stress-time curve and compared to the fitted H, and a coefficient was obtained. It's expected that these results and methods could shed light on the fundamental understanding of deformation of BMGs, as well as the studies for other traditional and advanced materials.

CHAPTER VII SUMMARY AND CONCLUSION

In this study, three methods which can improve the plasticity of BMGs were investigated and characterized, including geometrical-constraint, pre-fatigue, and laser-peening induced constraint methods. The improvement of plasticity was successfully obtained. The geometrical-constraint study provides an easy method to distinguish the plasticity from sample intrinsic properties or from the combination of sample and machine frame. Specifically, under the unconstrained condition, which is the standard for compression tests, the stress drop and displacement burst will keep increasing as the system has no boundary constrained for shear band propagation. In contrast, the decreasing trend can be found in the constrained condition, both for the stress drop and displacement burst, implying that the system actually prevents the propagation of shear bands and avoid the catastrophic fracture. Huge shear bands interactions can be observed on the lateral surface of compressed sample under constrained condition, which is responsible for the prolonged plasticity. While only several shear bands can be found in the fractured sample under unconstrained condition. The slip duration and waiting time didn't show strong trend under both unconstrained and constrained conditions at various strain rates. The features of trend were successfully applied in the case of nanoindentation, where the deformation is localized and constrained by the surrounding bulk materials, and good agreement was achieved between the constrained trend and stress-drop pattern from pop-ins.

The pre-fatigue method could improve the plasticity for both ductile and brittle compositions. Using various cycles leads to different extent of the improvement. Different compositions also have effects on the improvement, e.g., more improvement can be found for a relatively ductile composition ($Zr_{64.13}Cu_{15.75}Ni_{10.12}Al_{10}$ in this study).

Generally, 10^4 cycles didn't contribute to the improvement. From 10^5 cycles, discernible changes can be observed, and when increasing to 10^6 cycles, obvious improvement was obtained, compared to the results of as-cast sample, but large fluctuation of the plasticity is found during the repeated compression experiments. From the characterization of the fracture surface, huge shear-band network can be spotted on the S6 sample, which could result in the extended plasticity. With the statistical method, the stress-drop patterns for all samples are analyzed, and features for processing with different cycles can be distinguished. To investigate the local changes at the anelastic sites, synchrotron diffraction experiment is proposed. The synchrotron data is still being analyzed.

The plasticity of bulk metallic glasses was improved using the laser shock peening through introducing the compressive residual stresses and shear bands. By adapting various laser power levels and coating layers, the optimal effect for the improvement can be achieved. The improvement was confirmed in mechanical tests, as compression experiments. Furthermore, the mechanism of the improvement was identified, and the residual stresses induced by laser peening was mapped and related to the deformation mechanism. Finally, a 3-D finite-element model is developed to compare with experimental results and provide the prediction for the future study. A theoretical model to analyze the plasticity is developed for the investigation of the deformation dynamics.

Through the thermograph study, plenty of information was unveiled for the shear-band evolution, which is usually neglected in previous work, and the following issues are clarified. The stress drops in the serration region are one to one corresponding to the shear band activities. The small stress drops in the yielding region and tiny drop

overlapping on the large stress drop in Stage II are also indicates the operation of shear bands. A modified model of the shear-band propagation was proposed. The linear relationship between stress drop and temperature rise was revealed. Besides, The heat content *H* was fitted from the spatiotemporal surface of the temperature data using IR camera, and is comparable to the literature value for Vit-1, which gives an easy way to extract the *H* for each serration event. The stored energy was also calculated from the stress-time curve and compared to the fitted H, and a coefficient was obtained. It's expected that these results and methods could shed light on the fundamental understanding of deformation of BMGs, as well as the studies for other traditional and advanced materials.

CHAPTER VIII FUTURE WORK

Besides the efforts shown in the present study, some extra work still needs to be done to improve the understanding of the deformation mechanism of BMGs, which are listed as below:

- Serration behavior analysis of pop-ins in the nanoindentation results;
- In-situ synchrotron study of the samples in fatigue-compression experiments to investigate the structural changes;
- More studies on the thermograph for compression at different strain rates;
- Thermograph study of tension experiments;
- Thermograph study combined with strain gages;
- Acoustic emission study of the plastic deformation under different loading conditions.

All these work should be carefully designed to achieve a better understanding of the shear band dynamics.

LIST OF REFERENCES

[1] W. H. Wang, C. Dong, and C. H. Shek, "Bulk metallic glasses", *Mater. Sci. Eng., R*, 2004, 44(2-3), pp. 45-89.
[2] A. L. Greer, "Metallic glasses", *Science*, 1995, 267(5206), pp. 1947-1953.
[3] A. Peker and W. L. Johnson, "A highly processable metallic glass: $Zr_{41.2}Ti_{13.8}Cu_{12.5}Ni_{10.0}Be_{22.5}$", *Appl. Phys. Lett.*, 1993, 63(17), pp. 2342-2344.
[4] A. Inoue, "Stabilization of metallic supercooled liquid and bulk amorphous alloys", *Acta Mater.*, 2000, 48(1), pp. 279-306.
[5] W. Zhang and A. Inoue, "Formation and mechanical properties of Ni-based Ni–Nb–Ti–Hf bulk glassy alloys", *Scripta Materialia*, 2003, 48(5), pp. 641-645.
[6] C. J. Gilbert, R. O. Ritchie, and W. L. Johnson, "Fracture toughness and fatigue-crack propagation in a Zr-Ti-Ni-Cu-Be bulk metallic glass", *Appl. Phys. Lett.*, 1997, 71(4), pp. 476-478.
[7] A. Inoue, H. Koshiba, T. Itoi, and A. Makino, "Ferromagnetic Co-Fe-Zr-B amorphous alloys with glass transition and good high-frequency permeability", *Appl. Phys. Lett.*, 1998, 73(6), pp. 744-746.
[8] A. Inoue, T. Zhang, W. Zhang, and A. Takeuchi, "Bulk Nd-Fe-Al amorphous alloys with hard magnetic properties", *Materials Transactions Jim*, 1996, 37(2), pp. 99-108.
[9] G. Y. Wang, M. D. Demetriou, J. P. Schramm, P. K. Liaw, and W. L. Johnson, "Compression-compression fatigue of $Pd_{43}Ni_{10}CU_{27}P_{20}$ metallic glass foam", *J. Appl. Phys.*, 2010, 108(2).
[10] G. Y. Wang, P. K. Liaw, X. Q. Jin, Y. Yokoyama, E. W. Huang, F. Jiang, L. M. Keer, and A. Inoue, "Fatigue initiation and propagation behavior in bulk-metallic glasses under a bending load", *J. Appl. Phys.*, 2010, 108(11), p. 113512.
[11] G. Y. Wang, P. K. Liaw, and M. L. Morrison, "Progress in studying the fatigue behavior of Zr-based bulk-metallic glasses and their composites", *Intermetallics*, 2009, 17(8), pp. 579-590.
[12] G. Y. Wang, P. K. Liaw, Y. Yokoyama, A. Inoue, and C. T. Liu, "Fatigue behavior of Zr-based bulk-metallic glasses", *Mater. Sci. Eng., A*, 2008, 494(1-2), pp. 314-323.
[13] G. Y. Wang, P. K. Liaw, Y. Yokoyama, A. Peker, W. H. Peter, B. Yang, M. Freels, Z. Y. Zhang, V. Keppens, R. Hermann, R. A. Buchanan, C. T. Liu, and C. R. Brooks, "Studying fatigue behavior and Poisson's ratio of bulk-metallic glasses", *Intermetallics*, 2007, 15(5-6), pp. 663-667.
[14] S. J. Pang, T. Zhang, K. Asami, and A. Inoue, "Bulk glassy Fe-Cr-Mo-C-B alloys with high corrosion resistance", *Corros. Sci.*, 2002, 44(8), pp. 1847-1856.
[15] J. R. Scully, A. Gebert, and J. H. Payer, "Corrosion and related mechanical properties of bulk metallic glasses", *J. Mater. Res.*, 2007, 22(2), pp. 302-313.
[16] W. H. Peter, R. A. Buchanan, C. T. Liu, P. K. Liaw, M. L. Morrison, J. A. Horton, C. A. Carmichael, and J. L. Wright, "Localized corrosion behavior of a zirconium-based bulk metallic glass relative to its crystalline state", *Intermetallics*, 2002, 10(11-12), pp. 1157-1162.
[17] L. Huang, D. C. Qiao, B. A. Green, P. K. Liaw, J. F. Wang, S. J. Pang, and T. Zhang, "Bio-corrosion study on zirconium-based bulk-metallic glasses", *Intermetallics*, 2009, 17(4), pp. 195-199.
[18] M. F. Ashby and A. L. Greer, "Metallic glasses as structural materials", *Scripta Materialia*, 2006, 54(3), pp. 321-326.
[19] Y. Suzuki and T. Egami, "Shear deformation of glassy metals: Breakdown of cauchy relationship and anelasticity", *J. Non Cryst. Solids*, 1985, 75(1–3), pp. 361-366.
[20] W. Dmowski, T. Iwashita, C. P. Chuang, J. Almer, and T. Egami, "Elastic heterogeneity in metallic glasses", *Phys. Rev. Lett.*, 2010, 105(20), p. 205502.
[21] T. Egami, "Atomic level stresses", *Prog. Mater. Sci.*, 2011, 56(6), pp. 637-653.

[22] F. Spaepen, "A microscopic mechanism for steady state inhomogeneous flow in metallic glasses", *Acta Metall.*, 1977, 25(4), pp. 407-415.
[23] M. D. Demetriou, M. E. Launey, G. Garrett, J. P. Schramm, D. C. Hofmann, W. L. Johnson, and R. O. Ritchie, "A damage-tolerant glass", *Nat. Mater.*, 2011, 10(2), pp. 123-128.
[24] J. W. Qiao, Y. Zhang, and P. K. Liaw, "Serrated flow kinetics in a Zr-based bulk metallic glass", *Intermetallics*, 2010, 18(11), pp. 2057-2064.
[25] K. A. Dahmen, Y. Ben-Zion, and J. T. Uhl, "Micromechanical model for deformation in solids with universal predictions for stress-strain curves and slip avalanches", *Phys. Rev. Lett.*, 2009, 102(17), p. 175501.
[26] K. A. Dahmen, Y. Ben-Zion, and J. T. Uhl, "A simple analytic theory for the statistics of avalanches in sheared granular materials", *Nat. Phys.*, 2011, 7(7), pp. 554-557.
[27] H. Q. Li, C. Fan, K. X. Tao, H. Choo, and P. K. Liaw, "Compressive behavior of a Zr-based metallic glass at cryogenic temperatures", *Adv. Mater.*, 2006, 18(6), pp. 752-754.
[28] L. Yang, G. Q. Guo, L. Y. Chen, C. L. Huang, T. Ge, D. Chen, P. K. Liaw, K. Saksl, Y. Ren, Q. S. Zeng, B. LaQua, F. G. Chen, and J. Z. Jiang, "Atomic-scale mechanisms of the glass-forming ability in metallic glasses", *Phys. Rev. Lett.*, 2012, 109(10), p. 105502.
[29] G. Ananthakrishna, S. J. Noronha, C. Fressengeas, and L. P. Kubin, "Crossover from chaotic to self-organized critical dynamics in jerky flow of single crystals", *Phys. Rev. E*, 1999, 60(5), pp. 5455-5462.
[30] J. Balik and P. Lukac, "PORTEVIN-LE CHATELIER INSTABILITIES IN AL-3 MG CONDITIONED BY STRAIN-RATE AND STRAIN", *Acta Metall. Mater.*, 1993, 41(5), pp. 1447-1454.
[31] G. Besnard, F. Hild, and S. Roux, ""Finite-Element" displacement fields analysis from digital images: Application to portevin-le chatelier bands", *Experimental Mechanics*, 2006, 46(6), pp. 789-803.
[32] Y. Brechet and Y. Estrin, "ON THE INFLUENCE OF PRECIPITATION ON THE PORTEVIN-LE CHATELIER EFFECT", *Acta Metall. Mater.*, 1995, 43(3), pp. 955-963.
[33] K. Chihab, Y. Estrin, L. P. Kubin, and J. Vergnol, "THE KINETICS OF THE PORTEVIN-LE CHATELIER BANDS IN AN AL-5 ATMOSPHERIC PERCENT-MG ALLOY", *Scripta Metallurgica*, 1987, 21(2), pp. 203-208.
[34] A. H. Cottrell, "A NOTE ON THE PORTEVIN-LE CHATELIER EFFECT", *Philos. Mag.*, 1953, 44(355), pp. 829-832.
[35] P. Hahner, "On the critical conditions of the Portevin Le Chatelier effect", *Acta Mater.*, 1997, 45(9), pp. 3695-3707.
[36] P. Hahner, A. Ziegenbein, E. Rizzi, and H. Neuhauser, "Spatiotemporal analysis of Portevin-Le Chatelier deformation bands: Theory, simulation, and experiment", *Physical Review B*, 2002, 65(13), p. 134109.
[37] S. Kok, M. S. Bharathi, A. J. Beaudoin, C. Fressengeas, G. Ananthakrishna, L. P. Kubin, and M. Lebyodkin, "Spatial coupling in jerky flow using polycrystal plasticity", *Acta Mater.*, 2003, 51(13), pp. 3651-3662.
[38] M. Lebyodkin, Y. Brechet, Y. Estrin, and L. Kubin, "Statistical behaviour and strain localization patterns in the Portevin-Le Chatelier effect", *Acta Mater.*, 1996, 44(11), pp. 4531-4541.
[39] M. Lebyodkin, L. Dunin-Barkowskii, Y. Brechet, Y. Estrin, and L. P. Kubin, "Spatio-temporal dynamics of the Portevin-Le Chatelier effect: Experiment and modelling", *Acta Mater.*, 2000, 48(10), pp. 2529-2541.
[40] M. A. Lebyodkin, Y. Brechet, Y. Estrin, and L. P. Kubin, "STATISTICS OF THE CATASTROPHIC SLIP EVENTS IN THE PORTEVIN-LE CHATELIER EFFECT", *Phys. Rev. Lett.*, 1995, 74(23), pp. 4758-4761.

[41] McCormic.Pg, "PORTEVIN-LE CHATELIER EFFECT IN AN AL-MG-SI ALLOY", *Acta Metall.*, 1971, 19(5), pp. 463-&.
[42] McCormic.Pg, "MODEL FOR PORTEVIN-LE CHATELIER EFFECT IN SUBSTITUTIONAL ALLOYS", *Acta Metall.*, 1972, 20(3), pp. 351-&.
[43] P. Penning, "MATHEMATICS OF PORTEVIN-LE CHATELIER EFFECT", *Acta Metall.*, 1972, 20(10), pp. 1169-&.
[44] R. C. Picu, "A mechanism for the negative strain-rate sensitivity of dilute solid solutions", *Acta Mater.*, 2004, 52(12), pp. 3447-3458.
[45] E. Rizzi and P. Hahner, "On the Portevin-Le Chatelier effect: theoretical modeling and numerical results", *International Journal of Plasticity*, 2004, 20(1), pp. 121-165.
[46] J. M. Robinson and M. P. Shaw, "MICROSTRUCTURAL AND MECHANICAL INFLUENCES ON DYNAMIC STRAIN-AGING PHENOMENA", *Int. Mater. Rev.*, 1994, 39(3), pp. 113-122.
[47] S. H. Vandenbrink, A. Vandenbeukel, and P. G. McCormick, "STRAIN RATE SENSITIVITY AND PORTEVIN-LE CHATELIER EFFECT IN AU-CU ALLOYS", *Physica Status Solidi a-Applied Research*, 1975, 30(2), pp. 469-477.
[48] W. M. Wang, L. J. Sluys, and R. deBorst, "Viscoplasticity for instabilities due to strain softening and strain-rate softening", *International Journal for Numerical Methods in Engineering*, 1997, 40(20), pp. 3839-3864.
[49] B. A. Wilcox and G. C. Smith, "PORTEVIN-LE CHATELIER EFECT IN HYDROGEN CHARGED NICKEL", *Acta Metall.*, 1964, 12(4), pp. 371-&.
[50] P. D. Zavattieri, V. Savic, L. G. Hector, J. R. Fekete, W. Tong, and Y. Xuan, "Spatio-temporal characteristics of the Portevin-Le Chatelier effect in austenitic steel with twinning induced plasticity", *International Journal of Plasticity*, 2009, 25(12), pp. 2298-2330.
[51] S. Zhang, P. G. McCormick, and Y. Estrin, "The morphology of Portevin-Le Chatelier bands: Finite element simulation for Al-Mg-Si", *Acta Mater.*, 2001, 49(6), pp. 1087-1094.
[52] S. M. Zhu and J. F. Nie, "Serrated flow and tensile properties of a Mg-Y-Nd alloy", *Scripta Materialia*, 2004, 50(1), pp. 51-55.
[53] L. P. Kubin, K. Chihab, and Y. Estrin, "The rate dependence of the portevin-Le chatelier effect", *Acta Metall.*, 1988, 36(10), pp. 2707-2718.
[54] J. M. Robinson and M. P. Shaw, "Microstructural and mechanical influences on dynamic strain aging phenomena", *Int. Mater. Rev.*, 1994, 39(3), pp. 113-122.
[55] P. Hähner, "On the physics of the Portevin-Le Châtelier effect part 1: The statistics of dynamic strain ageing", *Mater. Sci. Eng., A*, 1996, 207(2), pp. 208-215.
[56] O. N. Senkov and J. J. Jonas, "Dynamic strain aging and hydrogen-induced softening in alpha titanium", *Metall. Mater. Trans. A*, 1996, 27(7), pp. 1877-1887.
[57] P. Rodriguez, "Serrated plastic flow", *Bull. Mater. Sci.*, 1984, 6(4), pp. 653-663.
[58] D. Wu, R. S. Chen, and E. H. Han, "Serrated flow and tensile properties of a Mg–Gd–Zn alloy", *Mater. Sci. Eng., A*, 2012, 532(0), pp. 267-274.
[59] T. Sakthivel, K. Laha, M. Nandagopal, K. S. Chandravathi, P. Parameswaran, S. Panneer Selvi, M. D. Mathew, and S. K. Mannan, "Effect of temperature and strain rate on serrated flow behaviour of Hastelloy X", *Mater. Sci. Eng., A*, 2012, 534(0), pp. 580-587.
[60] V. Shankar, M. Valsan, K. B. S. Rao, and S. L. Mannan, "Effects of temperature and strain rate on tensile properties and activation energy for dynamic strain aging in alloy 625", *Metall. Mater. Trans. A*, 2004, 35 A(10), pp. 3129-3139.
[61] A. H. Clausen, T. Børvik, O. S. Hopperstad, and A. Benallal, "Flow and fracture characteristics of aluminium alloy AA5083–H116 as function of strain rate, temperature and triaxiality", *Mater. Sci. Eng., A*, 2004, 364(1–2), pp. 260-272.

[62] S. Venkadesan, C. Phaniraj, P. V. Sivaprasad, and P. Rodriguez, "Activation energy for serrated flow in a 15Cr-15Ni Ti-modified austenitic stainless steel", *Acta Metall. Mater.*, 1992, 40(3), pp. 569-580.

[63] J. Antonaglia, X. Xie, Z. Tang, C. W. Tsai, J. W. Qiao, Y. Zhang, M. O. Laktionova, E. D. Tabachnikova, J. W. Yeh, O. N. Senkov, M. C. Gao, J. T. Uhl, P. K. Liaw, and K. A. Dahmen, "Temperature effects on deformation and serration behavior of high-entropy alloys (HEAs)", *JOM*, 2014, 66(10), pp. 2002-2008.

[64] A. H. Cottrell and B. A. Bilby, "Dislocation theory of yielding and strain ageing of iron", *Proc. Phys. Soc. London, Sect. A*, 1949, 62(1), p. 49.

[65] C. W. Tsai, Y. L. Chen, M. H. Tsai, J. W. Yeh, T. T. Shun, and S. K. Chen, "Deformation and annealing behaviors of high-entropy alloy Al0.5CoCrCuFeNi", *J. Alloys Compd.*, 2009, 486(1-2), pp. 427-435.

[66] J. Megusar, A. S. Argon, and N. J. Grant, "Plastic flow and fracture in Pd80Si20 near Tg", *Materials Science and Engineering*, 1979, 38(1), pp. 63-72.

[67] C. A. Schuh, T. C. Hufnagel, and U. Ramamurty, "Mechanical behavior of amorphous alloys", *Acta Mater.*, 2007, 55(12), pp. 4067-4109.

[68] T. Mukai, T. G. Nieh, Y. Kawamura, A. Inoue, and K. Higashi, "Effect of strain rate on compressive behavior of a Pd40Ni40P20 bulk metallic glass", *Intermetallics*, 2002, 10(11-12), pp. 1071-1077.

[69] A. V. Sergueeva, N. A. Mara, D. J. Branagan, and A. K. Mukherjee, "Strain rate effect on metallic glass ductility", *Scripta Materialia*, 2004, 50(10), pp. 1303-1307.

[70] T. Okuno, A. Kawashima, H. Kurishita, W. Zhang, H. Kimura, and A. Inoue, "Influences of temperature and strain rate on mechanical behavior of a Cu45Zr45Al5Ag5 bulk glassy alloy", *Mater. Trans.*, 2008, 49(3), pp. 513-517.

[71] W. F. Ma, H. C. Kou, J. S. Li, H. Chang, and L. Zhou, "Effect of strain rate on compressive behavior of Ti-based bulk metallic glass at room temperature", *J. Alloys Compd.*, 2009, 472(1-2), pp. 214-218.

[72] S. Gonzalez, G. Q. Xie, D. V. Louzguine-Luzgin, J. H. Perepezko, and A. Inoue, "Deformation and strain rate sensitivity of a Zr-Cu-Fe-Al metallic glass", *Mater. Sci. Eng., A*, 2011, 528(9), pp. 3506-3512.

[73] N. Li, Q. Chen, and L. Liu, "Size dependent plasticity of a Zr-based bulk metallic glass during room temperature compression", *J. Alloys Compd.*, 2010, 493(1–2), pp. 142-147.

[74] S. Xie and E. P. George, "Size-dependent plasticity and fracture of a metallic glass in compression", *Intermetallics*, 2008, 16(3), pp. 485-489.

[75] W. F. Wu, Z. Han, and Y. Li, "Size-dependent "malleable-to-brittle" transition in a bulk metallic glass", *Appl. Phys. Lett.*, 2008, 93(6), p. 061908.

[76] Y. Yang and C. T. Liu, "Size effect on stability of shear-band propagation in bulk metallic glasses: an overview", *J. Mater. Sci.*, 2012, 47(1), pp. 55-67.

[77] F. F. Wu, Z. F. Zhang, B. L. Shen, S. X. Y. Mao, and J. Eckert, "Size effect on shear fracture and fragmentation of a Fe57.6Co14.4B19.2Si4.8Nb4 bulk metallic glass", *Adv. Eng. Mater.*, 2008, 10(8), pp. 727-730.

[78] F. F. Wu, Z. F. Zhang, S. X. Mao, and J. Eckert, "Effect of sample size on ductility of metallic glass", *Philos. Mag. Lett.*, 2009, 89(3), pp. 178-184.

[79] H. Bei, Z. P. Lu, S. Shim, G. Chen, and E. P. George, "Specimen size effects on Zr-based bulk metallic glasses investigated by uniaxial compression and spherical nanoindentation", *Metall. Mater. Trans. A*, 2010, 41A(7), pp. 1735-1742.

[80] C.-P. Chuang, T. Yuan, W. Dmowski, G.-Y. Wang, M. Freels, P. K. Liaw, R. Li, and T. Zhang, "Fatigue-induced damage in Zr-based bulk metallic glasses", *Sci. Rep.*, 2013, 3, p. 2578.

[81] W. H. Jiang, G. J. Fan, H. Choo, and P. K. Liaw, "Ductility of a Zr-based bulk-metallic glass with different specimen's geometries", *Materials Letters*, 2006, 60(29-30), pp. 3537-3540.

[82] H. Guo, P. F. Yan, Y. B. Wang, J. Tan, Z. F. Zhang, M. L. Sui, and E. Ma, "Tensile ductility and necking of metallic glass", *Nat. Mater.*, 2007, 6(10), pp. 735-739.

[83] X. J. Gu, S. J. Poon, G. J. Shiflet, and J. J. Lewandowski, "Compressive plasticity and toughness of a Ti-based bulk metallic glass", *Acta Mater.*, 2010, 58(5), pp. 1708-1720.

[84] Z. Han, W. F. Wu, Y. Li, Y. J. Wei, and H. J. Gao, "An instability index of shear band for plasticity in metallic glasses", *Acta Mater.*, 2009, 57(5), pp. 1367-1372.

[85] Y. J. Huang, J. Shen, and J. F. Sun, "Bulk metallic glasses: Smaller is softer", *Appl. Phys. Lett.*, 2007, 90(8), pp. 081919-3.

[86] W. H. Jiang, F. Jiang, F. X. Liu, H. Choo, P. K. Liaw, and K. Q. Qiu, "Temperature dependence of serrated flows in compression in a bulk-metallic glass", *Appl. Phys. Lett.*, 2006, 89(26), p. 261909.

[87] D. Pan, H. Guo, W. Zhang, A. Inoue, and M. W. Chen, "Temperature-induced anomalous brittle-to-ductile transition of bulk metallic glasses", *Appl. Phys. Lett.*, 2011, 99(24), p. 241907.

[88] A. Kawashima, Y. Zeng, M. Fukuhara, H. Kurishita, N. Nishiyama, H. Miki, and A. Inoue, "Mechanical properties of a Ni60Pd20P17B3 bulk glassy alloy at cryogenic temperatures", *Mater. Sci. Eng., A*, 2008, 498(1–2), pp. 475-481.

[89] Q. Wang, J. M. Pelletier, J. J. Blandin, and M. Suéry, "Mechanical properties over the glass transition of Zr41.2Ti13.8Cu12.5Ni10Be22.5 bulk metallic glass", *J. Non Cryst. Solids*, 2005, 351(27–29), pp. 2224-2231.

[90] F. H. Dalla Torre, A. Dubach, A. Nelson, and J. F. Loffler, "Temperature, strain and strain rate dependence of serrated flow in bulk metallic glasses", *Mater. Trans.*, 2007, 48(7), pp. 1774-1780.

[91] H. J. Jun, K. S. Lee, J. Eckert, and Y. W. Chang, "High-temperature deformation behavior and formability of a Zr-Cu-Al-Ni bulk metallic glass", *Metall. Mater. Trans. A*, 2008, 39A(8), pp. 1831-1837.

[92] J. Lu, G. Ravichandran, and W. L. Johnson, "Deformation behavior of the $Zr_{41.2}Ti_{13.8}Cu_{12.5}Ni_{10}Be_{22.5}$ bulk metallic glass over a wide range of strain-rates and temperatures", *Acta Mater.*, 2003, 51(12), pp. 3429-3443.

[93] B. Gutenberg and C. F. Richter, "Seismicity of the earth and associated phenomena", 1965, New York: Hafner.

[94] A. L. Barabasi and R. Albert, "Emergence of scaling in random networks", *Science*, 1999, 286(5439), pp. 509-512.

[95] R. N. Mantegna and H. E. Stanley, "Scaling behaviour in the dynamics of an economic index", *Nature*, 1995, 376(6535), pp. 46-49.

[96] G. B. West, J. H. Brown, and B. J. Enquist, "A general model for the origin of allometric scaling laws in biology", *Science*, 1997, 276(5309), pp. 122-126.

[97] H. Jeong, B. Tombor, R. Albert, Z. N. Oltvai, and A. L. Barabasi, "The large-scale organization of metabolic networks", *Nature*, 2000, 407(6804), pp. 651-654.

[98] N. Friedman, S. Ito, B. A. W. Brinkman, M. Shimono, R. E. L. DeVille, K. A. Dahmen, J. M. Beggs, and T. C. Butler, "Universal critical dynamics in high resolution neuronal avalanche data", *Phys. Rev. Lett.*, 2012, 108(20), p. 208102.

[99] M. C. Miguel, A. Vespignani, S. Zapperi, J. Weiss, and J.-R. Grasso, "Intermittent dislocation flow in viscoplastic deformation", *Nature*, 2001, 410(6829), pp. 667-671.

[100] M. Zaiser, B. Marmo, and P. Moretti, "The yielding transition in crystal plasticity - discrete dislocations and continuum models", in *International Conference on Statistical Mechanics of Plasticity and Related Instabilities*, 2005.

[101] M. C. Miguel, A. Vespignani, S. Zapperi, J. Weiss, and J.-R. Grasso, "Complexity in dislocation dynamics: model", *Mater. Sci. Eng., A*, 2001, 309-310, pp. 324-327.
[102] L. Laurson and M. J. Alava, "1/f noise and avalanche scaling in plastic deformation", *Phys. Rev. E*, 2006, 74(6 Pt 2), p. 066106.
[103] F. F. Csikor, C. Motz, D. Weygand, M. Zaiser, and S. Zapperi, "Dislocation avalanches, strain bursts, and the problem of plastic forming at the micrometer scale", *Science*, 2007, 318, pp. 251-254.
[104] P. D. Ispanovity, I. Groma, G. Gyorgyi, F. F. Csikor, and D. Weygand, "Submicron plasticity: yield stress, dislocation avalanches, and velocity distribution", *Phys. Rev. Lett.*, 2010, 105(8), p. 085503.
[105] G. Tsekenis, N. Goldenfeld, and K. A. Dahmen, "Dislocations jam at any density", *Phys. Rev. Lett.*, 2011, 106(10), p. 105501.
[106] G. Tsekenis, J. T. Uhl, N. Goldenfeld, and K. A. Dahmen, "Emporal and finite-size scaling properties of avalanches in plasticity exhibit mean field character", *Submitted*, 2014.
[107] M. Koslowski, "Scaling laws in plastic deformation", *Philos. Mag.*, 2007, 87(8-9), pp. 1175-1184.
[108] P. Y. Chan, G. Tsekenis, J. Dantzig, K. A. Dahmen, and N. Goldenfeld, "Plasticity and dislocation dynamics in a phase field crystal model", *Phys. Rev. Lett.*, 2010, 105(1), p. 015502.
[109] A. S. Argon, "Plastic deformation in metallic glasses", *Acta Metall.*, 1979, 27(1), pp. 47-58.
[110] N. Friedman, A. T. Jennings, G. Tsekenis, J.-Y. Kim, M. Tao, J. T. Uhl, J. R. Greer, and K. A. Dahmen, "Statistics of dislocation slip avalanches in nanosized single crystals show tuned critical behavior predicted by a simple mean field model", *Phys. Rev. Lett.*, 2012, 109(9), p. 095507.
[111] M. Zaiser, "Scale invariance in plastic flow of crystalline solids", *Adv. Phys.*, 2006, 55(1-2), pp. 185-245.
[112] B. D. Beake, G. A. Bell, W. Brostow, and W. Chonkaew, "Nanoindentation creep and glass transition temperatures in polymers", *Polymer International*, 2007, 56(6), pp. 773-778.
[113] J. Chen, X. Guo, Q. Tang, C. Zhuang, J. Liu, S. Wu, and B. D. Beake, "Nanomechanical properties of graphene on poly(ethylene terephthalate) substrate", *Carbon*, 2013, 55(0), pp. 144-150.
[114] H. Wagner, D. Bedorf, S. Küchemann, M. Schwabe, B. Zhang, W. Arnold, and K. Samwer, "Local elastic properties of a metallic glass", *Nat. Mater.*, 2011, 10(6), pp. 439-442.
[115] Y. H. Liu, D. Wang, K. Nakajima, W. Zhang, A. Hirata, T. Nishi, A. Inoue, and M. W. Chen, "Characterization of nanoscale mechanical heterogeneity in a metallic glass by dynamic force microscopy", *Phys. Rev. Lett.*, 2011, 106(12), pp. 125504.
[116] Z. Y. Liu and Y. Yang, "A mean-field model for anelastic deformation in metallic-glasses", *Intermetallics*, 2012, 26(0), pp. 86-90.
[117] J. Antonaglia, X. Xie, M. Wraith, J. Qiao, Y. Zhang, P. K. Liaw, J. T. Uhl, and K. A. Dahmen, "Tuned critical avalanche scaling in bulk metallic glasses", *Sci. Rep.*, 2014, 4, p. 4382.
[118] Y. Yokoyama, H. Fredriksson, H. Yasuda, M. Nishijima, and A. Inoue, "Glassy solidification criterion of Zr50Cu40Al10 alloy", *Mater. Trans.*, 2007, 48(6), pp. 1363-1372.
[119] Y. Yokoyama, H. Inoue, K. Fukaura, and A. Inoue, "Relationship between the liquidus surface and structures of Zr-Cu-Al bulk amorphous alloys", *Mater. Trans.*, 2002, 43(3), pp. 575-579.

[120] C. E. Packard, E. R. Homer, N. Al-Aqeeli, and C. A. Schuh, "Cyclic hardening of metallic glasses under Hertzian contacts: Experiments and STZ dynamics simulations", *Philos. Mag.*, 2010, 90(10), pp. 1373-1390.

[121] M. E. Launey, R. Busch, and J. J. Kruzic, "Effects of free volume changes and residual stresses on the fatigue and fracture behavior of a Zr–Ti–Ni–Cu–Be bulk metallic glass", *Acta Mater.*, 2008, 56(3), pp. 500-510.

[122] Z. Han and Y. Li, "Cooperative shear and catastrophic fracture of bulk metallic glasses from a shear-band instability perspective", *J. Mater. Res.*, 2009, 24(12), pp. 3620-3627.

[123] B. A. Sun, S. Pauly, J. Tan, M. Stoica, W. H. Wang, U. Kühn, and J. Eckert, "Serrated flow and stick–slip deformation dynamics in the presence of shear-band interactions for a Zr-based metallic glass", *Acta Mater.*, 2012, 60(10), pp. 4160-4171.

[124] S. X. Song and T. G. Nieh, "Flow serration and shear-band viscosity during inhomogeneous deformation of a Zr-based bulk metallic glass", *Intermetallics*, 2009, 17(9), pp. 762-767.

[125] G. Wang, K. C. Chan, L. Xia, P. Yu, J. Shen, and W. H. Wang, "Self-organized intermittent plastic flow in bulk metallic glasses", *Acta Mater.*, 2009, 57(20), pp. 6146-6155.

[126] F. H. Dalla Torre, A. Dubach, J. Schällibaum, and J. F. Löffler, "Shear striations and deformation kinetics in highly deformed Zr-based bulk metallic glasses", *Acta Mater.*, 2008, 56(17), pp. 4635-4646.

[127] S. X. Song, H. Bei, J. Wadsworth, and T. G. Nieh, "Flow serration in a Zr-based bulk metallic glass in compression at low strain rates", *Intermetallics*, 2008, 16(6), pp. 813-818.

[128] F. H. Dalla Torre, D. Klaumünzer, R. Maaß, and J. F. Löffler, "Stick–slip behavior of serrated flow during inhomogeneous deformation of bulk metallic glasses", *Acta Mater.*, 2010, 58(10), pp. 3742-3750.

[129] L. Y. Chen, Z. D. Fu, G. Q. Zhang, X. P. Hao, Q. K. Jiang, X. D. Wang, Q. P. Cao, H. Franz, Y. G. Liu, H. S. Xie, S. L. Zhang, B. Y. Wang, Y. W. Zeng, and J. Z. Jiang, "New class of plastic bulk metallic glass", *Phys. Rev. Lett.*, 2008, 100(7), pp. 4, p. 075501.

[130] J. Das, M. B. Tang, K. B. Kim, R. Theissmann, F. Baier, W. H. Wang, and J. Eckert, ""Work-hardenable" ductile bulk metallic glass", *Phys. Rev. Lett.*, 2005, 94(20), p. 205501.

[131] Y. Zhang, W. H. Wang, and A. L. Greer, "Making metallic glasses plastic by control of residual stress", *Nat. Mater.*, 2006, 5(11), pp. 857-860.

[132] S. B. Kim, J. Shackleton, M. Preuss, P. J. Withers, A. Evans, and G. Bruno, "Stress relaxation of shot-peened UDIMET 720Li under solely elevated-temperature exposure and under isothermal fatigue", *Metall. Mater. Trans. A*, 2005, 36(11), pp. 3041-3053.

[133] R. Nalla, I. Altenberger, U. Noster, G. Liu, B. Scholtes, and R. Ritchie, "On the influence of mechanical surface treatments—deep rolling and laser shock peening—on the fatigue behavior of Ti–6Al–4V at ambient and elevated temperatures", *Mater. Sci. Eng., A*, 2003, 355(1), pp. 216-230.

[134] A. King, A. Steuwer, C. Woodward, and P. J. Withers, "Effects of fatigue and fretting on residual stresses introduced by laser shock peening", *Mater. Sci. Eng., A*, 2006, 435-436(0), pp. 12-18.

[135] N. H. Tariq, B. A. Hasan, and J. I. Akhter, "Evolution of microstructure in Zr55Cu30Al10Ni5 bulk amorphous alloy by high power pulsed Nd:YAG laser", *J. Alloys Compd.*, 2009, 485(1–2), pp. 212-214.

[136] G. Wu, R. Li, Z. Liu, B. Chen, Y. Li, Y. Cai, and T. Zhang, "Induced multiple heterogeneities and related plastic improvement by laser surface treatment in CuZr-based bulk metallic glass", *Intermetallics*, 2012, 24(0), pp. 50-55.

[137] B. Chen, S. Pang, P. Han, Y. Li, A. R. Yavari, G. Vaughan, and T. Zhang, "Improvement in mechanical properties of a Zr-based bulk metallic glass by laser surface treatment", *J. Alloys Compd.*, 2010, 504, Supplement 1(0), pp. S45-S47.

[138] X. H. Lin, W. L. Johnson, and W. K. Rhim, "Effect of oxygen impurities on crystallization on undercooled bulk glass forming Zr-Ti-Cu-Ni-Al alloy", *Materials Transactions Jim*, 1997, 38(5), pp. 473-477.

[139] T. G. Nieh, J. Wadsworth, C. T. Liu, T. Ohkubo, and Y. Hirotsu, "Plasticity and structural instability in a bulk metallic glass deformed in the supercooled liquid region", *Acta Mater.*, 2001, 49(15), pp. 2887-2896.

[140] W. H. Peter, R. A. Buchanan, C. T. Liu, and P. K. Liaw, "The fatigue behavior of a Zirconium-based bulk metallic glass in vacuum and air", *J. Non Cryst. Solids*, 2003, 317(1-2), pp. 187-192.

[141] M. L. Morrison, R. A. Buchanan, P. K. Liaw, B. A. Green, G. Y. Wang, C. Liu, and J. A. Horton, "Four-point-bending-fatigue behavior of the Zr-based Vitreloy 105 bulk metallic glass", *Mater. Sci. Eng., A*, 2007, 467(1-2), pp. 190-197.

[142] C. G. Tang, Y. Li, and K. Y. Zeng, "Characterization of mechanical properties of a Zr-based metallic glass by indentation techniques", *Mater. Sci. Eng., A*, 2004, 384(1-2), pp. 215-223.

[143] B. Winiarski, R. M. Langford, J. W. Tian, Y. Yokoyama, P. K. Liaw, and P. J. Withers, "Mapping residual stress distributions at the micron scale in amorphous materials", *Metall. Mater. Trans. A*, 2010, 41A(7), pp. 1743-1751.

[144] B. Winiarski, G. S. Schajer, and P. J. Withers, "Surface decoration for improving the accuracy of displacement measurements by digital image correlation in SEM", *Experimental Mechanics*, 2012, 52(7), pp. 793-804.

[145] X. Qiu, J. W. Thompson, and S. J. L. Billinge, "PDFgetX2: a GUI-driven program to obtain the pair distribution function from X-ray powder diffraction data", *J. Appl. Crystallogr.*, 2004, 37(4), p. 678.

[146] Y. Waseda, "The structure of non-crystalline materials: liquids and amorphous solids", 1980.

[147] M. E. Fitzpatrick and A. Lodini, "Analysis of residual stress by diffraction using neutron and synchrotron radiation", 2003: CRC Press.

[148] B. Wu and Y. C. Shin, "A one-dimensional hydrodynamic model for pressures near the coating-water interface during laser shock peening", *J. Appl. Phys.*, 2007, 101(2), pp. 023510-5.

[149] B. Wu and Y. C. Shin, "Two dimensional hydrodynamic simulation of high pressures induced by high-power nanosecond laser-matter interactions under water", *J. Appl. Phys.*, 2007, 101(10), pp. 103514.

[150] R. M. More, K. H. Warren, D. A. Young, and G. B. Zimmerman, "A new quotidian equation of state (QEOS) for hot dense matter", *Phys. Fluids*, 1988, 31(10), pp. 3059-3078.

[151] F. Ree, Equation of State of Water, 1976, California Univ., Livermore USA, Lawrence Livermore Lab.

[152] B. Wu and Y. C. Shin, "A self-closed thermal model for laser shock peening under the water confinement regime configuration and comparisons to experiments", *J. Appl. Phys.*, 2005, 97(11), pp. 113517, p. 113517.

[153] L. Berthe, R. Fabbro, P. Peyre, L. Tollier, and E. Bartnicki, "Shock waves from a water-confined laser-generated plasma", *J. Appl. Phys.*, 1997, 82(6), pp. 2826-2832.

[154] Y. Cao, Y. C. Shin, and B. Wu, "Parametric study on single shot and overlapping laser shock peening on various metals via modeling and experiments", *Journal of Manufacturing Science and Engineering-Transactions of the ASME*, 2010, 132(6), pp. 061010, p. 061010.

[155] B. Wu and Y. C. Shin, "From incident laser pulse to residual stress: a complete and self-closed model for laser shock peening", *Journal of Manufacturing Science and Engineering*, 2007, 129, pp. 117-125.

[156] ABAQUS, ABAQUS Analysis Manual, Version 6.9 Documentation, 2009, Simulia: Dassault Systèmes, RI, USA.

[157] C. Yang, R. P. Liu, Z. J. Zhan, L. L. Sun, and W. K. Wang, "High speed impact on $Zr_{41}Ti_{14}Cu_{12.5}Ni_{10}Be_{22.5}$ bulk metallic glass", *Mater. Sci. Eng., A*, 2006, 426(1-2), pp. 298-304.

[158] J. W. Tian, L. L. Shaw, Y. D. Wang, Y. Yokoyama, and P. K. Liaw, "A study on the surface severe plastic deformation behavior of a Zr-based bulk metallic glass (BMG)", *Intermetallics*, 2009, 17(11), pp. 951-957.

[159] J. W. Tian, J. C. Villegas, W. Yuan, D. Fielden, L. Shaw, P. K. Liaw, and D. L. Klarstrom, "A study of the effect of nanostructured surface layers on the fatigue behaviors of a C-2000 superalloy", *Mater. Sci. Eng., A*, 2007, 468–470(0), pp. 164-170.

[160] R. Sarmah, G. Ananthakrishna, B. A. Sun, and W. H. Wang, "Hidden order in serrated flow of metallic glasses", *Acta Mater.*, 2011, 59(11), pp. 4482-4493.

[161] C. Fan, L. Kecskes, T. Jiao, H. Choo, A. Inoue, and P. Liaw, "Shear-band deformation in amorphous alloys and composites", *Mater. Trans.*, 2006, 47(3), pp. 817-821.

[162] F. Shimizu, S. Ogata, and J. Li, "Theory of shear banding in metallic glasses and molecular dynamics calculations", *Mater. Trans.*, 2007, 48(11), pp. 2923-2927.

[163] J. Eckert, J. Das, K. B. Kim, F. Baier, M. B. Tang, W. H. Wang, and Z. F. Zhang, "High strength ductile Cu-base metallic glass", *Intermetallics*, 2006, 14(8-9), pp. 876-881.

[164] J. Zhang, P. Aimedieu, F. Hild, S. Roux, and T. Zhang, "Complexity of shear localization in a Zr-based bulk metallic glass", *Scripta Materialia*, 2009, 61(12), pp. 1145-1148.

[165] W. C. Oliver and G. M. Pharr, "An improved technique for determining hardness and elastic modulus using load and displacement sensing indentation experiments", *J. Mater. Res.*, 1992, 7(06), pp. 1564-1583.

[166] L. Wang, S. X. Song, and T. G. Nieh, "Assessing plastic shear resistance of bulk metallic glasses under nanoindentation", *Appl. Phys. Lett.*, 2008, 92(10), pp. 101925-3.

[167] T. Egami and S. J. L. Billinge, "Underneath the bragg peaks: structural analysis of complex materials", Vol. 7, 2003, pp. 219-244.

[168] G. R. Johnson and W. H. Cook, "A constitutive model and data for metals subjected to large strains, high strain rates and high temperatures", in *Proceedings of the 7th International Symposium on Ballistics*, 1983, 21: The Hague, Netherlands: International Ballistics Committee.

[169] Y. Fan, Y. Wang, S. Vukelic, and Y. L. Yao, "Wave-solid interactions in laser-shock-induced deformation processes", *J. Appl. Phys.*, 2005, 98(10), pp. 104904-11.

[170] H. Bruck, A. Rosakis, and W. Johnson, "The dynamic compressive behavior of beryllium bearing bulk metallic glasses", *J. Mater. Res.*, 1996, 11(2), pp. 503-511.

[171] Q. Yang, A. Mota, and M. Ortiz, "A finite-deformation constitutive model of bulk metallic glass plasticity", *Computational Mechanics*, 2006, 37(2), pp. 194-204.

[172] J. J. Lewandowski and A. L. Greer, "Temperature rise at shear bands in metallic glasses", *Nat. Mater.*, 2006, 5(1), pp. 15-18.

[173] B. Yang, M. L. Morrison, P. K. Liaw, R. A. Buchanan, G. Wang, C. T. Liu, and M. Denda, "Dynamic evolution of nanoscale shear bands in a bulk-metallic glass", *Appl. Phys. Lett.*, 2005, 86(14), p. 141904.

[174] H. M. Chen, J. C. Huang, S. X. Song, T. G. Nieh, and J. S. C. Jang, "Flow serration and shear-band propagation in bulk metallic glasses", *Appl. Phys. Lett.*, 2009, 94(14), p. 141914.

[175] Y. Yokoyama, T. Yamasaki, M. Nishijima, and A. Inoue, "Drastic increase in the toughness of structural relaxed hypereutectic $Zr_{59}Cu_{31}Al_{10}$ bulk glassy alloy", *Mater. Trans.*, 2007, 48(6), pp. 1276-1281.

[176] H. Leamy, T. Wang, and H. Chen, "Plastic flow and fracture of metallic glass", *Metallurgical and Materials Transactions B*, 1972, 3(3), pp. 699-708.

[177] W. J. Wright, R. B. Schwarz, and W. D. Nix, "Localized heating during serrated plastic flow in bulk metallic glasses", *Mater. Sci. Eng., A*, 2001, 319, pp. 229-232.

[178] W. H. Jiang, F. X. Liu, H. H. Liao, H. Choo, P. K. Liaw, B. J. Edwards, and B. Khomami, "Temperature increases caused by shear banding in as-cast and relaxed Zr-based bulk metallic glasses under compression", *J. Mater. Res.*, 2008, 23(11), pp. 2967-2974.

[179] W. J. Wright, M. W. Samale, T. C. Hufnagel, M. M. LeBlanc, and J. N. Florando, "Studies of shear band velocity using spatially and temporally resolved measurements of strain during quasistatic compression of a bulk metallic glass", *Acta Mater.*, 2009, 57(16), pp. 4639-4648.

[180] D. Klaumunzer, R. Maass, and J. F. Loffler, "Stick-slip dynamics and recent insights into shear banding in metallic glasses", *J. Mater. Res.*, 2011, 26(12), pp. 1453-1463.

[181] A. L. Greer, Y. Q. Cheng, and E. Ma, "Shear bands in metallic glasses", *Mater. Sci. Eng., R*, 2013, 74(4), pp. 71-132.

[182] S. V. Ketov and D. V. Louzguine-Luzgin, "Localized shear deformation and softening of bulk metallic glass: stress or temperature driven?", *Sci. Rep.*, 2013, 3, p. 2798.

[183] A. J. Cao, Y. Q. Cheng, and E. Ma, "Structural processes that initiate shear localization in metallic glass", *Acta Mater.*, 2009, 57(17), pp. 5146-5155.

[184] S. X. Song, X. L. Wang, and T. G. Nieh, "Capturing shear band propagation in a Zr-based metallic glass using a high-speed camera", *Scripta Materialia*, 2010, 62(11), pp. 847-850.

[185] S. X. Song and T. G. Nieh, "Direct measurements of shear band propagation in metallic glasses – An overview", *Intermetallics*, 2011, 19(12), pp. 1968-1977.

[186] W. J. Wright, R. R. Byer, and X. J. Gu, "High-speed imaging of a bulk metallic glass during uniaxial compression", *Appl. Phys. Lett.*, 2013, 102(24), pp. 4, p. 241920.

[187] B. Yang, C. T. Liu, T. G. Nieh, M. L. Morrison, P. K. Liaw, and R. A. Buchanan, "Localized heating and fracture criterion for bulk metallic glasses", *J. Mater. Res.*, 2006, 21(4), pp. 915-922.

[188] S. C. Glade, R. Busch, D. S. Lee, W. L. Johnson, R. K. Wunderlich, and H. J. Fecht, "Thermodynamics of Cu47Ti34Zr11Ni8,Zr52.5Cu17.9Ni14.6Al10Ti5 and Zr57Cu15.4Ni12.6Al10Nb5 bulk metallic glass forming alloys", *J. Appl. Phys.*, 2000, 87(10), pp. 7242-7248.

[189] W. H. Wang, "The elastic properties, elastic models and elastic perspectives of metallic glasses", *Prog. Mater. Sci.*, 2012, 57(3), pp. 487-656.

[190] Y. Zhang, N. A. Stelmashenko, Z. H. Barber, W. H. Wang, J. J. Lewandowski, and A. L. Greer, "Local temperature rises during mechanical testing of metallic glasses", *J. Mater. Res.*, 2007, 22(2), pp. 419-427.

[191] W. H. Jiang, H. H. Liao, F. X. Liu, H. Choo, and P. K. Liaw, "Rate-dependent temperature increases in shear bands of a bulk-metallic glass", *Metall. Mater. Trans. A*, 2008, 39A(8), pp. 1822-1830.

[192] D. T. A. Matthews, V. Ocelĺk, P. M. Bronsveld, and J. T. M. De Hosson, "An electron microscopy appraisal of tensile fracture in metallic glasses", *Acta Mater.*, 2008, 56(8), pp. 1762-1773.

[193] J. W. Qiao, H. L. Jia, Y. Zhang, P. K. Liaw, and L. F. Li, "Multi-step shear banding for bulk metallic glasses at ambient and cryogenic temperatures", *Mater. Chem. Phys.*, 2012, 136(1), pp. 75-79.

[194] D. B. Miracle, A. Concustell, Y. Zhang, A. R. Yavari, and A. L. Greer, "Shear bands in metallic glasses: Size effects on thermal profiles", *Acta Mater.*, 2011, 59(7), pp. 2831-2840.

[195] J. W. Qiao, Z. Wang, Z. M. Jiao, H. J. Yang, S. G. Ma, Z. H. Wang, and B. S. Xu, "Predicting burst sizes in amorphous alloys during plastic flows", *Mater. Sci. Eng., A*, 2014, 609(0), pp. 222-225.

VITA

Xie Xie was born in Xinyang, China. He got the Bachelor of Science degree in Materials Science and Engineering at Shanghai Jiao Tong University, China. He started his graduate study at the University of Tennessee, Knoxville from August 2009. In December 2014, he graduated from the University of Tennessee with Doctor of Philosophy degree in Materials Science and Engineering.